Magnetic read only memory

op 't Root, W.P.E.M.

Award date:
2005

Eindhoven University of Technology
Department of Applied Physics
Physics of Nanostructures (FNA)

Philips Research Eindhoven
Storage Physics

Magnetic Read Only Memory
W.P.E.M. Op 't Root
Feb 2005

Magnetic Read Only Memory

W.P.E.M. Op 't Root

Feb 2005

Supervisors:
Dr. Ir. F.J. Jedema
Dr. Ir. H. J. M. Swagten

Abstract

In this master project a feasibility study of the magnetic read only memory (MROM) concept has been carried out, at Philips Research Eindhoven. The MROM concept combines the advantages of optical and solid-state storage, by separating the solid-state reader from the information carrier. The information is encoded into the topography of the carrier, which is made ferromagnetic. The reader consists of a two dimensional array of magnetoresistive sensor elements. In order to determine the feasibility, a reader and information carrier have been fabricated, both having a surface of ~ 1 cm^2, plus the necessary mechanics and optics, needed to bring them into close contact in a controlled manner. A theoretical description of the reader and information carrier is developed for the interpretation of the results. The magnetoresistive sensor elements, which are magnetic tunnel junctions, are calibrated with a known external magnetic field. It is found that they are suitable for bit detection. The minimal obtainable separation distance between the reader and information carrier is 0.63 μm, under careful prepared experimental conditions. The experiment is conducted with bits and magnetic tunnel junctions having a dimension of 5 x 1 μm (length x width). The bits are scanned over a sensor element, while measuring its electrical resistance. This is done for various separation distances between the information carrier and the reader. The measured signal is compared with the theory, and it is found that the results can be quantitatively described with the theory. The required separation distance between the reader and information carrier for video application is calculated, and it is shown that it is smaller than 0.63 μm. This brings us to the conclusion, that the MROM concept is not suitable for any application requiring bit densities and bit rates, associated with video applications.

1 Introduction and technology assessment

Data storage can be categorized in three different segments being, optical storage, magnetic disc storage and non-volatile solid-state storage. Optical storage has the advantage that the read out mechanism and the information carrier are separated from another. Well-known examples of optical storage are the compact disc (CD) and the digital versatile disc (DVD). The read out is performed by scanning a laser beam, which is focused through a lens, over the information carrier. The data is encoded into the reflectance of the material on the medium at a certain position. Because the lens must be focused at all times at the information carrier, the reader typically consists of fine mechanics controlled by feedback loops. This makes the reader expensive to fabricate and difficult to miniaturize. The strength of optical storage is that the information carrier can be mass manufactured at low cost. In addition, the medium is very reliable. This makes optical storage the preferred solution for distributing pre-recorded digital content, such as audio and video, or computer software.

Magnetic disc storage has other advantages, such as a higher areal density, shorter random access time, higher data throughput and almost unlimited number of overwrite cycles. Due to these advantages magnetic storage is the preferred solution for data storage in computers. A well-known example of magnetic disc storage is the hard disc drive (HDD), in which the read out is performed by scanning a magnetic sensor over a magnetic information carrier. Because the magnetic sensor in a HDD has to be very close to the rotating information carrier (disc), typically in the order of tens of nanometers, the read out is sensitive to dust. Therefore the medium and read out mechanism cannot be separated from another. This makes the HDD unsuitable as a low cost option for the distribution of pre-recorded content.

Non-volatile solid-state storage is currently dominated by flash memory. Flash memory is a form of electrical erasable programmable read only memory (EEPROM), in which bits are addressed in blocks. Flash has a limited data rate and a limited number of overwrite cycles. On the other hand, it does have full random access and low power consumption. However, the main advantage of flash is that it has no moving parts, which makes it very robust and enables storage solutions that can be miniaturized. Flash memory can be embedded in an integrated circuit (IC), but is also often used for mass data storage, for example in a USB memory stick.

A new example of non-volatile solid-storage is magnetic random access memory (MRAM), which is closely related to the storage device that will be investigated in this thesis. It has the same advantages as flash, with the option for a higher data rate and larger number of overwrite cycles. In Fig. 1.1 a schematic representation of a MRAM is given. It consists of horizontal and vertical current lines with a memory element at every cross-section. In the most general definition the data is stored into the magnetization directions of the memory elements, which are read out electrically. This implies that the memory elements have to show magnetoresistance. In early MRAM's the anisotropic magnetoresistance (AMR) effect was used to define a bit. The AMR effect causes the electrical resistance to increase when an external magnetic field is applied perpendicular to the current. It only arises in ferromagnetic materials and is a result of the change in the orientations of electron orbitals. Because the magnitude of the AMR effect in thin films is typically less than 3% of the thin film resistance, it was only used in military and space applications, because it is

insensitive to electromagnetic radiation. The discovery of the giant magnetoresistance (GMR) effect improved this. The GMR effect is a result of the transport behavior of two ferromagnetic metal layers that are separated by a non-magnetic metal spacer. The two ferromagnetic metal layers need to be magnetically separated because the magnetoresistance depends on the relative orientation of the magnetization of the two ferromagnetic layers. The GMR allowed the realization of memory elements with higher resistance and larger MR effect (~ 5 à 15 %) and therefore a higher output signal. This made the MRAM, in principle, suitable for general applications. In 1995 a breakthrough in field of magnetic tunnel junctions (MTJ), showing an unprecedented magnetoresistance at room temperature, improved the commercial perspective for MRAM even further. The tunnel magnetoresistance (TMR) arises because the tunnel current between two ferromagnetic electrodes, separated by a thin barrier, depends on the relative orientation of the magnetization of the two electrodes. At this point in time there are no applications with MRAM, but it is expected that they come to the market within one or two years.

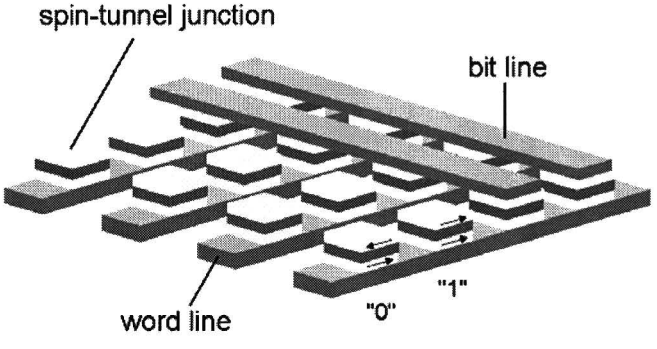

Fig. 1.1: Schematic representation of an MRAM array. It composes of a crossbar array of current lines with magnetoresistive elements at each intersection. An anti-parallel magnetization configuration of the layers of an element results in a high resistance, a parallel configuration results in a low resistance. This is used to store a one or zero.

The general idea behind the research in this thesis is to investigate the feasibility of a new storage concept, which combines the advantages of optical storage with those of non-volatile solid-state storage. This would mean that the storage concept facilitates a rapid random access, high data rate and low power consumption, plus an inexpensive replicable and removable information carrier. Moreover would it be robust and insensitive to shock, due to the absence of moving parts. This would make it the preferred solution for low cost distribution of pre-recorded digital content, in particular for mobile applications. This storage solution requires a solid-state reader, consisting of an array of sensors, at which a removable information carrier can be attached. The physical representation of a bit can be in principle anything.

1.1 Magnetic read only memory

In this research the general idea of separating the read out and storage functionality is investigated when magnetic bits represent the information. An advantage of magnetic signals is that they do not suffer from charging effects on the medium or sensor, as would be the case when the information is represented by electrical charges. This idea will be called magnetic read only memory (MROM). The concept is to store information into a manufactured 2 dimensional plane of magnetic bit locations. The read out is performed by an array of magnetoresistive sensor elements. In Fig. 1.2 a schematic representation of the MROM idea is shown. In the left we see the magnetic bit locations and the array of magnetoresistive sensor elements separate from each other. The information is encoded into the topography of the medium, and in order to perform the read out the blocks are made ferromagnetic. If we place the sensor array on top of the medium, see the right picture, we can read out the information on the medium, by measuring the electrical resistance of the elements in the sensor array.

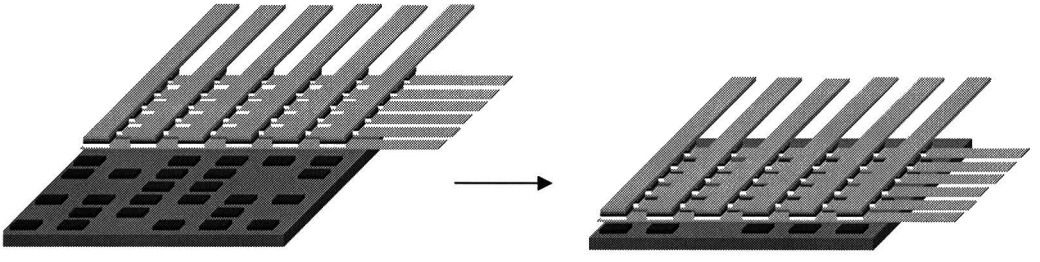

Fig. 1.2: Schematic representation of the MROM concept. In the left we see the information carrier and read out mechanism separated. The information is encoded into the topography of the carrier, which is made ferromagnetic. The reader consists of a 2 dimensional array of magneto restive elements. If we place the reader on top of the information carrier, we can read out the information on the carrier, by measuring the resistance of the elements in the sensor array. This is schematically drawn in the right picture.

In this particular embodiment the pre-recorded media could be manufactured very cheap. In principle it can be replicated in the same way as an optical disc with one additional step, the deposition of a ferromagnetic layer.

1.2 Sensor

The sensors used in this research are MTJ's. The choice for MTJ's is because they show a large magnetoresistance at room temperature. However, a disadvantage of MTJ's is the tunnel barrier. It can be easily destroyed with a peak in the bias voltage due to electrostatic discharge (ESD). In order to prevent this from happening proper grounding procedures have to be taken when measuring the MTJ's.

1.3 Medium

The medium is a glass substrate, to facilitate optical experiments, with a structured resist layer. The structured resist layer consists of blocks of resist, which are defined with electron beam (e-beam) lithography, on which a ferromagnetic layer is deposited. Fig. 1.3 shows a scanning electron microscope (SEM) picture of a group of five bits, with the ferromagnetic layer (CoFe) deposited.

The CoFe on top of a resist block will create a magnetic stray field, which we can detect with the MTJ's. This allows us to read out the information encoded into the topography of the medium.

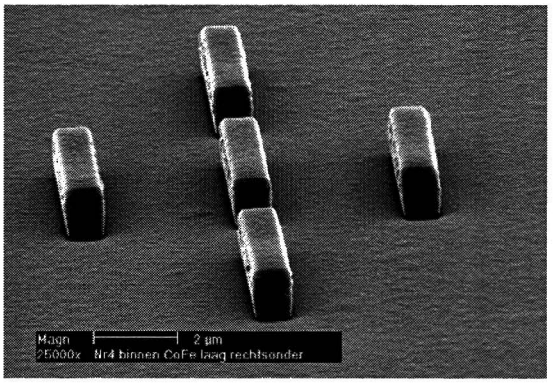

Fig. 1.3: SEM Picture of the bits with the ferromagnetic layer deposited on top of them.

1.4 Motivation and goal of research

As mentioned above, the separation of a solid-state reader and storage functionality promises a lot of advantages. Specifically, it combines the advantages of optical storage with those of solid-state storage. In principle this could be achieved in a lot of different ways. In this particular case magnetic bits were chosen to represent the information, and we use an electrical read out of the sensor.

To general goal of the work, described in this thesis, is to test the feasibility of the MROM concept. The two most important aspects, that will determine the success of MROM, are the bit density and data rate obtainable in a real application. The size of the fabricated MTJ elements and bits in this report are in the order of micrometers. The results of the experiment, however, have to be scaled to the much smaller dimensions to see what the performance of the MROM concept would be in a real application.

In order to fulfill this goal the following items have to be addressed.

- We have to fabricate a sensor and medium
- An experimental setup, to determine and control the alignment of, and distance between, the medium and sensor is necessary.
- We have to calibrate the MTJ elements of the sensor.
- The magnetic stray field of the bit pattern needs to be calculated theoretically.
- An assessment of the sensitivity of the MTJ elements is necessary.

In chapter 2 the necessary theory is explained for describing the magnetic and electrical properties of the bit pattern and the sensor. This will provide a basis for the interpretation of the experimental results. Chapter 2 also deals with optical interferometry, which is necessary for the experimental setup. More precisely, monochromatic interferometry is used to align the medium and sensor parallel, and white light interferometry is used to determine the separation distance between the medium and sensor. In chapter 3 the experimental setup is described in three parts. The first part reports on the processing of the sensor and medium. The second part deals with the mechanical

setup used to manipulate the sensor and medium on a nanometer scale. This includes the monochromatic and white light interferometers. The third part describes a setup used to calibrate the magnetoresistance of the MTJ's. In chapter 4 the results of the experiments are shown. The most important experiment is the bit detection, however first some experiments necessary for the interpretation of the bit detection are shown and discussed. It starts with the calibration of the tunnel junctions. Then measurements of the performance of the monochromatic and white light interferometer are shown and discussed. The third paragraph of chapter 4 is about the bit detection; it shows the measured magnetic bit fields comparison with theory, as described in chapter 2, and the measurements done with the MTJ array. In the last paragraph of chapter 4 the feasibility of the MROM concept is discussed. This will be done by calculation the design constraints aiming at portable video applications. In chapter 5, the final chapter, the conclusions and recommendations will be presented.

2 Theory

The theory chapter describes two different subjects. One being the magnetic theory used to describe the experiment, and the other subject is an optical theory used to describe important parts of the experimental setup.

The magnetic theory starts with the derivation of magnetostatics from the Maxwell equations. We will assume in the entire thesis that the magnetization is homogenous throughout the sample and that can only change its direction, not its magnitude. This knowledge is applied to a ferromagnet with the shape of a rectangle, because this shape is applicable to a bit as well as to a sensor. More specifically, the thermodynamic rest state and magnetization rotation in an external magnetic field, of a rectangular ferromagnet, are discussed. For this last subject a modified Stoner-Wohlfarth model is used. The modification with respect to the Stoner-Wohlfarth model is an extra term, necessary to describe so called exchange bias. When all relevant magnetic properties of a rectangular ferromagnet are discussed, it will be applied to the bit and sensor. First the magnetic stray field of one or more bits will be calculated. Secondly, the realization of a sensor, out of several magnetic and non-magnetic layers, will be explained and the sensitivity of such a sensor is discussed. The magnetic part of the theory is ended with a discussion of the theoretical performance of the MROM concept and the critical factors determining the performance.

One of the critical factors determining the performance of the MROM concept is the separation distance between the medium and the sensor. Another experimental requirement is that the medium and sensor plane have to be aligned parallel with respect to each other. Both these issues are addressed in the experimental setup with interferometry and the relevant optical theory is addressed in the last paragraph of the theory chapter.

2.1 Magnetostatics

The basic equations of the magnetostatics follow from the macroscopic Maxwell equations:

$$\vec{\nabla}\cdot\mathbf{D}=\rho_f \qquad \vec{\nabla}\cdot\mathbf{B}=0$$

$$\vec{\nabla}\mathrm{x}\mathbf{H}-\frac{\partial\mathbf{D}}{\partial t}=\mathbf{J}_f \qquad \vec{\nabla}\mathrm{x}\mathbf{E}+\frac{\partial\mathbf{B}}{\partial t}=0,$$

in which **D** is the electric displacement, **E** the electric field, **H** the magnetic field, **B** the magnetic induction, ρ_f the free charge density and $\mathbf{J}_f$ the free current density. Because our interest is only at magnetostatics we can reduce the above Maxwell equations by taking $\mathbf{D}=\mathbf{E}=0$, $\rho_f=0$ and setting all derivatives to the time to zero ($\partial/\partial t=0$). This gives us the following equations:

$$\vec{\nabla}\cdot\mathbf{B}=0 \tag{2.1}$$

$$\vec{\nabla}\mathrm{x}\mathbf{H}=\mathbf{J}_f. \tag{2.2}$$

We want to know the magnetic stray field of a ferromagnetic material, where the current density is zero ($\mathbf{J}_f = 0$). This implies that we can introduce a magnetic scalar potential ϕ_m such that

$$\mathbf{H} = -\vec{\nabla}\phi_m . \tag{2.3}$$

By doing this equation (2.2) is always fulfilled since the rotation of a gradient is always zero. If equation (2.1) is written in a different manner, which is[1]

$$\mu_0 \vec{\nabla} \cdot (\mathbf{H} + \mathbf{M}) = 0 \tag{2.4}$$

one can write down a magnetostatic Poisson equation

$$\vec{\nabla}^2 \phi_m = -\rho_m \tag{2.5}$$

where ρ_m is the effective magnetic-charge density:

$$\rho_m = -\vec{\nabla} \cdot \mathbf{M} . \tag{2.6}$$

According to equation (2.6) we can interpret the divergence of magnetization as an effective magnetic charge. This effective magnetic charge creates a magnetic field just as an electric charge creates an electric field.

2.1.1 Poisson equation

Before substituting the magnetization into equation (2.6) and applying it to the case of rectangular ferromagnet, a general method of solving the Poisson equation will be discussed. Let us assume we want to solve the following equation:

$$\vec{\nabla}^2 \phi(\mathbf{x}) = -\rho(\mathbf{x}) \tag{2.7}$$

where $\rho(\mathbf{x})$ is a arbitrary function of the coordinates. We can image $\rho(\mathbf{x})$ to be a charge distribution that is build up from point charges. In a more mathematical way this can be put as

$$\rho(\mathbf{x}) = \int_V \rho(\mathbf{y}) \delta(\mathbf{x} - \mathbf{y}) d^3\mathbf{y} , \tag{2.8}$$

where V is the volume of the area were we want to know the solution of the Poisson equation and $\delta(\mathbf{x}\text{-}\mathbf{y})$ is the Dirac-delta function. First we are going to solve the Poisson equation for a point

[1] If this step and the Maxwell equations are unknown for the reader he or she is referred to reference [2].

charge somewhere in space and then use that result to obtain the result for the entire charge distribution. The Poisson equation for a point "charge" at a position **y** is[2]

$$\vec{\nabla}^2 \phi_y(\mathbf{x}) = -\delta(\mathbf{x}-\mathbf{y}). \tag{2.9}$$

If we assume that our area of interest is the entire 3 dimensional space (which is true in our case) and we use the following conditions (also very reasonable),

$$\phi(\mathbf{x}) \to 0, |\mathbf{x}| \to \infty,$$

then the solution of equation (2.9) is the Coulomb potential (see reference [3])

$$\phi_y(\mathbf{x}) = -\frac{1}{4\pi|\mathbf{x}-\mathbf{y}|}. \tag{2.10}$$

The solution of the Poisson equation (2.7) can be obtained by summing the contributions of the point charges at the different points **y** with a weight factor $\rho(\mathbf{y})$:[3]

$$\phi(\mathbf{x}) = \int_V \rho(\mathbf{y})\phi_y(\mathbf{x}) d^3\mathbf{y} = -\frac{1}{4\pi}\int_V \frac{\rho(\mathbf{y})}{|\mathbf{x}-\mathbf{y}|} d^3\mathbf{y}. \tag{2.11}$$

Equation (2.11) gives us a general way to solve the Poisson equation for any charge distribution $\rho(\mathbf{x})$.

2.1.2 Magnetostatic potential and magnetic field of rectangular ferromagnet

We will now apply the general approach, for solving the Poisson equation, to calculate the magnetic field produced by the effective magnetic charge distribution of a single domain rectangular ferromagnet. The rectangular ferromagnet is drawn schematically in Fig. 2.1.

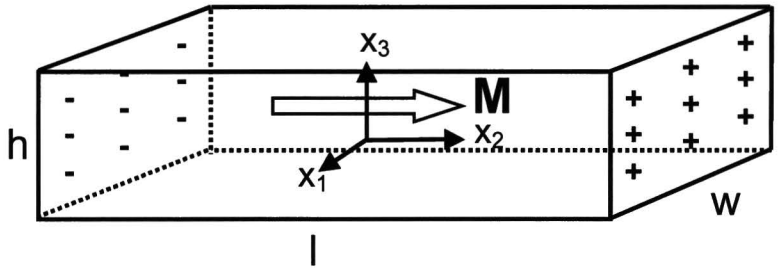

Fig. 2.1: Schematic picture of a rectangular ferromagnet. The magnetization is assumed to be homogenous and in one direction in the entire rectangular. The effective magnetic surface charges follow from equation (2.6).

[2] Note that point charge is a bit misleading because the dimension of the Dirac-delta function is m^{-3}. This can be understood if one realizes that equation (2.8) is in fact the defining characteristic of the Dirac-delta function.
[3] The reason that we can sum the contributions of the point charge to form the entire solution is because the Laplace operator is a linear operator.

This requires us to determine the effective magnetic charge distribution. If we assume that the magnetization is homogenous and in one direction in the entire bit, it is zero inside the bit, see equation (2.6). However, going from inside to outside the magnetization drops from its homogenous value in the bit, to zero at the surface. By integrating equation (2.6) over a small box straddling the surface (Fig. 2.2) and applying the divergence theorem we can show that there is an effective magnetic surface charge density equal to

$$\sigma_m = \mathbf{n}[\mathbf{x}] \cdot \mathbf{M}, \tag{2.12}$$

in which $\mathbf{n}[\mathbf{x}]$ is the outward normal on the surface of the rectangular ferromagnet at position $\mathbf{x}$.

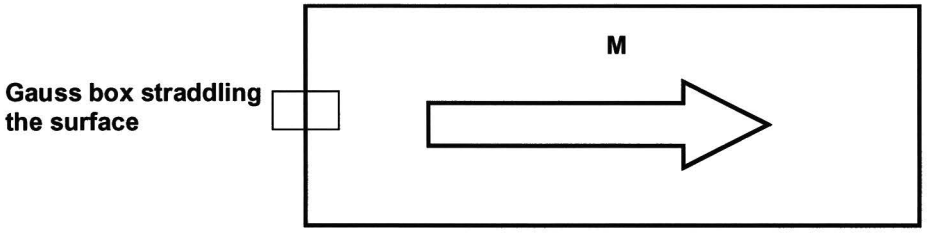

Fig. 2.2: Cross-section of the magnetic bit with a gauss box straddling the surface.

Substituting equation (2.12) into (2.11) gives the magnetic scalar potential

$$\phi_{\mathrm{m}}(\mathbf{x}) = \frac{1}{4\pi} \oint_{\text{Surface Bit}} \frac{\mathbf{n}[\mathbf{y}] \cdot \mathbf{M}}{|\mathbf{x}-\mathbf{y}|} d^2\mathbf{y}. \tag{2.13}$$

The divergence of equation (2.13) gives the magnetic field, see equation (2.3),

$$\mathbf{H}[\mathbf{x}] = -\frac{1}{4\pi} \oint_{\text{Surface Bit}} (\mathbf{n}[\mathbf{y}] \cdot \mathbf{M}) \frac{\mathbf{x}-\mathbf{y}}{|\mathbf{x}-\mathbf{y}|^3} d^2\mathbf{y} = -\vec{\vec{\mathbf{N}}}[\mathbf{x}] \cdot \mathbf{M}, \tag{2.14}$$

with $\vec{\vec{\mathbf{N}}}[\mathbf{x}]$ being a tensor function with components,

$$N_{\mathrm{ij}}[\mathbf{x}] = \frac{1}{4\pi} \oint_{\text{Surface Bit}} \frac{n_j[\mathbf{y}](x_i - y_i)}{|\mathbf{x}-\mathbf{y}|^3} d^2\mathbf{y}, \tag{2.15}$$

where i,j = 1,2,3. The expressions for the components, in the case of a rectangular ferromagnet, are listed in appendix 7.2.

In conclusion of paragraph 2.1, we have deduced magnetostatics from the Maxwell equations and shown that the Poisson equation plays an important role in it. Therefore we addressed a general method for solving it. After the effective magnetic charge distribution of a rectangular ferromagnet was determined, it was used to find an expression for the magnetic stray field of a rectangular ferromagnet.

2.2 Magnetic properties rectangular ferromagnet

With the magnetic stray field of rectangular ferromagnet known, we can use it to further explore its magnetic properties. In the coming two paragraphs we will discuss the direction the magnetization assumes, with and without an external magnetic field.

2.2.1 Magnetic anisotropy

In order to understand the thermodynamic equilibrium state of the magnetization of the bits, the magnetic anisotropy of the rectangular ferromagnet will be discussed. In order to do this we are going to calculate the self-energy density of the rectangular ferromagnet drawn in Fig. 2.1, as function of the direction of the magnetization and determine what direction has the lowest self-energy density. With self-energy density we mean the energy density of the rectangular ferromagnet, in the magnetic field produced by the rectangular ferromagnet itself. This magnetic field in the rectangular ferromagnet is the so called demagnetization field[4] ($\mathbf{H}_d[\mathbf{r}]$). The self-energy ($u[\mathbf{r}]$) can then be written as

$$u[\mathbf{r}] = -\frac{\mu_0}{2}\mathbf{M}\cdot\mathbf{H}_d[\mathbf{r}]. \tag{2.16}$$

To avoid tedious mathematics we are going to calculate the self-energy density, and thus $\mathbf{H}_d[\mathbf{r}]$, at $\mathbf{r} = \mathbf{0}$ since this allows us to use the symmetry of the rectangular bit. More precisely this means that at $\mathbf{r} = \mathbf{0}$ the off-diagonal components,

$$N_{ij}[\mathbf{0}] = 0,\ i \neq j, \tag{2.17}$$

are zero. The components on the diagonal of the tensor function are,

$$N_i[\mathbf{0}] = \frac{2}{\pi}\arctan\left[\frac{b_j b_k}{b_i\sqrt{(b_i^2 + b_j^2 + b_k^2)}}\right], \tag{2.18}$$

with b_i the dimensions of the bit in the x_i direction and i ≠ j ≠ k. Since in our case, see Fig. 2.1, $b_2 > b_1 >> b_3$ and because the arctan is a monotonic function it follows that $N_2 < N_1 << N_3$. Equation (2.14) and (2.18) together give $\mathbf{H}_d[\mathbf{0}]$. If we use this to calculate the self-energy density at $\mathbf{r} = \mathbf{0}$ this gives

$$u[\mathbf{0}] = -\frac{\mu_0}{2}\mathbf{M}\cdot\mathbf{H} = \frac{\mu_0}{2}\mathbf{M}\cdot\tilde{\mathbf{N}}[\mathbf{0}]\cdot\mathbf{M}. \tag{2.19}$$

Since we assumed that the magnetization is homogenous, it is a natural choice to describe it in spherical coordinates

[4] The name comes from the fact that in most cases the demagnetization field is in opposite direction of the magnetization.

$$\mathbf{M} = M \begin{pmatrix} \sin[\theta]\sin[\phi] \\ \cos[\theta]\sin[\phi] \\ \cos[\phi] \end{pmatrix}. \tag{2.20}$$

The definitions of the two angles, θ and ϕ, are depicted in Fig. 2.3.

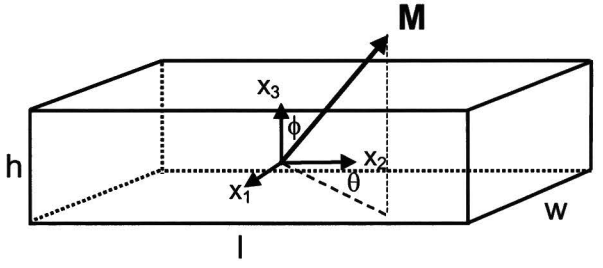

Fig. 2.3: Schematic picture of rectangular bit with the definition of the spherical coordinates.

If we fill in (2.20) into (2.19) we obtain

$$u[\mathbf{0}] = \frac{\mu_0}{2} M^2 (N_1 \sin^2[\theta]\sin^2[\phi] + N_2 \cos^2[\theta]\sin^2[\phi] + N_3 \cos^2[\phi]). \tag{2.21}$$

Calculating the thermodynamic equilibrium state of the magnetization requires minimizing equation (2.21) with respect to ϕ and θ. Since $N_2 < N_1 << N_3$ this means that the last term in (2.21) has to be zero and thus $\phi = \pi/2 + n\pi$, n being an integer. To see what direction, in the plane of the bit, is most favorable we insert $\phi = \pi/2 + n\pi$ into (2.21) and rewrite it

$$u[\mathbf{0}] = \frac{\mu_0}{2} M^2 (N_2 + (N_1 - N_2)\sin^2[\theta]). \tag{2.22}$$

Since $N_2 < N_1$ the lowest obtainable energy density is when $\theta = 0 + m\pi$, m being an integer. This brings us to the conclusion that if the magnetization is in its thermodynamic rest position it will be directed in the plane of the bit and point in the longitudinal direction of the rectangular ferromagnet. This corresponds with the direction drawn in Fig. 2.1.

2.2.2 Magnetization rotation in external magnetic field

If we want determine the influence of an external magnetic field, we have to take the magnetostatic energy into account, apart from the anisotropic shape energy. This is done in the Stoner-Wohlfarth model. An important assumption within this model is that M is constant at M_{sat} and uniform throughout the sample. This is justified because we are using a hard ferromagnetic material, which has a permanent magnetization of almost M_{sat}. We have added an extra term to the model in order to describe exchange coupling, this will be necessary for a description of the sensor.

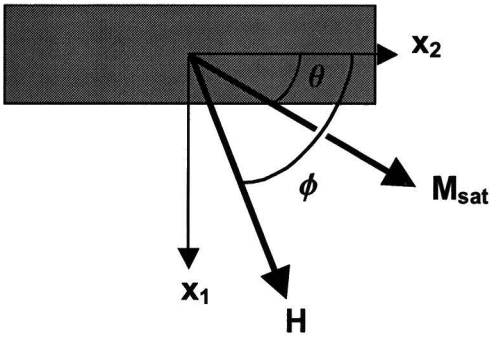

Fig. 2.4: Schematic top view of the rectangular ferromagnet. For the sensor we are mainly interested in thin films and therefore we assume that the magnetization will only rotate only in the x_1-x_2 plane. The amplitude of the magnetization is M_{sat}, it is assumed to stay constant at the saturation magnetization. The amplitude of the external magnetic field is H.

For the sensor we are mainly interested in thin films and therefore we assume that the magnetization will only rotate only in the x_1-x_2 plane. In that case the total energy density ($u[\theta]$) can be written as

$$u[\theta,\phi] = K\sin^2[\theta] - \mu_0 M_{sat} H\cos[\phi-\theta] - A\cos[\theta], \tag{2.23}$$

in which the first terms expressed the anisotropy energy with $K = (\mu_0/2)M_{sat}^2(N_1\text{-}N_2)$ describing its strength.[5] The second term is the magnetostatic energy with M_{sat} as the saturation magnetization, H the amplitude of the external magnetic field and μ_0 the magnetic permeability. The angles θ and ϕ are depicted in Fig. 2.4. The last term in equation (2.23) is added to describe the exchange coupling with A describing its strength. The origin of this interaction is not explained here, it will be addressed when discussing the sensor. Important at this point is that the exchange coupling wants to keep the magnetization directed into the positive x_2 direction. The direction of the magnetization at certain external magnetic fields can be calculated by minimizing the energy density. Directly related to the experimental situation, will we define M as the projection of the magnetization along the external magnetic field direction

$$M = \frac{\mathbf{M}\cdot\mathbf{H}}{H} = M_{sat}\cos[\phi-\theta]. \tag{2.24}$$

The first situation we will investigate is when the external field is in the direction of x_2 ($\phi = 0$). In that case the energy density can be written as

$$u[\theta,\phi=0] = K\sin^2[\theta] - \mu_0 M_{sat} H'\cos[\theta], \tag{2.25}$$

in which $H' = H + H_{exchange}$ and $H_{exchange} = A / \mu_0 M_{sat}$. If there is no external magnetic field equation (2.25) has a minimum at $\theta = 0$ due to the exchange coupling.[6] We expect that the magnetization will rotate if we apply a negative external magnetic field, negative because of the direction, that is

[5] Note that the constant in equation (2.22) is dropped. Since we will be seeking an energy minimum this is no problem.
[6] This is if we assume that the exchange bias energy is larger then the anisotropy energy, or more mathematically if $H_{exchange} > K$.

larger than $H_{exchange}$. However, things are a little bit more complicated. Equation (2.25) does indeed have minimum for $\theta = \pi$ when $H' < 0$, but as long as $H' > -2K/\mu M_{sat}$ it also has a local minimum at $\theta = 0$, which will prevent the magnetization from rotating. To illustrate this a plot of the energy density at three values of H' is plotted in Fig. 2.5. Note that the curve for each H' is given an offset in energy, except for the curve of H'=0. This is done to separate the individual curves graphically. We see that for $H' = -K/\mu_0 M_{sat}$ the energy density does indeed have the lowest value at $\theta = \pi$, but there is a bump in the energy density that prevents the magnetization from rotating towards that value. The bump disappears when $H' \leq -2K/\mu M_{sat}$, and only then is the magnetization free to rotate from $\theta = 0$ to $\theta = \pi$. The reasoning is analog if the magnetization is already at $\theta = \pi$. In that case the external magnetic field has to surpass $H' \geq 2K/\mu M_{sat}$ before the magnetization rotates to $\theta = 0$. The resulting M vs. H' curve is drawn in Fig. 2.6. Notice that magnetization behaves different dependent on its history and that the exchange coupling shifts the M vs. H curve with $H_{exchange}$.

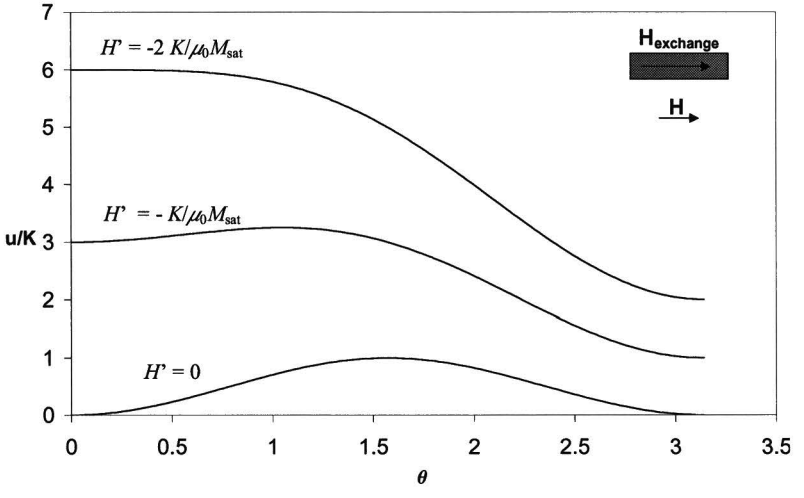

Fig. 2.5: Total energy density plotted versus θ at three different values of H' for $\phi = \pi$. Note that the curve for each H' is given an offset in energy, except the curve for H'=0. This is done to separate the individual curves. We see that the minimum of the energy density, when $H' = -K/\mu_0 M_{sat}$, is $\theta = \pi$. However, because of the "bump" in the energy density, the magnetization will not rotate at this value, instead it rotates when the "bump" disappears, at $H' = -2K/\mu_0 M_{sat}$. The corresponding M vs. H curve for this configuration is shown in Fig. 2.6.

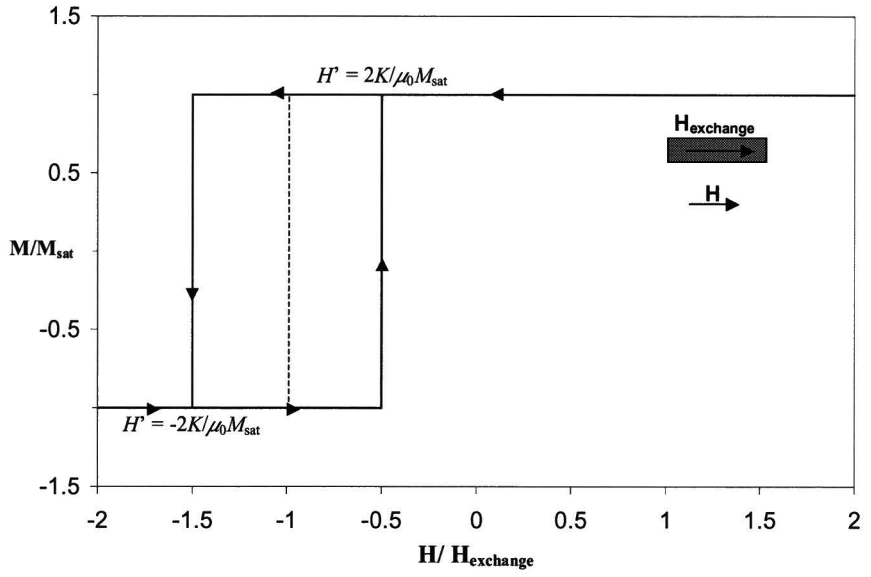

Fig. 2.6: M vs. H curve following from the Stoner-Wohlfarth model with an added term for the description of exchange biasing. The curve is almost the same as in the original Stoner-Wohlfarth model; the difference is the translation of the curve along H, with $H_{exchange}$.

The next situation of interest is when the external magnetic field is in the direction of x_1 ($\phi = \pi/2$). In that case the energy density can be written as

$$u[\theta,\phi=\pi/2] = K\sin^2[\theta] - \mu_0 M_{sat} H \sin[\theta] - A\cos[\theta]. \qquad (2.26)$$

Equation (2.26) is plotted for seven different values of H in Fig. 2.7. Once again the curves are given an offset in energy to separate them visually. Each curve has only one minimum and the magnetization will assume the corresponding θ without any hysteresis. In order to find the minimum of equation (2.26), the first derivative of the energy density to θ is set equal to zero:

$$\frac{\partial u[\theta,\phi=\pi/2]}{\partial\theta} = \frac{2K}{\mu M_{sat}}\sin[\theta]\cos[\theta] - H\cos[\theta] + H_{exchange}\sin[\theta] = 0. \qquad (2.27)$$

Substituting $\theta = \arcsin[M/M_{sat}]$ in equation (2.27) [7] results in:

$$(M - M_{sat})(M + M_{sat})(H - \frac{H_c}{M_{sat}}M)^2 + H_{exchange}^2 M^2 = 0, \qquad (2.28)$$

in which $H_c = 2K/\mu_0 M_{sat}$. If there is no exchange bias, $H_{exchange} = 0$, the solutions of equation (2.28) are:

$$M = M_{sat}, H > H_c,$$

[7] Equation (2.24) rewritten when $\phi = \pi/2$, furthermore we used $\cos[\arcsin[\theta]] = (1 - \theta)^{1/2}$ to calculate (2.28).

$$M = \frac{H}{H_c} M_{sat}, -H_c \le H \le H_c, \qquad (2.29)$$
$$M = -M_{sat}, H < -H_c.$$

If the rectangular ferromagnet is exchanged biased, the solutions of (2.28) are less tractable and only given graphically. For both cases, with exchange bias and without exchange bias, the M vs. H curve is drawn in Fig. 2.8. If we look at the differences between the two curves, we see that the exchange bias does not prevent the magnetization from rotating, at a certain external magnetic field. However, because the exchange interaction wants to keep the magnetization fixed at $\theta = 0$, the angle over which the magnetization rotates is smaller than in the case of no exchange bias.

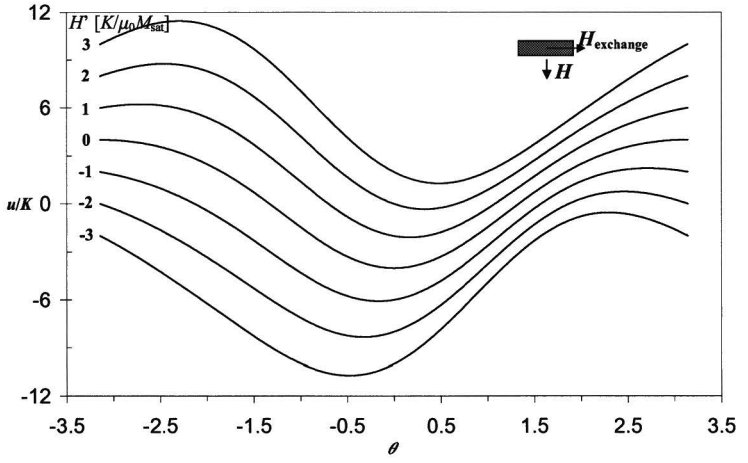

Fig. 2.7: Total energy density versus θ for seven different values of H' when $\phi = \pi/2$. Note that the curve for each H' is given an offset in energy, except the curve for H'=0. This is done to separate the individual curves. All the curves have one minimum, which the magnetization assumes without hysteresis. The M vs. H curve for this configuration is shown in Fig. 2.8.

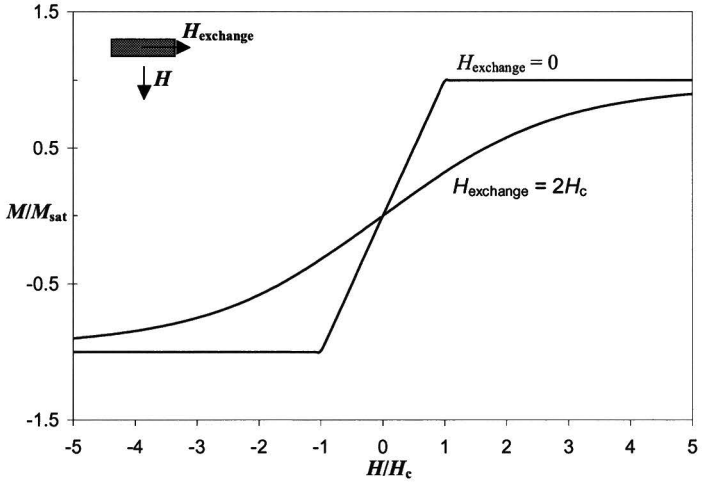

Fig. 2.8: M vs H curve for two different values of $H_{exchange}$, being $H_{exchange} = 0$ and $H_{exchange} = 2H_c$. If we look at the magnetization rotation at a certain external magnetic field, we see that the exchange bias does not prevent the magnetization from rotating. However, it does reduce the angle over which the magnetization rotates.

Concluding paragraph 2.2, we have shown that the thermodynamic rest position of the magnetization of a rectangular ferromagnet is in plane and directed in the longitudinal direction. We have calculated the direction of the magnetization at certain external magnetic fields. This is done for two different directions of the external magnetic field, parallel and perpendicular to the rectangular ferromagnet. In the next paragraph the discussed properties of a rectangular ferromagnet are applied to the bit and a sensor consisting of a number of magnetic layers.

2.3 Magnetic properties of bits

Before discussing the magnetic stray field of a bit, one aspect of its fabrication will be discussed. The bits are rectangular blocks of resist defined with lithography. On top of them a ferromagnetic layer is deposited. A schematic representation of a bit with an additional ferromagnetic layer is drawn in Fig. 2.9.

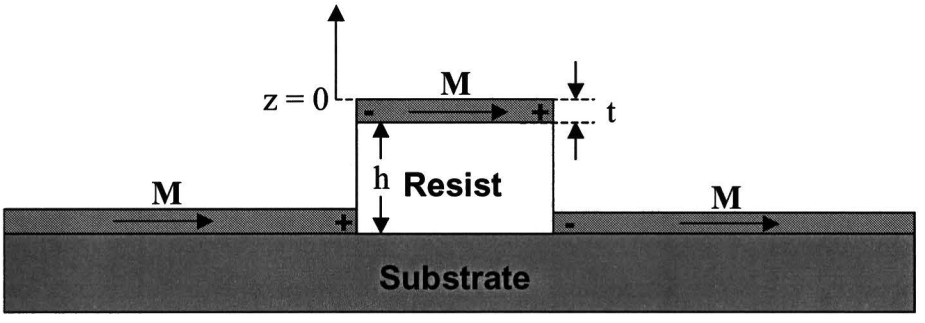

Fig. 2.9: Schematic representation of one bit. The bit is a block of resist with a ferromagnetic layer on top of it. This layer is a rectangular ferromagnet with a minus and plus magnetic pole. However, because the ferromagnetic layer on the substrate abruptly ends where a bit begins, a plus and minus magnetic pole also form on the substrate. The magnetic stray field coming from the substrate can be described with the same equations as the ferromagnetic layer on top of the bit, only with an opposite magnetization.

Since the ferromagnetic layer on the substrate abruptly ends where a bit begins, a plus and minus magnetic pole form on the substrate. Mathematically the magnetic stray field coming from the substrate can be described with the same equations as the ferromagnetic rectangular on top of the bit, only with opposite sign for the magnetization. The magnetic stray field created by one bit is thus not the magnetic field of one rectangular ferromagnet alone, but instead it is the field of two ferromagnetic rectangular layers on top of each other, each with an opposite magnetization.

A last remark, before addressing the magnetic field of a bit, is that the sensor will only be sensitive to magnetic fields in the plane of the sensor, which is the same plane as the bits. Since we assume that $\vec{M}_{\text{bit}} = (0, M, 0)$ we will only discuss H_2.

2.3.1 Magnetic field of one bit

The x_2 component of the magnetic field created by a bit can be written as (see equations (2.14) and (2.15)):

$$H_2[\mathbf{x}] = \sum_{m=0}^{1}\sum_{i=0}^{1}\sum_{j=0}^{1}\sum_{k=0}^{1}(-1)^{i+j+k+m}\frac{M}{4\pi}\arctan\left[\frac{(x_1-y_1)(x_3-y_3)}{(x_2-y_2)\sqrt{(x_1-y_1)^2+(x_2-y_2)^2+(x_3-y_3)^2}}\right],$$

in which y_1, y_2, y_3 should be substituted with:

$$y_1 = w(i-\tfrac{1}{2}),\ y_2 = l(j-\tfrac{1}{2}),\ y_3 = t(k-\tfrac{1}{2})+mh,$$

where w, l and h are respectively the width, length and height of the bit and t and M are respectively the thickness and magnetization of the ferromagnetic layer (see Fig. 2.9). The four summations are necessary to describe the four planes with magnetic charge. In Fig. 2.10 nine plots of H_2 as function of x_1 ($-3w < x_1 < 3w$) and x_2 ($-2l < x_2 < 2l$), at different heights above the bit, are shown. The height z is defined as $z = x_3 - h - t/2$, see Fig. 2.9, which means that $z = 0$ is the top of the bit. The dimensions of the bit are 5 x 1 x 1 μm (l x w x h), the thickness of the ferromagnetic layer is 0.2 μm and the magnetization is $4.3 \cdot 10^3$ G. These values have been chose because they are the expected values in the experiment. To show the magnetic field strength of H_2, cross-sections at $x_1 = 0$ μm of the nine plots in Fig. 2.10, are drawn in Fig. 2.11. If we look at Fig. 2.10, we see that H_2 has four peaks at low heights, a negative and positive peak at the beginning of the bit, and a negative and positive peak at the end of the bit. These peaks indicate the position of the magnetic poles of the magnetic layer. As the distance increases the peak values decrease and the magnetic poles become less visible. At $z = 1$ μm the positive peak has a value of $H_2 = 14$ Oe, this is decreased to 4.3 Oe at a height of z = 2 μm. The value of H_2 right above the bit, at $x_1 = x_2 = 0$ μm, also decreases at increasing height, from $H_2 = 6.6$ Oe at $z = 1$ μm, to $H_2 = 4.1$ Oe at z = 2 μm. This illustrates that the separation distance between the medium and sensor should be as small as possible. A relation between the medium sensor distance and sensor signal has to await the discussion of the sensor sensitivity. First we will investigate the situation of an array of bits, instead of one bit.

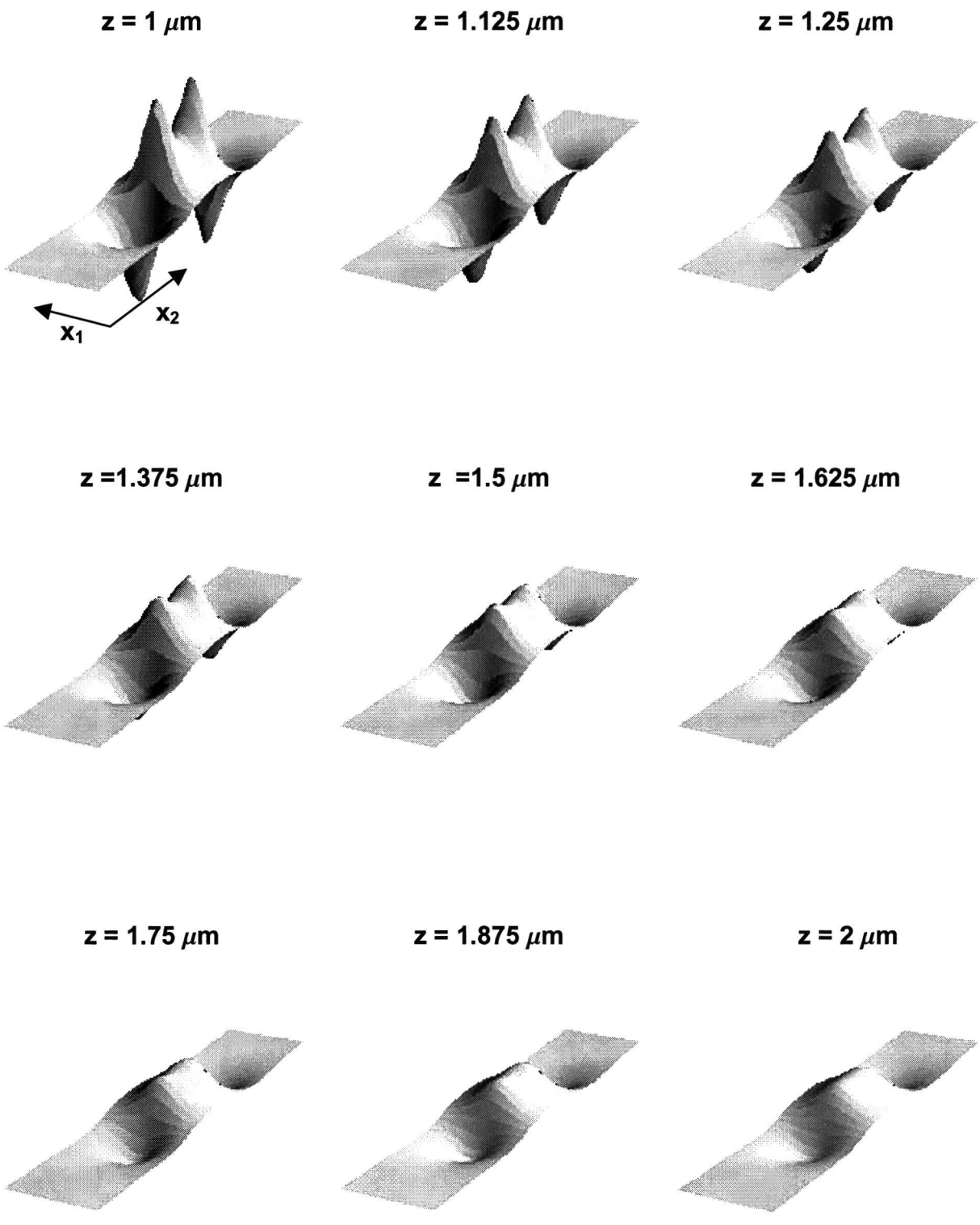

Fig. 2.10: Nine plots of H_2 as function of x_1, x_2 ($-3w < x_1 < 3w$, $-2l < x_2 < 2l$) at different heights z, $z = x_3 - h - t/2$. The dimensions of the bit are 5x1x1μm (lxwxh), the thickness of the ferromagnetic layer, t, is 0.2 μm and the magnetization, $4\pi M = 4.3 \cdot 10^3$ G. The magnetic fields strengths are shown quantitatively in Fig. 2.11, in nine cross-sections for x_1=0 μm.

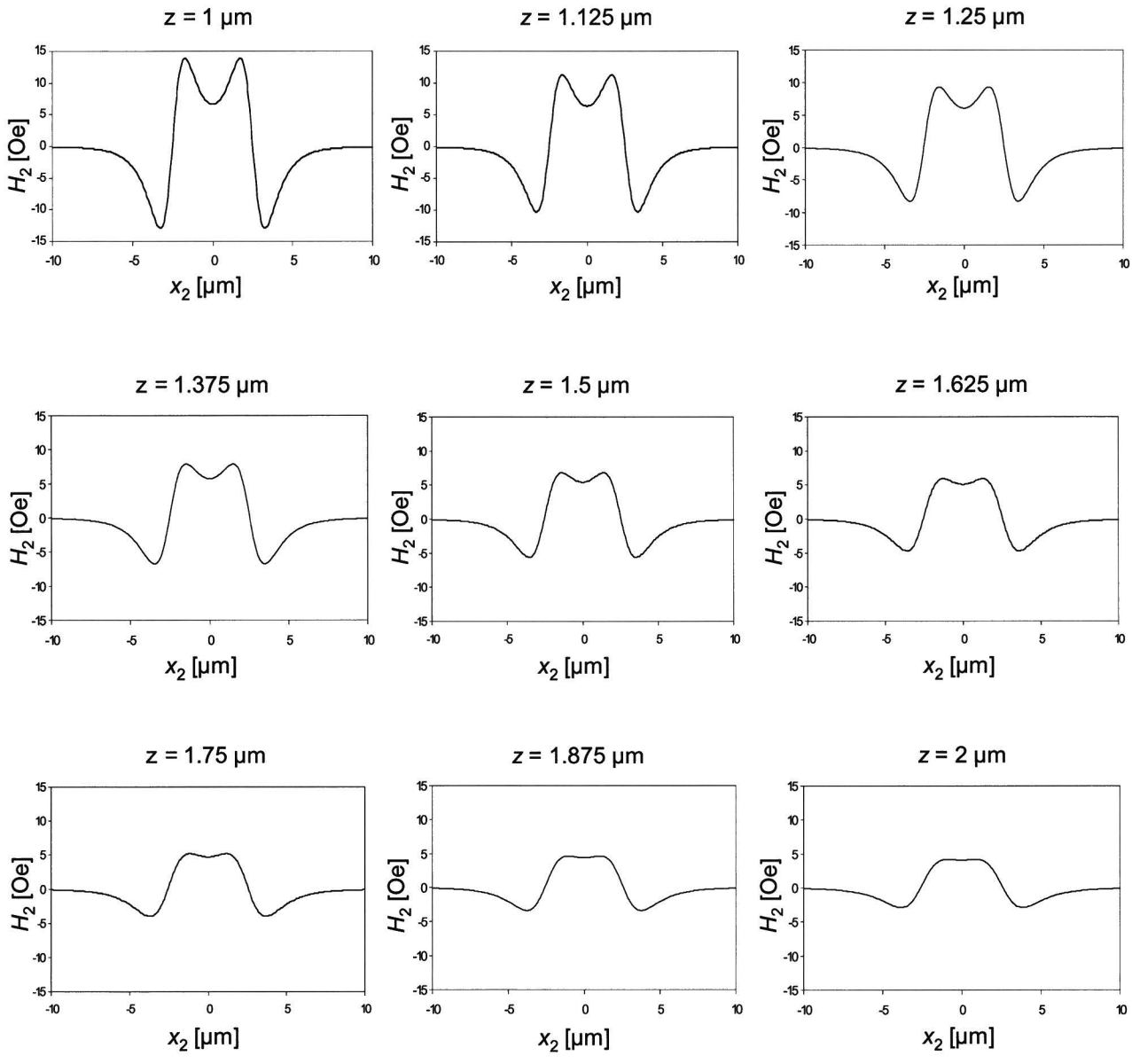

Fig. 2.11: Cross-sections at $x_2 = 0$ μm of the nine plots of H_2 at different heights, shown in Fig. 2.10. We can see that the magnetic field decreases as the height increases.

2.3.2 2 Dimensional array of bits

In the previous section we have calculated the magnetic field coming from one bit. For industrial application of the MROM concept it is important to know the maximum bit density, as this number will largely determine the cost per megabyte. Therefore the total magnetic field created by an array of bits should be calculated. This is done by summing up the individual contributions of all bits in accordance with equation (2.3) and (2.6). Hereby we neglect the interaction between the bits. If we

consider the magnetic bit as a dipole[8] with a magnetic moment of MV, with V the volume of the magnetic material and M the magnetization, we can compare the magnetostatic energy of a bit in the magnetic field of another bit at a distance r, with its shape anisotropy energy. This gives $U_{magn}/U_{anis} = 2(N_1-N_2)V/4\pi r^3$. If we fill in some typical numbers for the experiment, $l = 5$ μm, $w = 1$ μm, $h = 0.1$ μm and r = 2 μm we find $U_{magn}/U_{anis} \cong 2\cdot10^{-3}$. Since the magnetostatic energy is a factor $2\cdot10^{-3}$ less than the anisotropic energy, this justifies the assumption that the bits have almost no interaction.

As illustration, we will calculate the total magnetic field of a 3x3 bit array, where the middle bit is left out. In Fig. 2.12 the array of bits is drawn schematically. The length and width of the bits are 5x1 μm, the pitch[9] in the x_1 direction is 4 μm and the pitch in the x_2 is 7 μm.

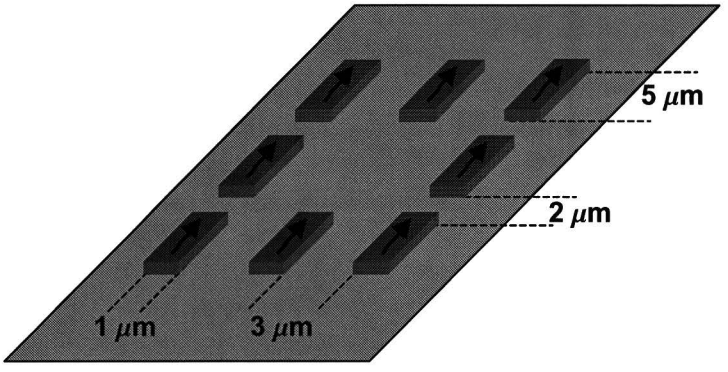

Fig. 2.12: Schematic representation of the 2 dimensional array of bits, used for illustration. The array consists of 3x3 bits, in which the middle bit is missing. The length and width of the bits are 5x1 μm, the pitch in the x_1 direction is 4 μm and the pitch in the x_2 is 7 μm.

In Fig. 2.13 H_2 as function of x_1 (-8 μm < x_1 < 8 μm) and x_2 (-14 μm < x_2 < 14 μm) at three different heights are drawn. Note that the scale of the H_2-axes of each plot is different; this is done because we are interested in the shape of the signal. At the lowest height, $z = 1$ μm, the bit pattern is clearly visible in the periodic structure of H_2. The positive peaks in H_2 indicate the presence of a magnetic pole, and in the middle of the array two positive peaks are missing. At the intermediate height, $z = 3$ μm, H_2 has a valley in the middle of the array, and, although the exact structure of the bit array becomes obscured, we can still see the absence of the middle bit. At the highest height, $z = 5$ μm, we only see two peaks in H_2 and the information about the structure of the middle row is lost.

[8] See reference [9], if the magnetic field of a magnetic dipole is unfamiliar to the reader.
[9] With pitch we mean the characteristic length at which the bit structure repeats it self.

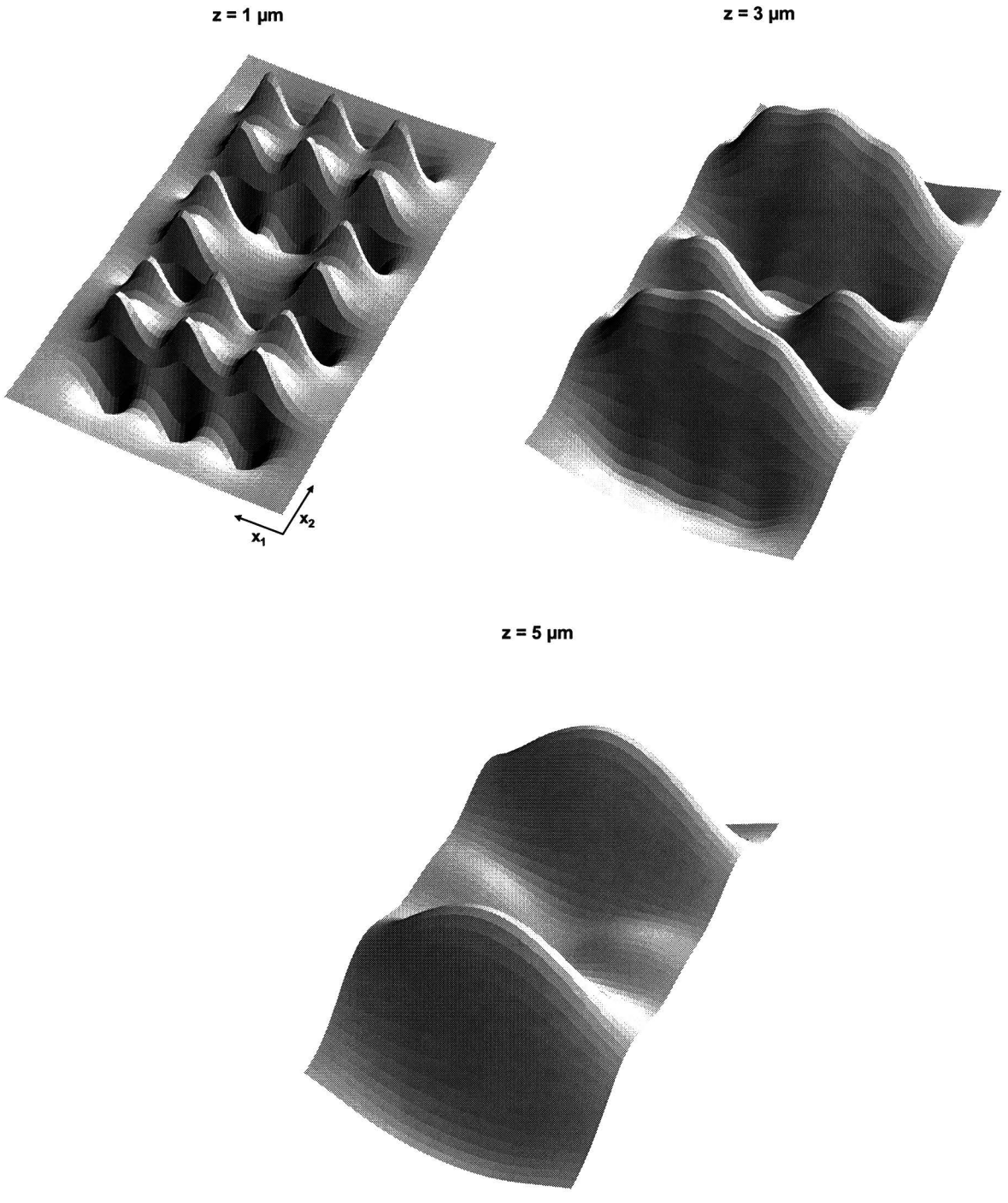

Fig. 2.13: Three plots of H_2 as function of x_1 (-8 μm < x_1 < 8 μm) and x_2 (-14 μm < x_2 < 14 μm) at different heights. The bit pattern is schematically drawn in Fig. 2.12. Note that the scale of the z-axes of each plot is different because we are interested in the shape of the signal. At the lowest height, z = 1 μm, the bit pattern is clearly visible in the periodic structure of H_2. The positive peaks in H_2 indicate the presence of a magnetic pole, and in the middle of the array two positive peaks are missing. At the intermediate height, z = 3 μm, H_2 has a valley in the middle of the array and although the exact structure of the bit array becomes obscured, we can still see that there is no bit present in the middle. At the highest height, z = 5 μm, we only see two peaks in H_2 and the information about the bit structure of the middle row is lost.

The fact that the bit structure of the array become less visible at greater heights is something we expect. If the distance between the sensor and medium is much larger than the distance between two adjacent bits, there is almost no difference in magnitude of the signal of the two bits. To find out how fast the spatial resolution decrease, as the height increase, we can use Fourier analysis. Because we are interested in the magnetic field above the bits, we take the Fourier transform of the magnetic potential (2.5) at coordinates where $\rho_m = 0$,

$$\frac{\partial^2 \Phi_m[k_1,k_2,x_3]}{\partial x_3^2} - 4\pi^2 k^2 \Phi_m[k_1,k_2,x_3] = 0, \tag{2.30}$$

where $\Phi_m[k_1,k_2,x_3]$ denotes the 2-dimensional Fourier transform of $\phi_m[x_1,x_2,x_3]$ and $k^2 = k_1^2+k_2^2$. We can find a general solution of $\Phi_m[k_1,k_2,x_3]$,

$$\Phi_m[k_1,k_2,x_3] = c[k_1,k_2]e^{-2\pi k x_3}, \tag{2.31}$$

in which $c[k_1,k_2]$ is a function independent of x_3. We have placed the magnetic source at $x_3 = -a$ and take $x_3 > -a$, with a being a positive constant. Since the magnetic potential must approach zero when $x_3 \to \infty$ the positive exponential is neglected. A more interesting aspect of (2.31) is that we can write

$$\Phi_m[k_1,k_2,x_3] = \Phi_m[k_1,k_2,0]e^{-2\pi k x_3}, \quad x_3 > 0. \tag{2.32}$$

If we calculate the Fourier transform of the x_2 components of the magnetic field, it follows that,

$$G_2[k_1,k_2,x_3] = \mathrm{FT}(-\frac{\partial \phi_m[x_1,x_2,x_3]}{\partial x_2}) = -ik_2\Phi_m[k_1,k_2,0]e^{-2\pi k x_3} = G_2[k_1,k_2,0]e^{-2\pi k x_3}, x_3 > 0, \tag{2.33}$$

where $G_2[k_1,k_2, x_3]$ is the 2-dimensional Fourier transforms of $H_2[x_1, x_2, x_3]$ and $k = \sqrt{k_1^2 + k_2^2}$. According to equation (2.33) each Fourier component of the magnetic field decays with its own wave number. This means that the components with high wave numbers, describing the small spatial changes of the magnetic field, decay as fastest. This is clearly visible in Fig. 2.13. The peaks in H_2, having a small spatial dimension, disappear as first. At greater heights the signal becomes smoother because the lower wave numbers are dominating. The wave number of our interest is the wave number corresponding to the pitch of the bit array. If that particular component becomes undetectable we cannot discriminate between a one and a zero. In the experiment we will use a bit structure with a pitch of 4 μm in the x_1 direction and 7 μm in the x_2 direction, therefore we expect that the signal decays with $2\pi k = 2\pi\sqrt{k_1^2 + k_2^2} = 2\pi\sqrt{1/4^2 + 1/7^2} = 1.81\mu m^{-1}$. Thus if we increase the height with $1.81^{-1} = 0.55$ μm, we loss a factor e in the Fourier component critical for bit detection. We will use this analysis later, when the sensor sensitivity is known, to make a general statement about the loss of the critical Fourier component with increasing height.

To conclude paragraph 2.3, we have discussed the necessary elements of the processing of a bit in order to calculate its magnetic field. This magnetic field is shown, at different heights, to show its

shape and decay as function of height. This brought us to the conclusion that the medium sensor distance should be as small as possible. We have then shown that we can calculate the magnetic field produced by an array of bits, by summing up the individual contributions of each bit. The calculation shows that it becomes increasingly difficult to resolve the bits at increasing height, even if we can detect the magnetic field. To express this mathematically, Fourier analysis is used to find a relation between the height and the component of the magnetic field, necessary for bit detection. We have shown that it drops a factor e every 0.55 μm, if the pitch of the bit pattern is 4 μm in one direction, and 7 μm in the other direction.

2.4 Sensor

With the magnetic field of the bits known, it is time to turn our attention to the other part of the magnetic theory, which is about the sensor. We will discuss the transport model for the electrons flowing through the sensor and explain where the magnetoresistance comes from, in the case of a MTJ. Then we will address how we can make a sensor, from ferromagnetic and non-ferromagnetic layers and find a description for the sensitivity of such a sensor.

2.4.1 Magnetoresistance and transport model

To understand why the sensor shows magnetoresistance we need to take a look at a MTJ and the layered stack it is made off. In principle an MTJ consists of two ferromagnetic metal layers separated by an isolation layer, which is the third layer. The three layers, and their band energy scheme with the electron wave function, are drawn schematically in Fig. 2.14.

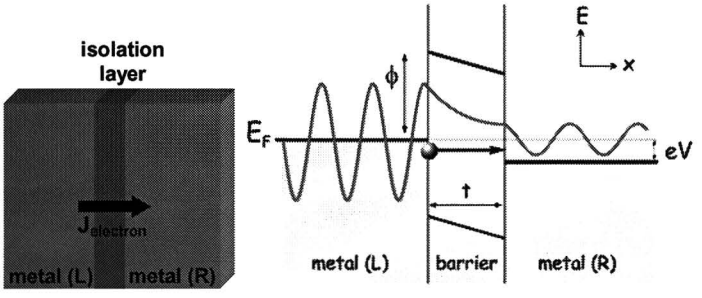

Fig. 2.14: On the left a schematic representation of the two (ferromagnetic) metal layers, separated by an isolation layer, is drawn. On the right the band and energy picture, together with the wave function of the electrons, is drawn schematically. In this picture ϕ is the barrier height, E_f the Fermi level in the metal, V the applied voltage, t the thickness of the isolation layer and e is charge of an electron.

The right metal in Fig. 2.14 is biased with a voltage V with respect to the left metal and electrons will start to tunnel elastically through the barrier. In accordance with [4, 5, 6], we expect the flow of electrons from left to right to be proportional with the available electrons on the left, $N_l[E-eV]f[E-eV]$, the transmission probability, $|T[E]|^2$, and the empty energy states on the right, $N_r[E](1-f[E])$:

$$I_{l\to r}[E,V] \propto N_l[E-eV]f[E-eV]\ |T[E]|^2 N_r[E](1-f[E]), \tag{2.34}$$

where $N_l[E]$ is the density of states of the left metal, $f[E]$ is the Fermi-Dirac distribution and e is the electrical charge of an electron. The flow of electrons in opposite direction can be written in a similar way.

$$I_{r\to l}[E,V] \propto N_l[E-eV](1-f[E-eV])\ |T[E]|^2 N_r[E](f[E]), \tag{2.35}$$

with $N_r[E]$ the density of states of the right metal. The net electron flow going from left to right is the integral over all energies of the difference between equations (2.34) and (2.35)

$$I[V] \propto \int_{-\infty}^{\infty} N_l[E-eV]N_r[E]\ |T[E]|^2 (f[E-eV]-f[E])dE. \tag{2.36}$$

If we assume that the applied voltage V is much lower than the barrier height ϕ ($V << \phi$), only electrons at the Fermi energy are tunneling. The tunnel probability and the density of states can then be taken independent of the energy at the Fermi energy[10]

$$I[V] \propto N_l[E_f]N_r[E_f] \int_{-\infty}^{\infty} f([E-eV]-f[E])dE. \tag{2.37}$$

Equation (2.37) can be reduced further if we assume that $k_bT << eV$ (k_b is the Boltzmann constant, T is the temperature) since then the integral over the Fermi-Dirac distribution will give eV as result, and hence (2.37) will give Ohm's law

$$I/V \propto N_l[E_f]N_r[E_f]. \tag{2.38}$$

This means that the resistance of the two metallic layers, with a thin insulating layer in between, is inversely proportional to the product of the density of states at the Fermi level

$$R \propto \frac{1}{N_l[E_f]N_r[E_f]}. \tag{2.39}$$

Thus far we have been neglecting the fact that the metals are magnetic. To introduce this into our model we introduce a separate density of states for each spin direction. Since a ferromagnet has a net magnetic moment these density of states are shifted in energy with respect to each other[11]. This is illustrated schematically in Fig. 2.15. As a consequence of the shift in the density of states, the density of states at the Fermi energy is different for each spin direction. To see how this leads to

[10] The tunnel probability is omitted in equation (2.37) because it is of no real interest to us. It only needs to be big enough to actual measure any current. In practice this means that the barrier thickness typically should be in the order of nanometers.

[11] The energy shift, or more general the different shapes of the density of states for each spin direction, comes from the consequence of the Pauli exclusion principle on the electrostatic energy of a electron distribution and is called exchange interaction. For more information about exchange interaction see reference [8]

magnetoresistance for the two ferromagnetic layers in Fig. 2.14, we are going to split the tunnel current into a spin up and spin down current. Since the barrier thickness is typically in the order of nanometers it is justified to assume that the spin of the electrons, during tunneling, is conserved. Therefore the spin up and down currents can be taken independent of each other.

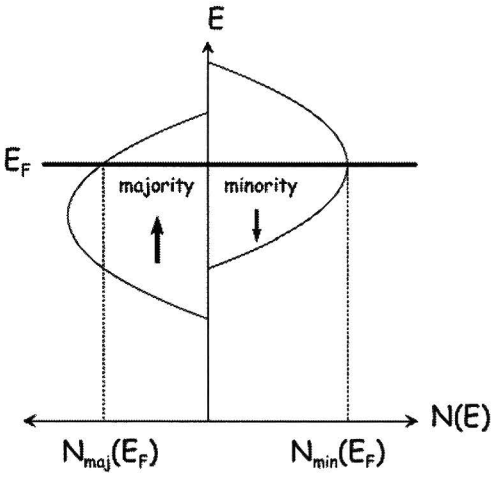

Fig. 2.15: Schematic representation of the shift of the density of states for each spin direction. The imbalance in spin up and spin down electrons leads to a net magnetic moment. Due to the shift the density of states at the Fermi energy is different for each spin direction.

In Fig. 2.16 the two different situations, being parallel and anti-parallel magnetization, are drawn schematically. If the magnetizations of both layers are parallel (top Fig. 2.16) the electrons with majority spin direction tunnel into the majority band and the electrons with minority spin direction tunnel into the minority band. The combined conductance of the two spin currents is then

$$\frac{1}{R_p} \propto N_{maj}^2[E_f] + N_{min}^2[E_f]. \tag{2.40}$$

If the magnetizations of both layers are anti-parallel (bottom Fig. 2.16) the electrons with majority spin direction tunnel into the minority band and the electrons with minority spin direction tunnel into the majority band. The combined conductance of the two spin currents is then

$$\frac{1}{R_{ap}} \propto 2N_{maj}[E_f]N_{min}[E_f]. \tag{2.41}$$

The electrical resistance of a MTJ thus depends on the relative orientation of the magnetization of the ferromagnetic layers. This explains where the magnetoresistance comes from. However this is not the only ingredient for magnetoresistance in an MTJ. For a sensor it is crucial that the two ferromagnetic layers rotate over a different angle, in a certain external magnetic field. Otherwise the anti-parallel orientation cannot be achieved and we will not observe any magnetoresistance. The preferred situation would be if one layer does not rotate at all, while the other is free the rotate. This is accomplished by so called exchange biasing one of the two ferromagnetic layers. This is discussed in the next paragraph.

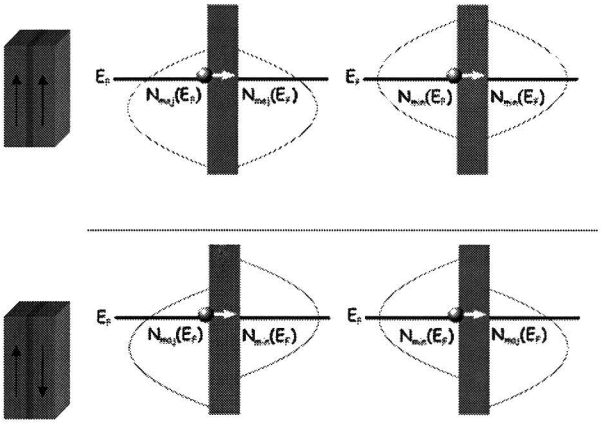

Fig. 2.16: Schematic picture of tunneling for each spin current. If the magnetizations of both layers are parallel (top), the electrons with majority spin direction tunnel into the majority band, and the electrons with minority spin direction tunnel into the minority band. If the magnetizations of both layers are anti-parallel (bottom), the electrons with majority spin direction tunnel into the minority band, and the electrons with minority spin direction tunnel into the majority band.

2.4.2 MTJ stack

In order to get the desired magnetic rotation for the two ferromagnetic layers, we can bias one of them with an antiferromagnet. In an antiferromagnet the individual magnetic moments align themselves into two different magnetic lattices. Within a lattice the magnetic moments align parallel, but moments in the adjacent lattice align anti-parallel (see Fig. 2.17). If a ferromagnet is grown on an antiferromagnet the magnetic moments in the ferromagnet at the interface, will align with the direction of the interface lattice of the antiferromagnet[12]. This is because the exchange interactions between the magnetic moments in an ordered ferromagnet are favoring on overall parallel alignment[13]. In this simplified picture, the direction of the interface lattice of the antiferromagnet will therefore determine the magnetization direction of the ferromagnet. This is schematically shown in Fig. 2.18. This interaction is called exchange biasing, and is the reason the $-A\cos[\theta]$ is included in equation (2.23). We used a $-A\cos[\theta]$ term because it has the lowest energy at $\theta = 0$, and the highest energy at $\theta = \pi$, and it is periodic from 0 until 2π, in accordance with the aforementioned interaction at the interface.

[12] The microscopic origin of the alignment of magnetic moments is exchange interaction. If exchange interaction is unfamiliar to the reader see reference [8].

[13] We ignore the influence of the interface and lattices mismatches and assume that the magnetic moments in the ferromagnet align with the moments in the antiferromagnet, as if it were magnetic moments in the ferromagnet.

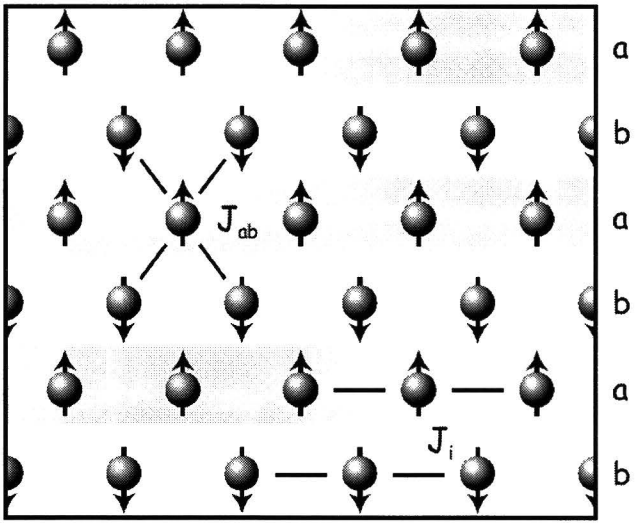

Fig. 2.17: Schematic representation of an antiferromagnet. The antiferromagnet orders into two different lattices denoted a and b. The interaction within each lattice (J_i) is parallel. Where as the interaction between the lattices (J_{ab}) is anti parallel.

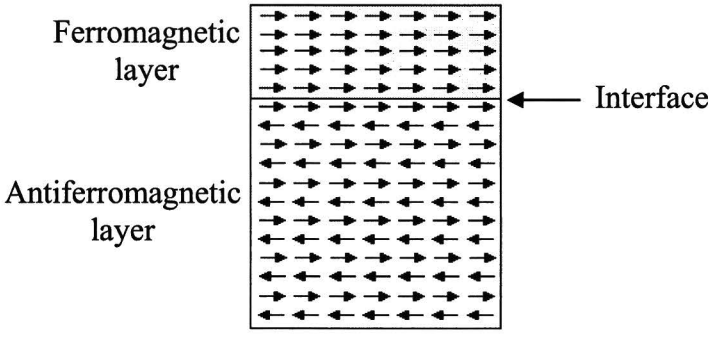

Fig. 2.18: Schematic representation of an exchange biased ferromagnetic layer. At the interface the local magnetization direction of the antiferromagnet, will determine the magnetization direction of the ferromagnet.

Reducing the dipolar coupling in the MTJ

If we exchange bias one of the two ferromagnetic layers of the MTJ, we know the magnetization rotation of that layer in an external magnetic field. In section 2.2.2 we have shown that the magnetization will not rotate, as long as the external magnetic field is smaller than $H_{exchange}$, assuming that the external magnetic field is in the same direction as the exchange bias. This means that the magnetoresistance solely depends on the magnetization rotation of the unbiased ferromagnetic layer. Since the sensor must be sensitive to small magnetic fields, the unbiased ferromagnetic layer must rotate at small magnetic fields. To see that this is not the case in a realistic sample structure of finite area, where we simply exchange bias one of the magnetic layers, we have to take a look at Fig. 2.19. The biased ferromagnetic layer influences the unbiased ferromagnetic layer through its magnetic stray field. This is illustrated in the left part of Fig. 2.19. Placing an extra ferromagnetic layer in the MTJ stack, near the biased layer, can reduce this magnetic stray field, if it has opposite magnetization. This is accomplished by separating the biased ferromagnetic layer and the extra ferromagnetic layer, with a non-magnetic metal spacer. The non-magnetic metal spacer must be thin enough for the wave functions of the mobile s

electrons, in both ferromagnetic layers, to have overlap. This overlap results in an interface exchange interaction that aligns the two ferromagnetic layers anti-parallel. Because of this anti-parallel configuration their combined magnetic moment, and thus combined magnetic stray field, is almost zero. This reduces the interaction between the top ferromagnet and the rest of the stack to almost zero. This is illustrated in the right part of Fig. 2.19.

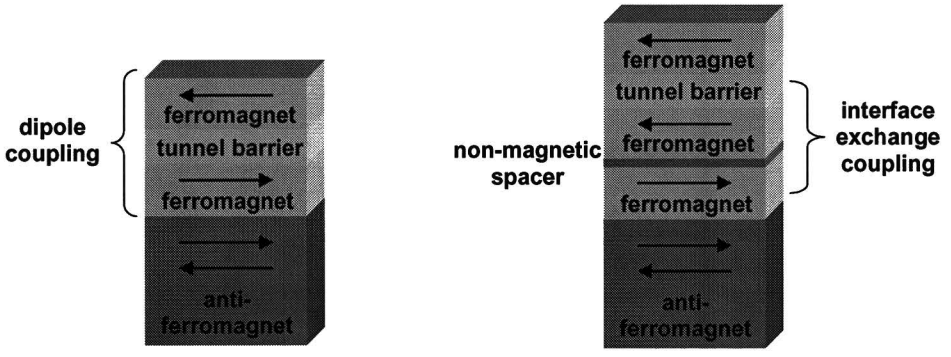

Fig. 2.19: In the left situation the biased ferromagnetic layer will create a magnetic field, which interacts with the ferromagnetic layer on the other side of the tunnel barrier. In the right situation, a non-magnetic spacer and an extra ferromagnetic are inserted between the biased ferromagnetic layer and the tunnel barrier. The extra ferromagnetic layer and the biased ferromagnetic layer will align anti-parallel. Therefore is the sum of their magnetic moment, and magnetic stray field, almost zero. This reduces the interaction between the top ferromagnet and the rest of the stack to almost zero.

We emphasize that, although the M vs. H curve of the right stack in Fig. 2.19 is complex, the R vs. H curve is not. It is determined by the orientation of the magnetizations of the two ferromagnetic layers adjacent to the tunnel barrier. The ferromagnetic layer under the tunnel barrier is exchange biased, via the non-magnetic spacer, and does not rotate in an external magnetic field, at least not in the magnetic fields of the bits. The ferromagnetic layer on top of the tunnel barrier, however, is free to rotate in an external magnetic field. The magnetoresistance can therefore be described with a simple model, taking into account the magnetization rotation of a ferromagnetic rectangular in an external magnetic field. This will be done in the next paragraph.

2.4.3 Sensor sensitivity

From now on we will refer to the exchange biased ferromagnetic layer as the fixed layer, while the other ferromagnetic layer will be referred to as the free layer. The sensor configuration of the free and fixed layer is schematically drawn in Fig. 2.20. This configuration is chosen, because it ensures that the fixed layer does not rotate as long as the external field is smaller than $H_{exchange}$. This is because the exchange bias is in the same direction as the external field; see Fig. 2.6 for the corresponding M vs. H curve. The magnetization of the free layer, on the other hand, rotates at small magnetic fields, because the external magnetic field is perpendicular to its magnetization. For this case the corresponding M vs. H curve is shown in Fig. 2.8 for $H_{exchange} = 0$. This way an analog sensor is produced, that is sensitive to small magnetic fields. The magnetoresistance can be related to the component of the magnetization of the free layer, in the magnetization direction of the fixed layer. Since the magnetization of the fixed layer and the external magnetic field are in the same direction, this coincides with the definition of M made in the theory, see equation (2.24). The

MR curve of the sensor is therefore the same as the M vs. H curve plotted in Fig. 2.8 for $H_{exchange}$ = 0. The only difference is that the scale on the vertical axis is that of resistance, instead of magnetization. In Fig. 2.21 the theoretical MR curve for the sensor is drawn. The quantities used in Fig. 2.21 are defined as follows, $R_0 = (R_{ap} + R_p)/2$, $\Delta R = (R_{ap} - R_p)/2$ and H_c^{free} is the coercive magnetic field of the free layer.

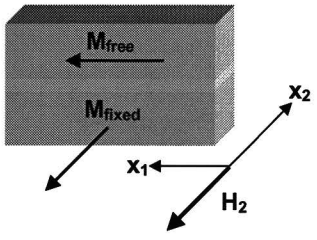

Fig. 2.20: Schematic representation of the sensor configuration. The fixed layer is exchanged biased into the x_2 direction. The magnetization of the free layer is directed into the x_1 direction, at H_2=0 Oe, due to the shape anisotropy of the free layer. In this configuration the sensor is linear around zero external field. The corresponding MR curve is shown in Fig. 2.21.

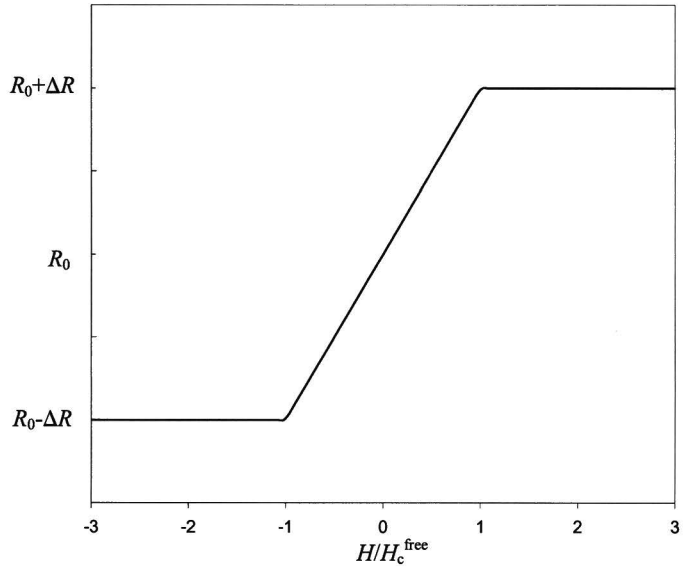

Fig. 2.21: Theoretical magnetoresistance curve of the sensor. The corresponding sensor configuration is shown in Fig. 2.20.

We are particularly interested in the sensor sensitivity at H = 0 Oe, which can be written as,

$$\frac{\partial R_{MTJ}}{\partial H}\Big|_{H=0} = \frac{2\Delta R}{2H_c^{free}} = \frac{\Delta R}{M_{free}(N_1 - N_2)}, \qquad (2.42)$$

where we used $K = (\mu_0/2)M_{free}^2(N_1\text{-}N_2)$. Equation (2.42) gives the expected electrical resistance change of the MTJ at a certain magnetic field.

In conclusion, in paragraph 2.4 we have discussed the transport model explaining the magnetoresistance of a MTJ and found that it depends on the relative orientation of the two

ferromagnetic layers adjacent to the tunnel barrier. It is then explained how to create a fixed and free layer in the MTJ stack so that it can be used as sensor. The orientation of the fixed and free layer is discussed and explained why it is chosen in this particular form. This resulted in a description of the sensor sensitivity, which will be used in the next paragraph.

2.5 Expected performance and critical factors

In order to determine the performance of the MROM concept we have to set a lower bound to the signal we can detect. Since we are detecting electrical signals of a tunnel resistor we set the lower bound at the Johnson-Nyquist[14] noise of the sensor,

$$V_{\text{noise}} = \sqrt{4k_b T R_{\text{MTJ}} \Delta f}\,, \tag{2.43}$$

where V_{noise} is the amplitude of the noise signal, k_b is Boltzmann constant, T is the temperature, R_{MTJ} is the resistance of the sensor and Δf is the spectral bandwidth of the measuring setup. If we are measuring with constant current (I_{measure}) this relates to an noise in the resistance of

$$R_{\text{noise}} = \frac{V_{\text{noise}}}{I_{\text{measure}}} = \frac{\sqrt{4k_b T\, R_{\text{MTJ}} \Delta f}}{I_{\text{measure}}}. \tag{2.44}$$

In order to get a quantitative prediction about the signal during the experiment we are going to calculate R_{noise} and the sensitivity of the sensor for realistic numbers at room temperature. These realistic numbers are, $\Delta f = 10$ Hz, $R_{\text{MTJ}} = 10$ kΩ, and $I_{\text{measure}} = 1$ μA. This gives an R_{noise} of $40 \cdot 10^{-3}$ Ω. For the sensor sensitivity the realistic numbers are, $4\pi M_{\text{free}} = 15 \cdot 10^3$ G, $\Delta R = 1.8$ kΩ[15]. Using equation (2.18) with $b_1 = 1$ μm, $b_2 = 5$ μm, $b_3 = 15$ nm to calculate $(N_1 - N_2)$ we find,

$$\frac{\partial R_{\text{MTJ}}}{\partial H}\Big|_{H=0} = 13.4 \frac{\Omega}{Oe}, \tag{2.45}$$

for the sensor sensitivity. This means that, magnetic fields smaller than, $40 \cdot 10^{-3} / 13.4 = 3$ mOe, are undetectable because they get lost in the noise. However, the order of magnitude of the expected signal from our micrometer sized bits, see Fig. 1.3 and Fig. 2.11, is a factor 10^3 larger, and we should be able to detect bits when performing the experiment.

As was already pointed out in 2.3 the distance between the medium and the sensor is of crucial importance. With the sensor sensitivity known, we can try to predict the largest distance, at which we can detect individual bits. For that purpose equation (2.33) is written as function of the scaled coordinates $\xi = (x_1/p1, x_2/p_2, z/p_3)$,

[14] Johnson-Nyquist noise is due to the random movement of the conduction electrons if we envision them as a free electron gas.

[15] Corresponds with a R_0 of 10 kΩ and a MR of 20%.

$$G_2[\kappa_1,\kappa_2,\xi_3] = G_2[\kappa_1,\kappa_2,0]\exp[-2\pi\sqrt{(\frac{p_3}{p_1}\kappa_1)^2+(\frac{p_3}{p_2}\kappa_2)^2}\,\xi_3], \qquad (2.46)$$

in which p_i denotes the pitch of the bits in the i-th direction and $\kappa_i = p_i k_i = 1/\xi_i$ is the scaled wave number. We will take p_3 equal to h, the height of the bit. A numerical calculation of the Fourier component $G_2[1,1,0]$ is done in appendix 7.3 for a two-dimensional infinite bit array of ones. The calculation is done at $p_3/p_1 = 1/4$ and $p_3/p_2 = 1/7$, all other relevant parameters are listed in appendix 7.3. This gives a value of $G_2[1,1,0]=1.8\cdot10^{-3}M = 7.74$ Oe, when $4\pi M = 4.3\cdot10^3$ G. Substituting these numbers into equation (2.46) and assuming that the Fourier component $G_2[1,1,\xi_3]$ has to be 10^2 times larger than the signal due to noise, we can calculate ξ_3 to be,

$$\xi_3 = -\frac{1}{1.81}\log[\frac{0.29}{7.74}] = 1.79, \qquad (2.47)$$

before the component critical for bit detection is lost in the noise. Because $p_3 = h = 1$ μm and $z = p_3\xi_3$, this relates to a distance of 1.79 μm between the sensor and medium. In the experiment we should at least get as close as this, otherwise we do not expect to retrieve the bit pattern.

As last remark we note that expression (2.47) illustrates what one of the difficulties is when we want to increase the data capacity. If we make all the pitches twice as small, we also need to reduce the distance between the sensor and medium with a factor two. In fact, as long as the ratios of the pitches and all other parameters do not change, expression (2.47) tells us that the maximum distance between sensor and medium reduces by the same factor as the pitches. We can get a high bit density, but then the distance between medium and sensor becomes small. This illustrates the importance of the distance between the medium and sensor in the experiment.

2.6 Interferometer

In the previous part of the theory it is concluded that the separation distance between the medium and the sensor is a critical factor in the experiment. However, before we can determine this distance, the medium and sensor plane have to be set parallel. Monochromatic interferometry and white light interferometry are used to measure both relevant experimental quantities (parallelism and distance). In the remainder of this paragraph, the theory of interferometry is described in detail and how it is applied in the MROM experimental setup.

2.6.1 Fizeau interferometer

In Fig. 2.22 the medium plane and sensor plane are shown schematically, assuming that there is tilt in only 1 direction.

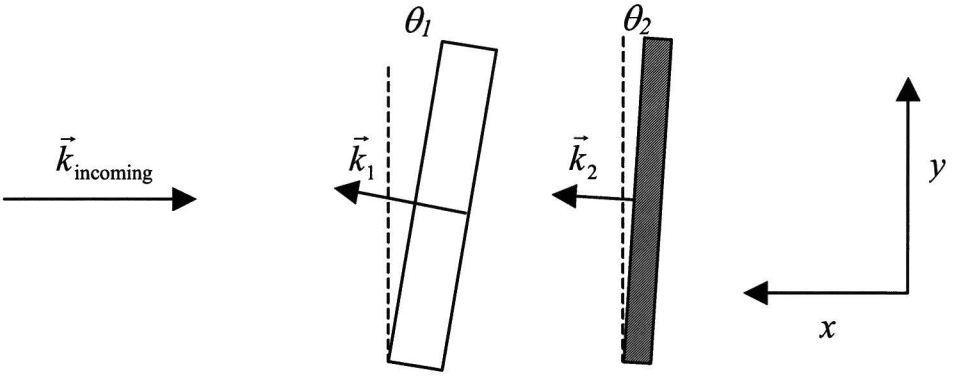

Fig. 2.22: Plane 1 is the plane of the medium and plane 2 is the sensor plane. Plane 1 will reflect a part of the light specular, and it will transmit a part of the light. The transmitted light will reflect specular on the silicon sensor plane. The wave reflected at the front side of the glass is neglected, because we assume that its wave vector is equal to k_1.

The front and backside of the medium are assumed to be parallel. Therefore the reflection at the front side of the medium is neglected. The reflected light beams can be described by plane waves,

$$\left|\vec{E}_1\right| \propto E_1 e^{i(\vec{k}_1 \cdot \vec{r} - \omega \cdot t)} \tag{2.48}$$

$$\left|\vec{E}_2\right| \propto E_2 e^{i(\vec{k}_2 \cdot \vec{r} - \omega \cdot t)} \tag{2.49}$$

where E_1 and E_2 are the amplitudes, $\vec{k}_1$ and $\vec{k}_2$ the wave vectors and ω the radial frequency of the reflected light waves. The vector $\vec{r}$ is the position vector on the detector and t is the time. Since the polarization is not changed during the reflections the light can be treated as if it were a scalar. The intensity of the reflected light is

$$I \propto E \cdot E^* = E_1^2 + E_2^2 + 4E_1E_2 \cos[(\vec{k}_1 - \vec{k}_2) \cdot \vec{r}]. \tag{2.50}$$

The wave vectors for both waves can be replaced with:

$$\vec{k}_1 = \frac{2\pi}{\lambda}(\cos\theta_1, \sin\theta_1), \tag{2.51}$$

$$\vec{k}_2 = \frac{2\pi}{\lambda}(\cos\theta_2, \sin\theta_2), \tag{2.52}$$

where λ is the wavelength and θ_1 and θ_2 are the angles of the medium and sensor with the y-axis, they are depicted in Fig. 2.22. Substituting these two equations into equation (2.50) gives:

$$I \propto E \cdot E^* = E_1^2 + E_2^2 + 4E_1E_2 \cos[\frac{2\pi}{\lambda}((\cos\theta_1 - \cos\theta_2)x + (\sin\theta_1 - \sin\theta_2)y)]. \tag{2.53}$$

If we replace the cosine and sine with the first term of their Taylor expansion, which is justified for very small angles, we obtain:

$$I \propto E \cdot E^* = E_1^2 + E_2^2 + 4E_1E_2 \cos[\frac{2\pi}{\lambda}(\theta_1 - \theta_2)y]. \quad (2.54)$$

Equation (2.54) describes the intensity distribution on the detector, as a function of the y coordinate on the detector. It allows us to relate the tilt between the medium and sensor with the observed oscillations on the detector. From it we can deduce that n oscillations in the intensity, over a distance W on the detector, relates with the tilt in the following manner:

$$W = n \cdot period = \frac{n \cdot \lambda}{\theta_1 - \theta_2}. \quad (2.55)$$

If we make sure, by adjusting the experimental setup, that we observe only ½ a wavelength (thus n = ½) we can calculate θ_1-θ_2 to be:

$$\theta_1 - \theta_2 = \frac{\lambda}{2 \cdot W}. \quad (2.56)$$

This analysis is easily extended into 3 dimensions, which gives a similar relation as equation (2.54) including the angles perpendicular on the x-y plane.

2.6.2 White light interferometer

The monochromatic interferometer, described in the preceding section, only gives information about the relative tilt between the medium and sensor, not about the absolute distance between them. This is not directly obvious from equation (2.50), since the medium and sensor are both positioned at an arbitrary distance from the detector. In order to take the distance between them into account, the situation is drawn schematically in Fig. 2.23.

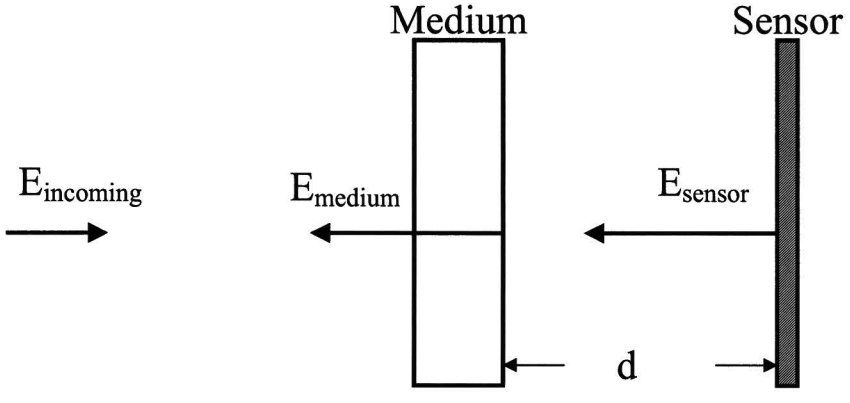

Fig. 2.23: Schematic representation of medium and sensor. The incoming light is partly reflected (specular) and partly transmitted at the glass-air interface. All the transmitted light is reflected (specular) at the silicon. We assume that the two planes are parallel to each other.

If the detector is placed somewhere at the left of Fig. 2.23, the light waves reflected at the medium-air interface and at the sensor, will have phase difference corresponding with two times the distance between them. The electrical field of the reflected light can be described with[16]

$$E = E_{\text{medium}} e^{ik(x-ct)} + E_{\text{sensor}} e^{ik(x+2d-ct)}, \qquad (2.57)$$

in which E_{medium} and E_{sensor} are the amplitudes of the light reflected at respectively the medium-air interface and the sensor, x is the distance from the backside of the glass to the detector, c is the velocity of light and d is the distant between the backside of the medium and the sensor. The signal of the detector is proportional with the intensity of the light, which is given by

$$I = E \cdot E^* = \left|E_{\text{medium}}\right|^2 + \left|E_{\text{sensor}}\right|^2 + E_{\text{medium}}\, E_{\text{sensor}}\, 2\cos[2kd]. \qquad (2.58)$$

According to equation (2.58) the intensity is an oscillating function of the wave number k, with a period of π/d. This allows us to determine the sensor medium separation distance, by detecting the period of the oscillation in the reflected spectrum. Notice that this requires a light source, which emits light in a range of wavelengths. We will use a halogen lamp in our experimental setup.

Coherence length and spectral distributions

Equation (2.58) is an oversimplification of what is really happening. It would only be valid if the detection window of the spectrometer, $F[k]$, were infinitely narrow (Dirac function), which is not the case. In Fig. 2.24 the typical response of the spectrometer to a monochromatic light source is drawn, it is measured with a laser beam ($\lambda = 635$ nm). Instead of a Dirac function it is a Gaussian distribution

$$F[k] = \exp[-\frac{(k-k_0)^2}{2\Delta k^2}]. \qquad (2.59)$$

In equation (2.59) k is the wave number, k_0 is the wave number of the incident light and Δk is a measure of the width of the peak.

[16] Note the difference in the way the phasor is written down with respect to equation (2.48). This is done, anticipating on the coherence length, to show the dependence on k unambiguous. The existence of the coherence length is the reason we can neglect the reflection of light at the front side of the glass. The thickness of the glass will turn out to be bigger then the coherence length in our setup.

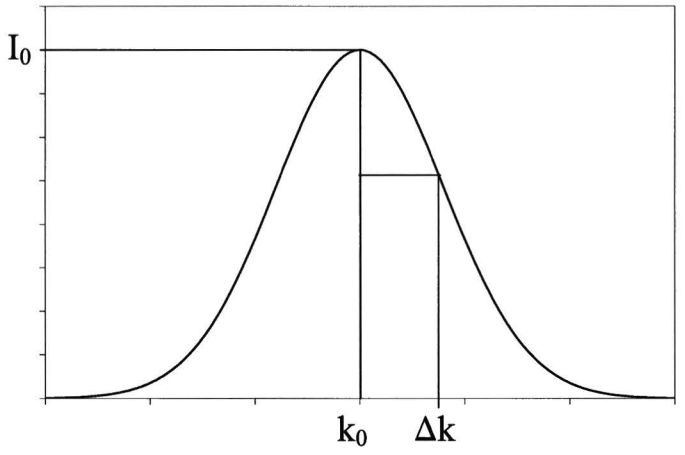

Fig. 2.24: Typical response of spectrometer when illuminated with monochromatic light. The response has the shape of a Gaussian distribution.

Since a broad range of wave numbers is present in the light, we have to take into account that we are not measuring the intensity of a monochromatic wave. Instead we are measuring the intensity produced by a wave packet for which the wave number distribution is given by equation (2.59). The electric field build up from such a distribution can be described with[17]

$$E = E_{\text{medium}} \int_{-\infty}^{\infty} F[k] e^{ik(x-ct)+i\phi[k]} dk + E_{\text{sensor}} \int_{-\infty}^{\infty} F[k] e^{ik(x+2d-ct)+i\phi[k]} dk \quad (2.60)$$

The function $\phi[k]$ describes the phase of each wave number and is, by definition, a random fluctuating function of k. This random fluctuating function expresses the randomness of the light emitted by a halogen lamp. It will be better defined a bit later. Using the electric field in equation (2.60) to calculate the intensity gives

$$\begin{aligned} I = E \cdot E^* = {} & |E_{\text{medium}}|^2 \int_{-\infty}^{\infty}\int_{-\infty}^{\infty} F[k]F[k'] e^{i(k-k')(x-ct)+i(\phi[k]-\phi[k'])} dkdk' + \\ & |E_{\text{sensor}}|^2 \int_{-\infty}^{\infty}\int_{-\infty}^{\infty} F[k]F[k'] e^{i(k-k')(x+2d-ct)+i(\phi[k]-\phi[k'])} dkdk' + \\ & E_{\text{medium}}\, E_{\text{sensor}} \int_{-\infty}^{\infty}\int_{-\infty}^{\infty} F[k]F[k'] e^{i(k-k')(x-ct)-2dk'+i(\phi[k]-\phi[k'])} dkdk' + \\ & E_{\text{medium}}\, E_{\text{sensor}} \int_{-\infty}^{\infty}\int_{-\infty}^{\infty} F[k]F[k'] e^{i(k-k')(x-ct)+2dk+i(\phi[k]-\phi[k'])} dkdk' . \end{aligned}$$

[17] Although the electric field should be a discreet sum over all the wave numbers it is assumed that the wave numbers are so closely packed that the sum can be described with an integral.

Now we state that $\phi[k]$ is by definition such a random fluctuating function, that the only contribution to the intensity is at $k = k'$, all other contributions will add up to zero. The intensity will then reduce to

$$I = |E_{\text{medium}}|^2 \int_{-\infty}^{\infty} F^2[k]dk + |E_{\text{sensor}}|^2 \int_{-\infty}^{\infty} F^2[k]dk + 2E_{\text{medium}}\ E_{\text{sensor}} \int_{-\infty}^{\infty} F^2[k]\cos[2dk]dk\,. \quad (2.61)$$

From equation (2.61) we can see, that if the detection window of the spectrometer were a Dirac pulse, then equation (2.58) would have been correct. However, inserting the proper Gaussian distribution into equation (2.61) gives

$$I = \Delta k\sqrt{\pi}(|E_{\text{medium}}|^2 + |E_{\text{sensor}}|^2 + 2E_{\text{medium}}\ E_{\text{sensor}} \exp[-\Delta k^2 d^2]\cos[2k_0 d])\,. \quad (2.62)$$

Equation (2.62) shows that the intensity is still an oscillating function of k_0, however the oscillation is damped. If the distance between the medium and sensor increases, the amplitude of the oscillation decreases and will eventually disappear. The separation distance at which the oscillation disappear, is called the coherence length and can be defined as[18],

$$\Lambda = \frac{\lambda^2}{\Delta\lambda}, \quad (2.63)$$

in which Λ is the coherence length and $\Delta\lambda$ is the detection window of the spectrometer. As long as the separation distance is smaller than the coherence length, we can use white light interferometry to determine it. If the separation distance is larger, the oscillations in the spectrum are gone and the information about it is lost[19].

Multiple reflections

Anticipating the composition of the sensor, we will address the influence of the SiO_2 layer in which the MTJ elements are embedded, on the detected spectrum. The medium and sensor are drawn schematically in Fig. 2.25; the incident light is drawn under an angle in order to separate the multiple reflections visually. In the calculation a normal incidence is assumed. The SiO_2 layer adds an extra interface at which light reflects and transmits. This will create extra oscillations with different periods in the spectrum. If we take all the reflections into account we can write,

$$E = I[k](r_{12}e^{ik_1x} + t_{12}t_{21}e^{i(k_1x+2d_2k_2)}\sum_{n=0}^{\infty} r_{23}^n r_{21}^n e^{i2d_2k_2n}(r_{23} + t_{23}t_{32}e^{i2d_3k_3}\sum_{m=0}^{\infty} r_{32}^m e^{i2d_3k_3m})), \quad (2.64)$$

[18] In most literature the coherence length is defined as the distance needed to create a phase difference of 2π between the smallest and biggest wavelength present in the light. This is used in the derivation of equation (2.63).

[19] To justify footnote 16 we will calculate Λ for the biggest wavelength, λ_{max} = 900 nm, present in the light. The resolution of the used spectrometer is $\Delta\lambda$ = 1.5 nm. This gives Λ = 0.54 mm, since the medium is 4 mm thick we can neglect the influence of the front side of the medium.

for the reflected light. In equation (2.64) r_{ij} and t_{ij} are respectively the reflection and transmission coefficient for a wave propagating through medium i at the interface with medium j. The wave number in each medium i, is given by $k_i = n_i k$, with n_i the refraction index of medium i and k the wave number in air. The thickness of medium i is given by d_i. The intensity spectrum of the incident light is given by $|I[k]|^2$.

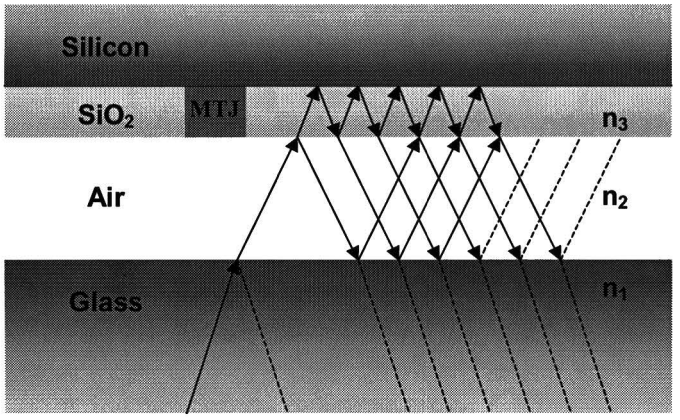

Fig. 2.25: Schematic representation of the sensor with one MTJ element, which is embedded in a SiO_2 layer. The incident light is drawn under an angle in to separate the multiple reflections visually. In the calculation a normal incidence is assumed. Each interface reflects and transmits light, creating multiple reflections, which lead to oscillations with different periods in the spectrum.

The reflection and transmission coefficient, in the case of normal incidence light, are given by the Frensel equations[20],

$$r_{ij} = \pm\frac{n_i - n_j}{n_i + n_t}, \tag{2.65}$$

$$t_{ij} = \frac{2n_i}{n_i + n_j}. \tag{2.66}$$

The plus sign in equation (2.65) applies to light with a polarization perpendicular to the plane of incidence, and the minus sign belongs to light with a polarization parallel to the plane of incidence. We will not pursue the subject of multiple reflections any further at this point. Instead we will return to it later in the experimental results, to determine which terms in equation (2.64) should be taken into account and which can be neglected.

In conclusion of paragraph 2.6, we have shown that we can use the monochromatic interferometer to align the medium and sensor parallel to each other, and we found a expression for the minimal obtainable theoretical tilt between them. This is further generalized to the case of white light interferometry and it is explained how this can be used to detect the distance between the medium and sensor. Two complicating matters, coherence length and multiple reflections, are briefly discussed to describe their influence on the experiment.

[20] For more information about the Fresnel equations see reference [1] on page 94.

3 Experiment

This chapter starts with a discussing of the experimental requirements. The next subject is the processing of the sensor and medium. With the details of them know we can address the subjects drawn schematically in Fig. 3.1. In the upper left corner the calibration is shown. This setup is built for calibrating the TMR sensors with a known external magnetic field. In the upper right corner the MROM experimental setup is drawn, it is necessary for manipulating the medium and sensor on a micrometer scale. In the bottom the interferometer is displayed, it is developed for determining the alignment of, and distance between, the medium and sensor.

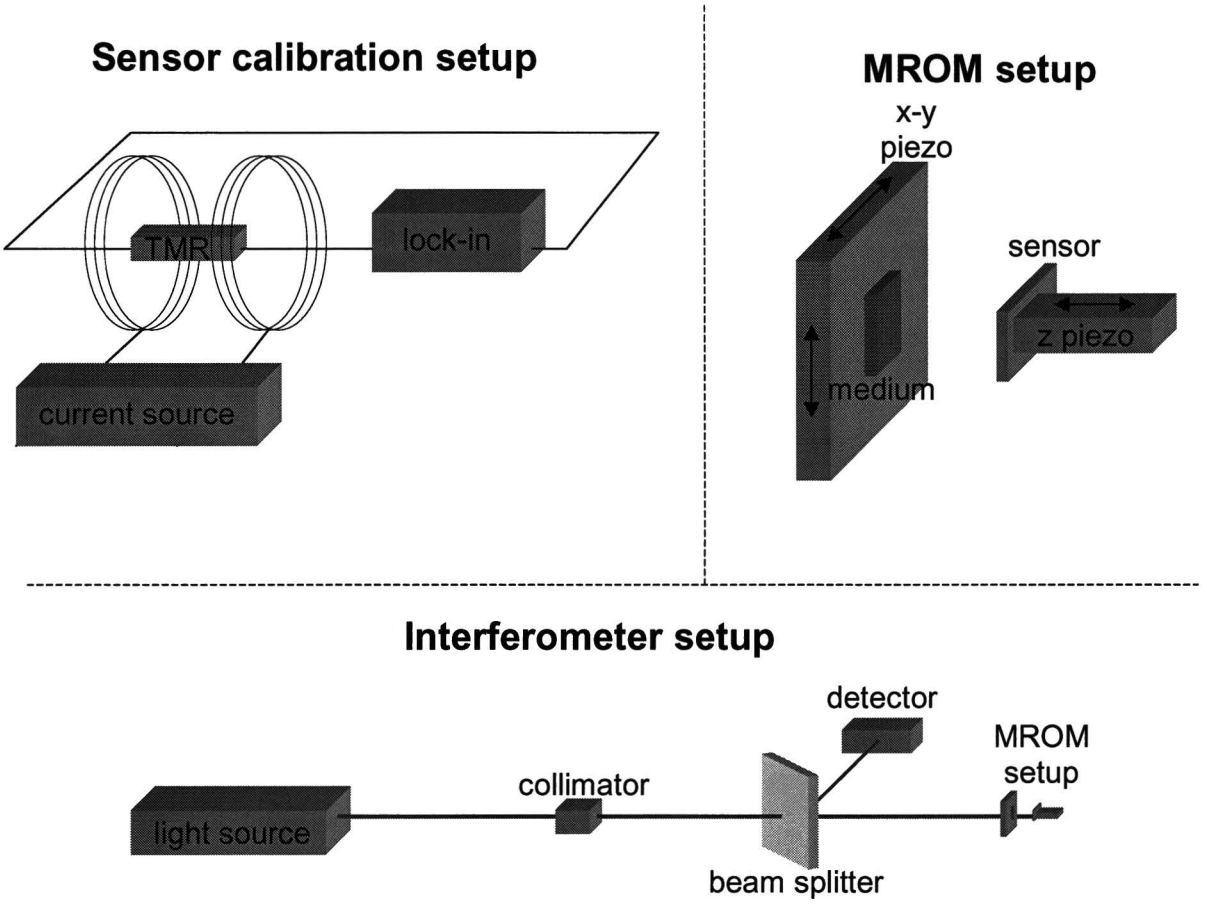

Fig. 3.1: Schematic picture of the sensor calibration, MROM and interferometer setup. In the upper left corner the sensor calibration is shown. This part is built for calibrating the TMR elements with an (known) external magnetic field. In the upper right corner the MROM experimental setup is drawn, it is necessary for manipulating the medium and sensor on a micrometer scale. In the bottom the interferometer is shown. It is created for determining the alignment of, and distance between, the medium and sensor.

3.1 Experimental requirements

The interferometers should be able to align the medium and sensor parallel, and measure the separation distance between them. With parallel we mean a height difference of 10 nm per

(approximately) 2 bits. Since the biggest pitch of the bit pattern is 7 μm, this corresponds to a minimal tilt of $7 \cdot 10^{-4}$ rad between the two planes. If we fill in realistic numbers used in the experimental setup ($\lambda = 635\ nm$ and $W = 4$ mm) in equation (2.56),

$$\theta_1 - \theta_2 = \frac{\lambda}{2 \cdot W} = \frac{635 \cdot 10^{-9}}{2 \cdot 4 \cdot 10^{-3}} \cong 8 \cdot 10^{-5} rad,$$

we see that the requirement is fulfilled. In the theory we showed that we expect to measure signal from the bits at a medium sensor distance of $\sim 1\mu$m. The white light interferometer should therefore be able to measure the medium sensor distance in that order of magnitude. Since we determine the medium sensor distance from oscillations in the spectrum, the smallest detectable separation distance is determined by the spectral width of the halogen lamp, assuming we need one entire oscillation in the spectrum. If we use the specifications of the halogen lamp, $\lambda_{min} = 350$ nm and $\lambda_{max} = 900$, we find $d_{min} = \frac{1}{2}(\lambda_{min}^{-1} - \lambda_{max}^{-1})^{-1} = 300$ nm for the smallest detectable medium sensor distance. The maximum detectable sensor medium distance on the other hand, is determined by the coherence length, which in its turn is determined by the spectral resolution of the spectrometer ($\Delta\lambda = 1.5$ nm). If we calculate the coherence length for λ_{min} and use that as maximum measurable sensor medium distance, we find $d_{max} = \lambda_{min}^2 / \Delta\lambda = 82\ \mu$m. This brings us to the conclusion that the white light interferometer measures the sensor medium distance in the desired range.

In the mechanical MROM setup an (x,y)-nanopositioner is used to scan the medium across the sensor, with a range of 100 µm in both x and y direction, while measuring the signal of the sensor. The specified resolution of the (x,y)-nanopositioner is 0.3 nm. A second piezo is used to control and actively drive the separation distance between the medium and sensor. This piezo has a range of 38 µm and a specified resolution of 0.2 nm. Both these resolutions are more than enough for the experiment since the bits have much larger dimensions (5x1 μm). The range of the piezo elements is also sufficient for the experiment.

3.2 Sensor processing

The processing of the sensors consists of nine steps. Each step will be addressed chronologically with a description and a schematic representation of the result. The process starts with a bare silicon wafer, with a layer of 500 nm SiO_2 on top to make it insulating.

- Deposition of the MTJ stack. During the deposition of the MTJ stack a magnetic field is applied to induce crystalline anisotropy in the free layer. Underneath the MTJ stack a Cu layer is deposited, which will serve as bottom electrode.

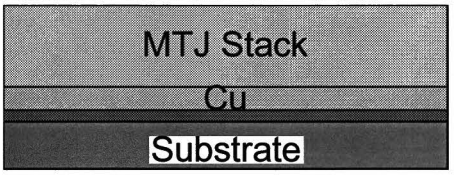

- Deposition of Cr layer. This layer will serve as a hard etch mask to structure the MTJ's. Between the Cr layer and the MTJ stack, a Ta layer is added as seed layer.

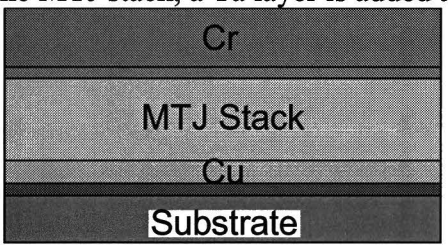

- Structuring of MTJ with e-beam lithography. The resist used is hydrogensilsesquioxane (HSQ). The structure written into the HSQ will be used as etch mask for the Cr.

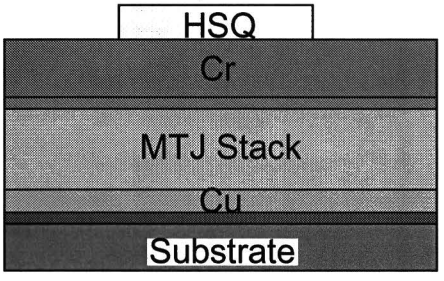

- Etching of the Cr with Reactive Ion Etching (RIE). This is chosen because it is anticipated to result in an anisotropic etch profile, and does not lead to any risk of lifting-off the whole structure, as wet etch technique might do. The Ta layer is used as stopping layer for the RIE. Any residual HSQ is removed at the end of this step.

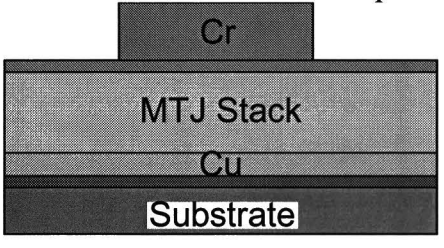

- Etching of the MTJ stack. Chosen is for Ion Beam Etching (IBE) since its clean and free of corrosion and highly anisotropic. However, any redeposition of metal atoms on the sidewall of the MTJ stack can create a shortcut of the tunnel barrier, and is therefore lethal for the MTJ. To avoid this the ion beam is directed under an off-normal angle while the wafer is rotating. The IBE is stopped at the Cu layer by measuring the electrical resistance of the remaining stack.

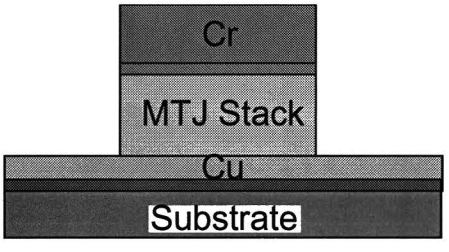

- Structuring of bottom electrodes. The bottom electrodes are defined in resist with optical contact lithography. The etching is done with a sputter etch.

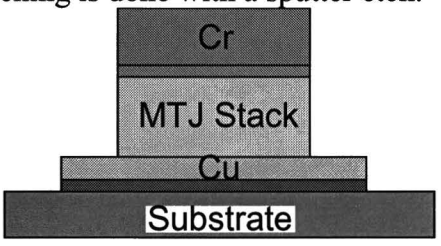

- Passivation of the stack by filling the open space between the structures with SiO_2.

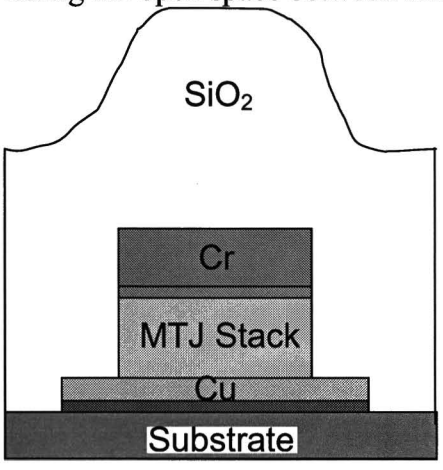

- Planarization of the wafer. The entire wafer is chemically and mechanically polished until the Cr layer is fully exposed.

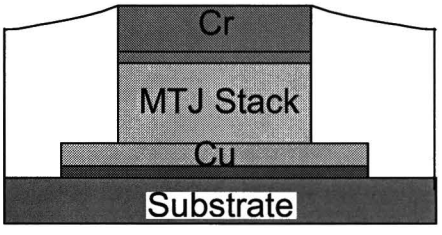

- Metallization of top contacts. A layer of Al is sputtered on top of the wafer. An image of the top electrodes is defined in resist with optical contact lithography. The layer of Al is removed by RIE everywhere, except where the resist is present, defining the top electrodes.

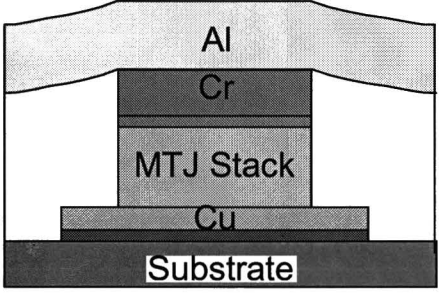

3.2.1 Sensor layout

The sensor is created in two different layouts in order to increase the yield of the process. In both layouts the dimensions of the tunnel junctions are 5 x 1 μm (length x width). The first layout is a two-dimensional array of tunnel junctions; this layout will be called MTJ array in the rest of this thesis. The MTJ array is composed of three horizontal current lines, on top of three vertical current lines, with a tunnel junction at each intersection. Because this layout is sensitive to electrostatic discharge, (a short of one tunnel barrier influences the entire array), we have created another layout in which each MTJ has a unique current path. This second layout will be referred to as single junction in the rest of the thesis. In Fig. 3.2 three pictures of the sensor are shown, the upper two are made with a microscope to illustrate the difference between the two layouts. The upper left picture is of the MTJ array, and in the upper right picture three single junctions are displayed. In the bottom an entire sensor bonded on a chip carrier is shown.

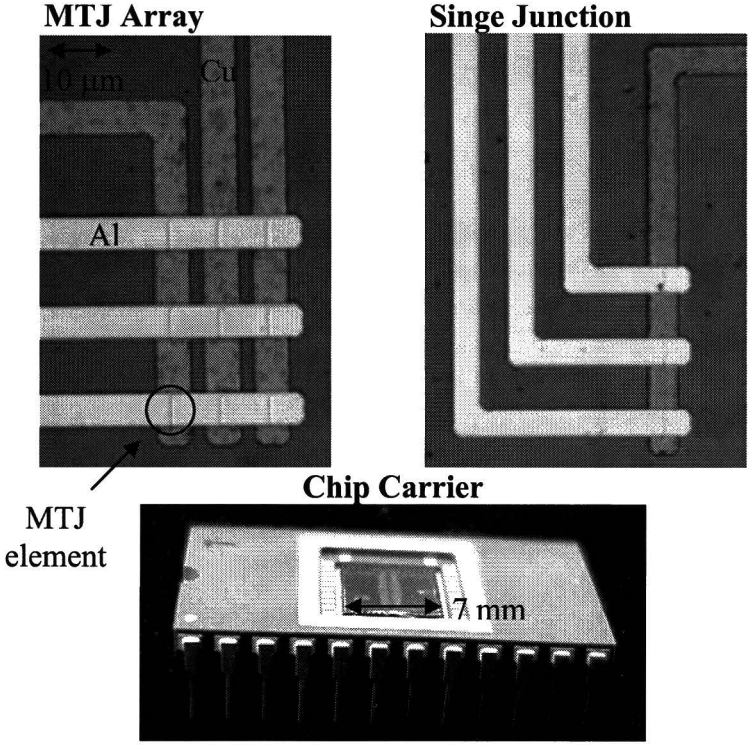

Fig. 3.2: Pictures of the sensor. The upper two pictures are made with a microscope. The upper left picture is of the MTJ array and in the upper right picture three single junctions are shown. In the bottom an entire sensor, bonded on a chip carrier, is shown, as it will be used in the experiment.

3.3 Medium processing

In comparison with the sensors, the processing of the medium is rather elementary; it basically consists of three steps. The individual bits are created in a 1 μm thick resist layer on the glass substrate. The bits have the shape of a rectangular block with dimension 5 x 1 x 1 μm (*length* x *width* x *height*). On the rectangular blocks a ferromagnetic layer is deposited. The layer has a round shape, with a radius of 0.55 mm. Please note that the bits are only present on a small portion of the total surface of the glass substrate. This is because the ferromagnetic layer makes the surface

of the medium opaque to light, which is unwanted because of the interferometer setup. As with the processing of the sensors, each step will be addressed chronologically with a description and a schematic representation of the result. The process starts with 4-inch quartz substrate of 4mm thickness.

- Structuring of bit pattern into a resist layer of 1 μm thick with e-beam lithography. A 100 nm thick HSQ layer is used as mask for the e-beam lithography. Before the resist layer is spin-coated, a Cr layer is deposited to prevent charging of the quartz plate by the e-beam. Charging at the surface would deflect the e-beam, and hence, would modify the written pattern.

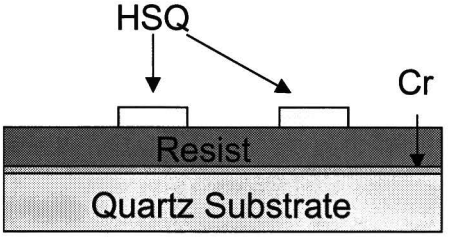

- The Cr and resist are removed by RIE, leaving Cr/resist/HSQ pillars on the quartz substrate.

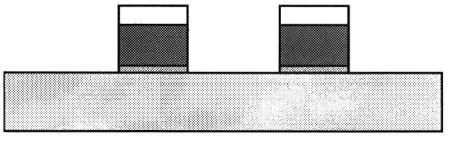

- Deposition of a 200 nm thick CoFe layer on the substrate. During deposition a magnetic field is applied along the longitudinal direction of the bits to align the crystalline anisotropy with the shape anisotropy. Between the HSQ and CoFe layer, a Ta layer is added as seed layer and the CoFe layer is passivated with a thin Al layer.

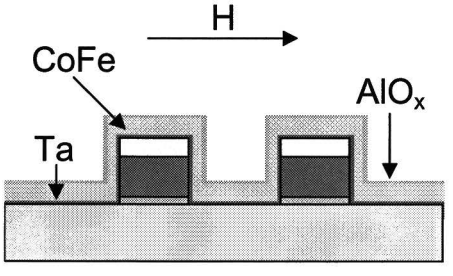

In Fig. 3.3 two SEM pictures of the bits are shown. The left SEM picture is taken before the CoFe layer is deposited. The right SEM picture is made after deposition.

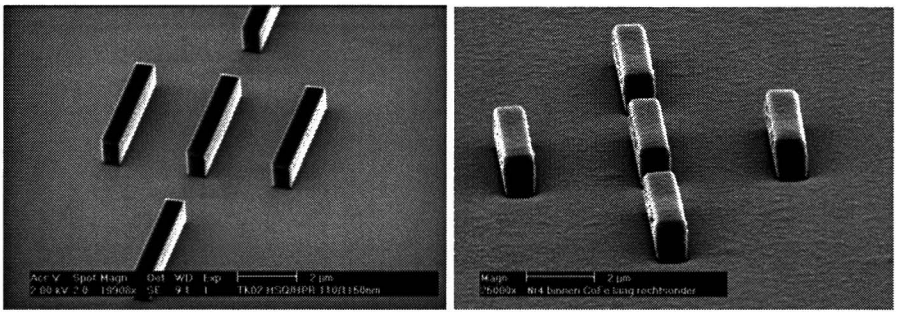

Fig. 3.3: Two SEM pictures of the medium. In the left picture the blocks of resist are shown, the CoFe layer is not yet deposited. In the right picture the CoFe is deposited, and we see the bits as they are used in the experiment.

We see that the bits are sharply defined blocks of resist, before the CoFe layer is deposited. After the deposition of the CoFe layer, the edges of the bits are less sharp. It also appears that the bits are wider at the top than at the bottom.

3.3.1 Bit patterns

The bits are structured into four different bit patterns; they are shown in Fig. 3.4. Bit pattern A is fabricated to see if we can recognize individual bits in a closely packed array. In bit pattern B the bits are grouped into triangles to see if we can recognize structures formed by bits. Bit array C resembles bit array A, however at some locations a bit is missing. This allows us to check whether we can find the position of a missing bit, in the signal of a packed bit array. The last bit pattern D, consists of groups of five bits and individual bits. This is to test whether we can detect individual bits or small groups of bits.

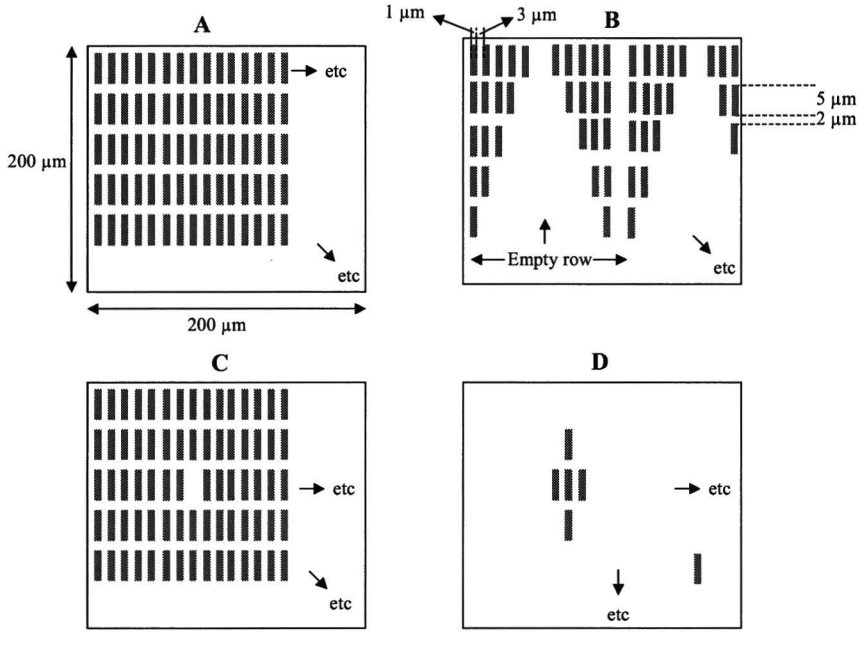

Fig. 3.4: Four different bit patterns in which the resist layer on the medium is structured. Bit pattern A is created to see if we can recognize individual bits in a closely packed array. Bit pattern B is fabricated to check if we can recognize structures formed by bits. Bit array C allows us to check, whether we can find the position of a missing bit, in the signal of a packed bit array. Bit pattern D is created to check if we can detect individual bits or small groups of bits.

3.4 Calibration setup

Because the difference in layout between the MTJ array and the single junction, both require a different setup for measuring their electrical resistance. We will first discuss the calibration setup for the MTJ array; it is drawn schematically in Fig. 3.5. In order to create a homogeny magnetic field at the MTJ array, two Helmholtz coils are used. The current through the Helmholtz coils is controlled by a current source, which in its turn, is controlled by a function generator. By linking the function generator to a PC we can control the current, and thus the magnetic field, with the PC. Not shown schematically in Fig. 3.5 is a Hall probe used to measure the magnetic field produced by the two Helmholtz coils. The read out of the Hall probe is also done with the PC.

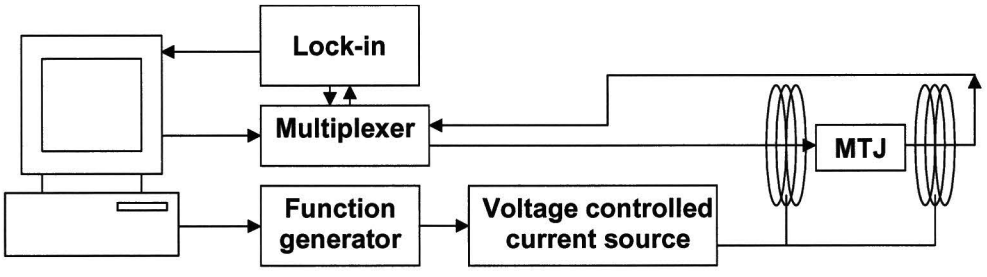

Fig. 3.5: Schematic picture of sensor calibration setup used for the MTJ array. The multiplexer selects which MTJ element of the MTJ array is measured. In Fig. 3.6 a schematic picture of the multiplexer is drawn.

The electrical resistance of an element in the MTJ array is measured with a lock-in amplifier, which is linked to the PC. The multiplexer determines which element of the MTJ array is measured. It consists of six low ohmic (30 Ω) Field Effect Transistors (FET) and a virtual ground. In Fig. 3.6 the principle behind the multiplexer is drawn schematically.

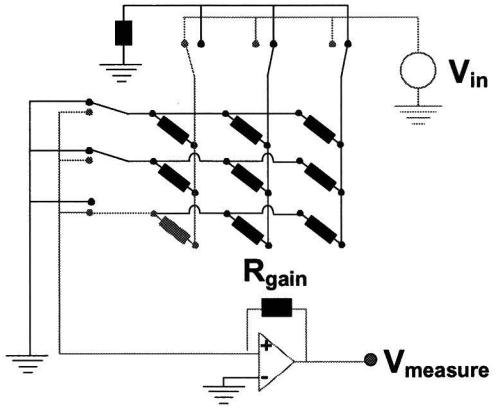

Fig. 3.6: Schematic picture of the manner in which the multiplexer measures the electrical resistance of one MTJ element of the MTJ array.

The multiplexer applies a voltage, V_{in}, on a column and the other remaining columns are placed on earth via a shunt resistance. The shunt resistance prevents current leakage when a MTJ element is shorted. The rows are also placed on earth, however, one of them is placed on earth via an op-amp. This allows us to do determine the resistance, R, of the red element in Fig. 3.6 via,

$$R = -R_{\text{gain}} \frac{V_{\text{in}}}{V_{\text{measure}}}, \tag{3.1}$$

in which V_{measure} and R_{gain} are depicted in Fig. 3.6. The six FET's of the multiplexer are controlled through the PC.

For the single junction the multiplexer is not necessary, and the calibration setup is a bit different. For this case the setup is drawn schematically in Fig. 3.7.

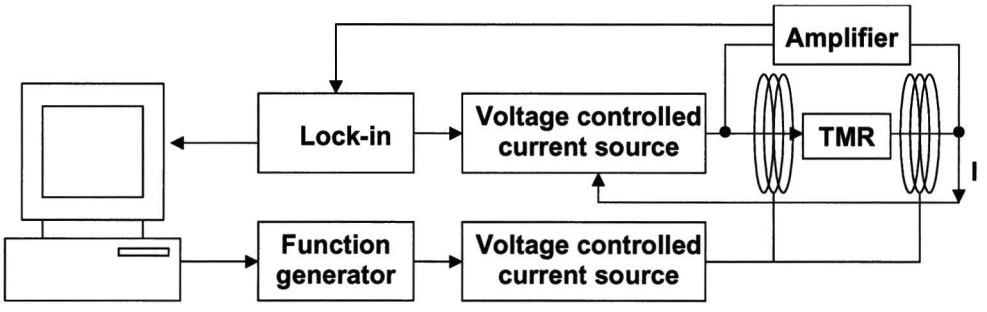

Fig. 3.7: Schematic picture of calibration setup used for the single junction.

The part controlling the current through the Helmholtz coils, and for measuring the magnetic field is the same, however, the manner in which the electrical resistance of the MTJ is determined, is different. In this case the output signal of the lock-in is used to create an oscillating current with constant amplitude through the MTJ. The voltage difference over the MTJ is amplified and linked to the lock-in amplifier. Once again the PC is used to readout the lock-in amplifier.

3.5 MROM setup

The MROM setup is the mechanical part necessary for aligning the medium and sensor parallel and manipulating them on a nanometer resolution. In Fig. 3.8 and Fig. 3.9 pictures of the setup are shown. The millimeter screws denoted with number 1, in the top picture of Fig. 3.8, can be used to control the tilt of the plateau on which the (*x*-*y*) nanopositioner and medium will be attached. The positioning of the chip holder, in which the chip carrier with sensor is placed, is done with the screws denoted with number 2. The piezo element, labeled with number 3, is used to vary the distance between the sensor and medium. The lower left picture of Fig. 3.8 shows the MROM setup when the (*x*-*y*) nanopositioner is attached, and in the lower right picture the medium holder is attached to the (*x*-*y*) nanopositioner. The backside of the medium holder, on which the medium is attached, is shown in Fig. 3.9. The medium is kept in its place by applying vacuum to it. Note that there is an opening in the medium holder; this is the optical window necessary for the interferometers. An E-516 control module of PI is used to control the piezo elements. This control module is linked to the PC through the RS-232 interface.

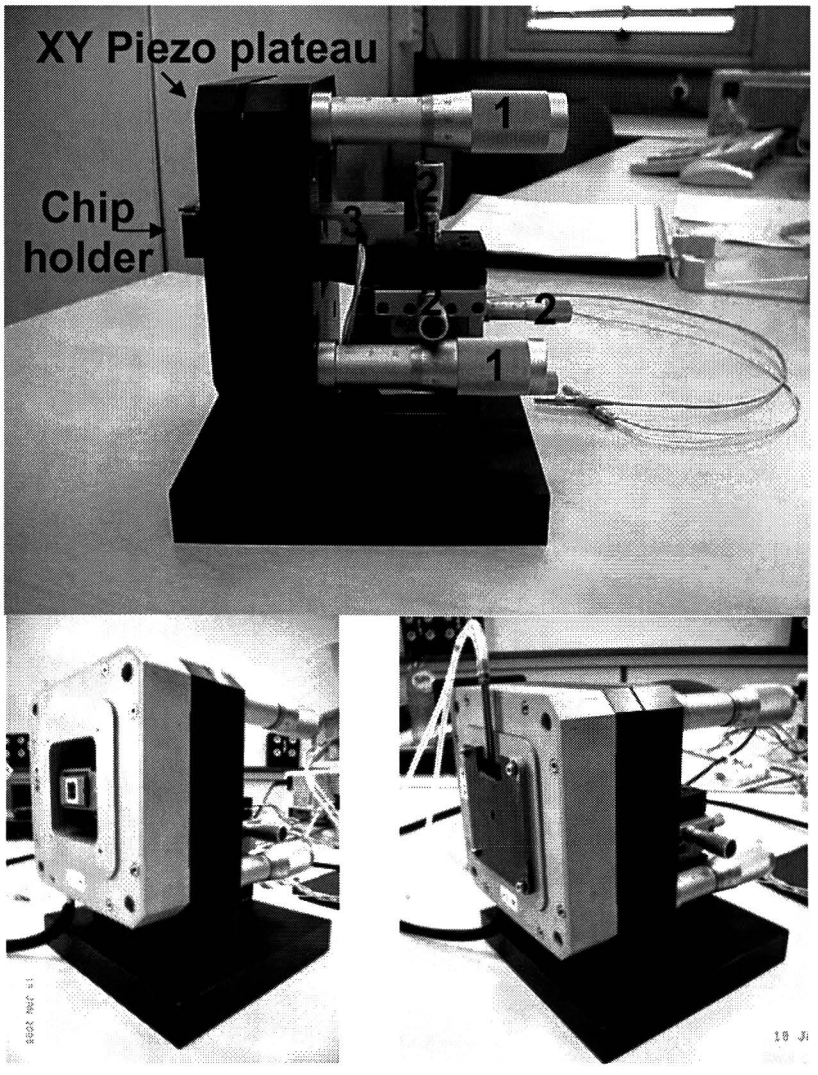

Fig. 3.8: Three pictures of the mechanical MROM setup. In the upper picture the MROM setup without (x-y) nanopositioner is shown. In the lower left picture the (x-y) nanopositioner is attached and in the lower right picture the (x-y) nanopositioner and medium holder are attached to the MROM setup.

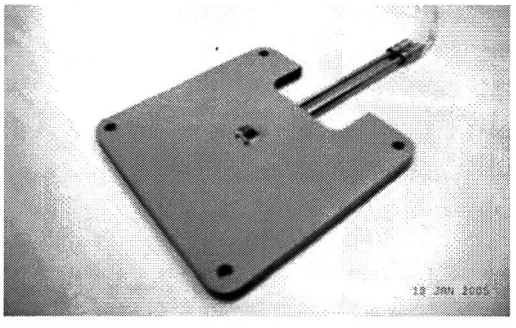

Fig. 3.9: Picture of medium holder with medium attached. The medium is kept in its positions by applying vacuum to it.

3.6 Interferometer

The last part of the chapter experiment is about the interferometers. It begins with the monochromatic interferometer and then addresses the white light interferometer.

3.6.1 Monochromatic interferometer

In Fig. 3.10 a schematic picture is drawn of the home built Fizeau interferometer.

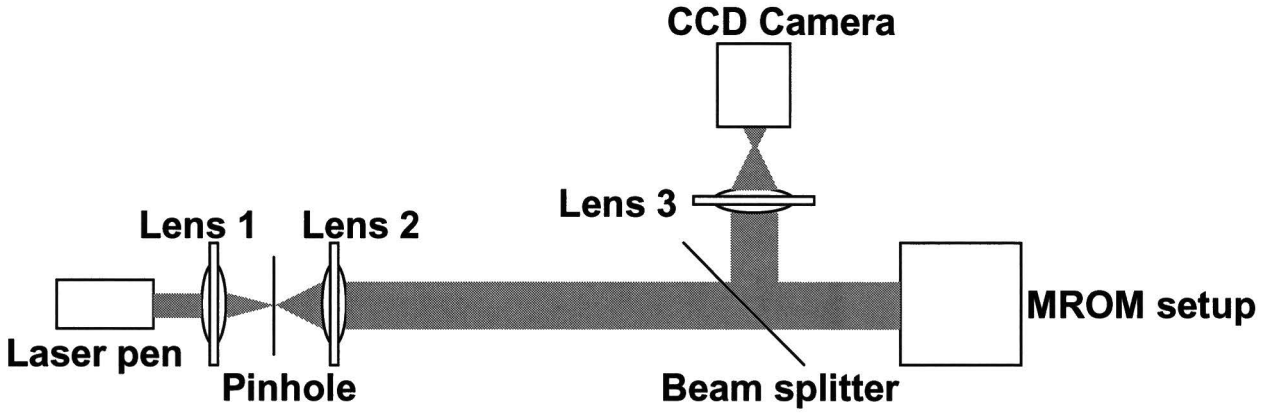

Fig. 3.10: Schematic overview of the Fizeau interferometer. The laser pen is a N-type diode laser. The pinhole, in combination with lens 1 and 2, act as collimator. The beam splitter reflects the light coming from the MROM setup in the direction of the CCD camera. Lens 3 forms an image of the optical window of the MROM on the CCD camera.

The laser pen is a N-type diode laser with a wavelength of 635 nm with an optical power of 0.7 mW. The pinhole and the first two lenses act as a collimator. The beam splitter reflects part of the light coming from the MROM setup into lens 3, which creates an image of the MROM setup on the CCD camera. In the following the important components of the optical setup will be described in more detail.

The laser pen

In Fig. 3.11 a more detailed picture is drawn of what is meant with the block "laser pen" in Fig. 3.10.

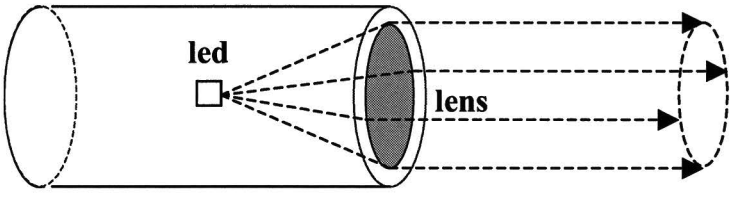

Fig. 3.11: Schematic picture of the laser pen. The laser pen consists of a LED and a lens, which also forms the exit pupil. Placing the LED in the focal plane of the lens collimates the emitted light.

The laser pen is chosen as light source since it is easy to implement and it emits enough power. The light emitted by the light emitting diode (LED) is collimated through the lens at the exit of the laser pen. The LED is placed in the focal plane of the lens, and the numerical aperture (NA) of the lens is the same as the full width half maximum (FWHM)[21] of the led. The laser pen used in the experimental setup emits a light bundle with a diameter of 4 mm and an optical power of 0.7 mW at 100 mm from the pen. The divergence of the beam leaving the laser pen is 0.25 mrad.

Collimator

In Fig. 3.12 a schematic picture is drawn of the collimator. The light bundle leaving the laser pen is collimated, however the intensity is not homogeneous enough for our purpose. This is because the exit lens of the laser pen acts as a round aperture, creating diffraction in the form of Airy rings [1]. In order to remove the diffraction pattern the light is focused on a pinhole with a lens (lens 1). This pinhole will create an Airy diffraction pattern just like the exit lens of the laser pen. However, by placing lens 2 on focus distance, and choosing the diameter of lens 2 equal to the diameter of the first dark Airy ring, a collimated bundle is created. This bundle suffers much less from diffraction because the intensity at the edges of lens 2, and thus the aperture, is zero. By choosing the diameter of the second lens a few times larger than the optical window of the MROM setup we have created an intensity distribution that is homogeneous enough for our purpose.

We have calculate the diameter of the first dark Airy ring originating from the pinhole with,

$$r_{dark} = 1.22 \cdot \frac{D\lambda}{2a}, \tag{3.2}$$

where r_{dark} is the radius of the first dark ring, a is the radius of the opening in the pinhole and λ is the wavelength of the light (see reference [1] on page 416). The distance at which we want to calculate the diameter of the first dark airy ring is D. When we fill in the appropriate numbers, $D = f_2 = 150$ mm and $a = 10$ μm, we find that $r_{\mathrm{dark}} = 1.16$ cm. The diameter of lens 2 must therefore be $2 \cdot r_{\mathrm{dark}} = 2.32$ cm. Lens 1 is chosen to have a focus length of 100 mm.

[21] The intensity of the emitted light by the LED depends on the angle and the FWHM is defined as the angle at which the intensity of the light is half the maximum intensity.

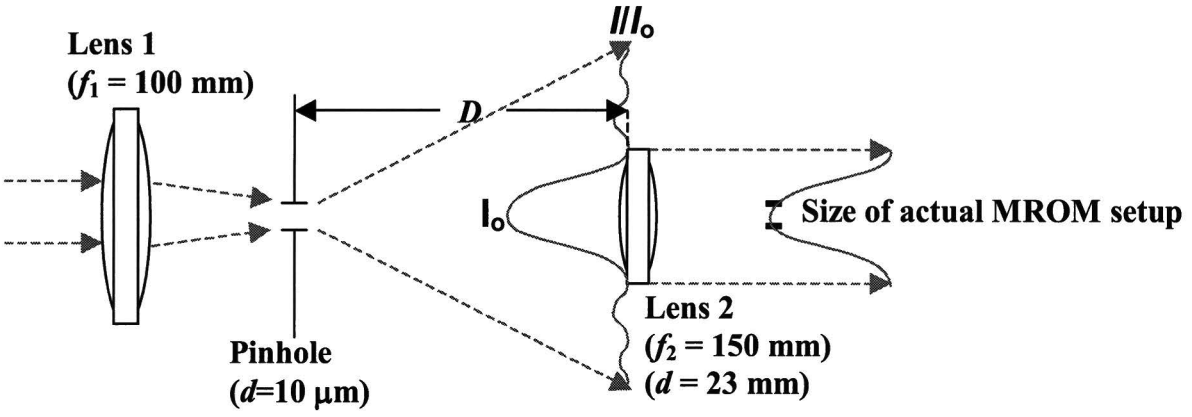

Fig. 3.12: Schematic representation of the collimator. Lens 1 focuses the light on the pinhole. The pinhole creates a diffraction pattern in the form of Airy rings. The diameter and position of lens 2 are chosen in such a manner, that only the first Airy ring of the diffraction pattern is collimated. This way a homogenous intensity is created over the optical window of the MROM setup.

Projection lens

Lens 3 creates an image of the optical window of the MROM setup on the CCD camera. The image must be approximately of the same size as the optical window, as it will fit nicely to the active area (~1 cm^2) of the CCD chip. This means that the image distance should equal the object distance. Substituting this into the lens formula gives:

$$\frac{1}{f} = \frac{1}{o} + \frac{1}{i} = \frac{2}{o} = \frac{2}{i}, \tag{3.3}$$

where f is the focal length, o the object distance and i the image distance. Rewriting equation (3.3) gives $o = i = 2f$. Since f_3 = 100 mm the object and image distance must be around, $o = i$ = 200 mm.

Optical alignment

In this paragraph the optical alignment used for the Fizeau meter is described. The reader can, without any loss of continuity, skip this section. It is mainly intended as guideline for setting up the optical experiment. The entire setup is built on an optical table.

- The laser pen is placed at the optical rail at the same height (12.4 cm from the optical table) as the optical window of the MROM setup, with the silicon sensor attached in it. Between the laser pen and the MROM setup an aperture, with an opening of approximately 1 cm, is placed at the optical rail at the same height. The laser pen is manipulated in such way that

the light bundle is going through the aperture in both directions[22]. When this is done the aperture is removed.

- Lens 1 is placed at the optical rail at such a distance that it magnifies the diffraction pattern coming from the laser pen. Lens 1 is then manipulated until the middle of the Airy disk is located at the optical window of the MROM setup. The pinhole is then placed in the focal length of lens 1. This is done by first placing the pinhole at a distance greater than the focal length. This way the light spot is larger and the location of the pinhole is found easier. After the pinhole is aligned properly in the plane perpendicular on the optical axis, the pinhole is carefully shifted backwards until it is at the focal length of lens 1. The pinhole is in focus when the intensity behind the pinhole is at its maximum. Now lens 2 is placed behind the pinhole. The lens is placed in such a way that the bundle doesn't diverge or converge after lens 2. This means that the pinhole is at the focal distance.
- The beam splitter is placed on the optical table at approximately the focal length of lens 3. Lens 3 is then placed on a second optical axis, directed orthogonal to the first optical axis formed by the laser and the MROM setup. Lens 3 is positioned at approximately a distance f_3 away from the first optical axis. This ensures that the object length is approximately equal to the image length, which means that the magnification is approximately one. The CCD camera is then placed a distance of approximately 2 times f_3. Looking at the output of the CCD camera one can verify if the CCD camera is at the correct distance from lens 3. If it is, the image of the structures on the silicon can be viewed clearly. The last step is to attach the medium to the MROM setup. The tilt between the silicon and the medium can now be observed by looking at the intensity output of the CCD camera.

3.6.2 White light interferometer

In Fig. 3.13 the white light interferometer is drawn schematically. The light source is a Fiber-Lite 30 W quartz halogen lamp. It emits light with wavelengths between 350 nm and 900 nm. The fiber coming from the light source is placed directly behind a pinhole with a diameter of 0.2 mm. The light passing through the pinhole is collimated through lens 1 (diameter is 1 cm and a $f_1^{\text{white}} = 3$ cm). If we calculate the coherence length of the entire spectrum emitted by the light source ($\lambda = 600$ nm, $\Delta\lambda = 300$ nm, see equation (2.63)), we obtain $\Lambda \cong 1\ \mu$m. Therefore there is no reason to adjust the diameter of lens 1 to the first dark Airy ring, there is no diffraction pattern visible. The pinhole is placed in the setup to create a point source. All the lenses used in the white light interferometer are achromatic lenses. This is to reduce chromatic aberrations[23]. The aperture, which has a diameter of 50 mm, is placed in the optical path to reduce aberrations by removing the rays not near the optical axis. The reason for reducing the aberrations is that the optical spot on the MROM setup must be small. Otherwise the distance between the medium and sensor is not well defined, since it is an average over the entire optical spot. Two beam splitters are used; one is used to reflect the light coming from the MROM setup towards the spectrometer. The other is used to reflect it towards a CCD camera. The image on the CCD camera is formed by lens 2 ($f_2^{\text{white}} = 3$

[22] One direction is when the light is coming from the laser pen. The other direction is when the light is reflected at the MROM setup.

[23] Chromatic aberrations come from the fact that the refractive index is a function of the wavelength. Thus the focus point of a lens for each wavelength is different. Achromatic lenses are specially designed to make this effect smaller then in a normal lens. For more information about chromatic, and other aberrations, see [1] at pag. 220.

cm, diameter is 1 cm), and allows us to observe the medium and sensor during the experiment, and to see where we focus the spot. Besides that, focuses lens 2 the light on the MROM setup. The light traveling towards the spectrometer is focused through lens 3 (f_3^{white} = 10 cm, diameter is 5 cm) on the fiber (diameter is 0.2 mm) of the spectrometer. The spectrometer is connected with a computer for the purpose of signal processing. The spectrometer is an Ocean Optics USB2000. According to the specification of Ocean Optics it has a resolution of 1.5 nm (FWHM) and operates in a range between 390 nm and 950 nm.

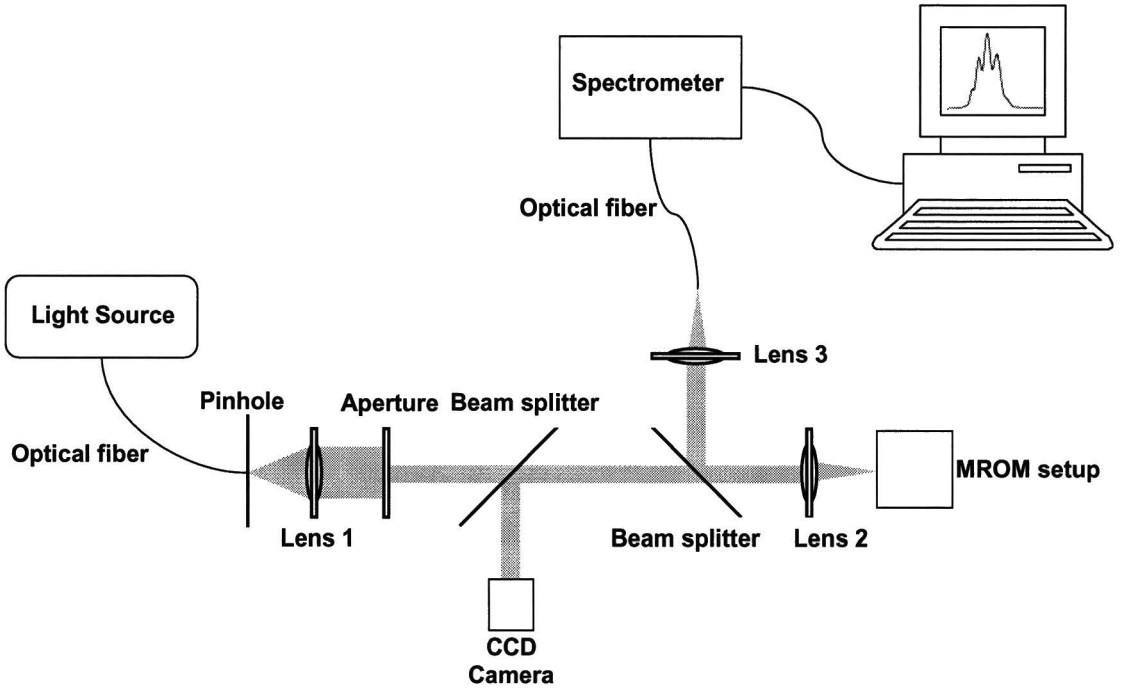

Fig. 3.13: Schematic representation of the white light interferometer. The fiber coming from the light source is placed directly behind a pinhole, which is placed in the focal plane of lens 1. All lenses drawn in Fig. 3.13 are achromatic. In order to reduce aberrations, the size of the light beam is truncated, by placing an aperture in the optical path. The first beam splitter is used to create an image of the optical window of the MROM setup on the CCD camera. The second beam splitter is used to reflect the light coming from the MROM setup, towards the spectrometer. Lens 2 focuses the light on the medium and sensor, and it creates an image of the sensor and medium on the CCD camera. Lens 3 focuses the light on the fiber of the spectrometer. The spectrometer gives it output to the computer through the USB interface. The computer is used to do the necessary signal processing in order to determine the separation distance between the medium and sensor.

Data processing

The raw data, coming from the spectrometer to the computer via the USB interface, is processed with a program written in Labview 7.0. The raw data represents intensity versus wavelength. The intensity is measured in counts per time interval. The time interval the spectrometer measures can be adjusted. The maximum integration time is 100 ms. How one count relates to intensity in watt can be calculated with the specifications of the spectrometer. However, this is not necessary because the Labview program normalizes the measured spectrum.

When the program starts it first measures the stray field $S[\lambda]$. This is done by blocking the light source and saving the resulting spectrum in memory. A typical stray field measurement is shown in Fig. 3.14.

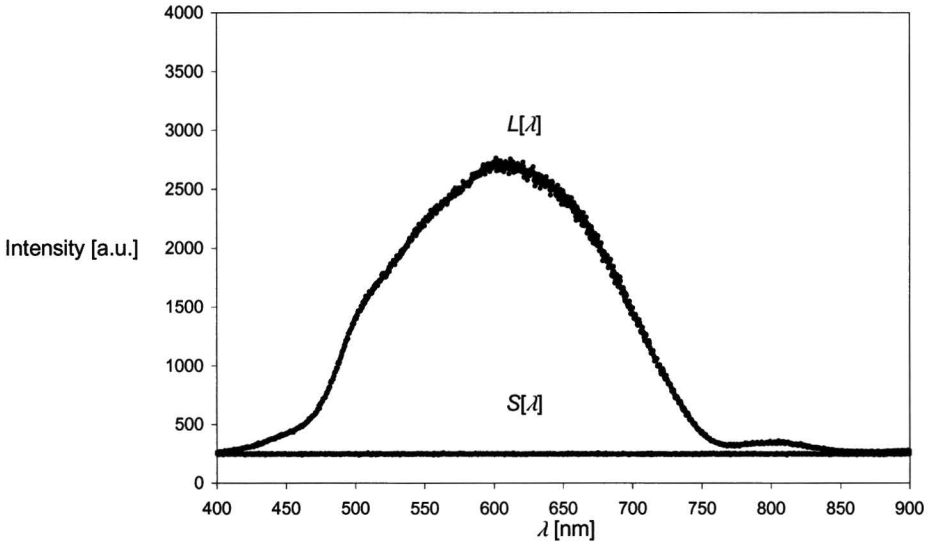

Fig. 3.14: Measurement of stray field, $S[\lambda]$, and light source spectrum, $L[\lambda]$. The stray field has been taking by blocking the light source and measuring the spectrum. The light source spectrum is taken after the light traveled through the optical and MROM setup. In order to prevent the spectrum from oscillating, the separation distance between the medium and sensor is made larger than the coherence length.

The next step is to measure the spectrum of the light source in combination with the optical and MROM setup ($L[\lambda]$). In order to prevent the spectrum from oscillating, the distance between medium and silicon is made larger than the coherence length. Because the light is traveled through the entire optical and MROM setup, all relevant spectral coefficients are taken into account. A typical measurement of $L[\lambda]$ is shown in Fig. 3.14. The shape of the spectrum is mainly determined by the halogen lamp and does indeed contain wavelengths between 350 nm and 900 nm. The measurement of $L[\lambda]$ is done once at the beginning of the program and then stored in the memory. With the stray spectrum ($S[\lambda]$) and the light source spectrum ($L[\lambda]$) known, the actual distance between the medium and the sensor can be determined. In order to do this, the distance between the medium and sensor is made smaller than the coherence length and the spectrum is measured. The spectrum with oscillations will be called $O[\lambda]$. Fig. 3.15 shows a measurement of $O[\lambda]$, taken with the medium and a piece of unprocessed silicon. The separation distance between them is 30.8 μm.

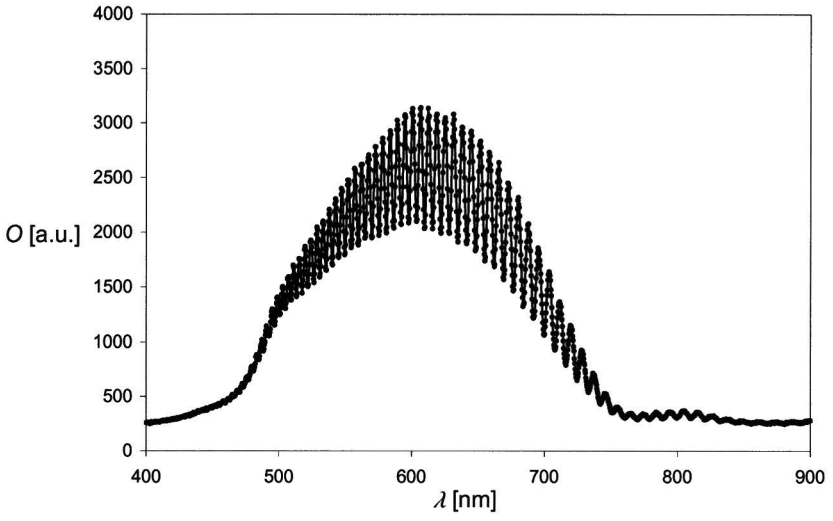

Fig. 3.15: Spectrum with oscillations ($O[\lambda]$). The period of the oscillations corresponds to a distance of 30.8 μm between medium and silicon.

In order to normalize the intensity, the stray field ($S[\lambda]$) is subtracted from the spectrometer signal ($O[\lambda]$) and divided by the light source spectrum ($L[\lambda]$), which is also corrected with the stray field

$$I[\lambda]_{\text{normalized}} = \frac{O[\lambda] - S[\lambda]}{L[\lambda] - S[\lambda]}. \tag{3.4}$$

In Fig. 3.16 the normalized intensity, calculated with the spectra of Fig. 3.14 and Fig. 3.15, is shown. Up to this point the intensity is measured versus the wavelength. To get a spectrum with a constant oscillation the unit of wavelength, read from the spectrometer, is changed to wave number using

$$k = \frac{2\pi}{\lambda}. \tag{3.5}$$

If equation (3.5) is applied to the spectrum shown in Fig. 3.16, the spectrum shown in Fig. 3.17 is obtained.

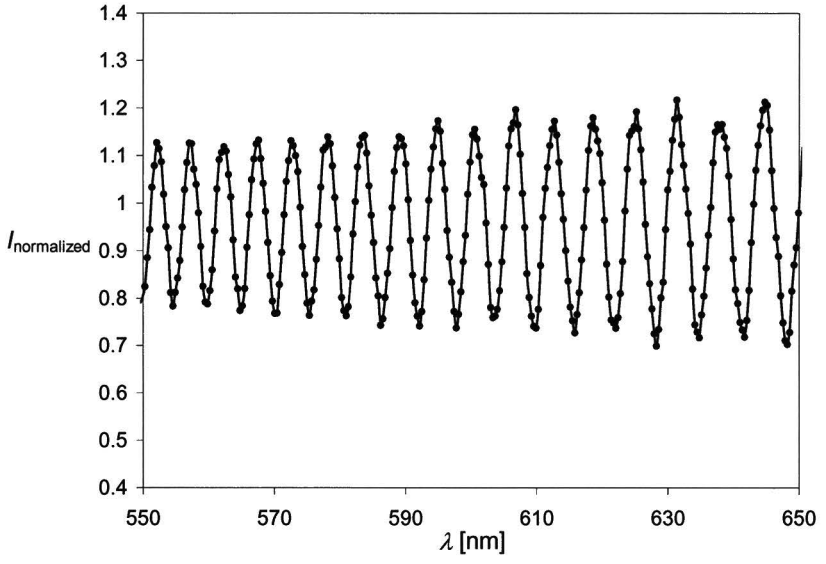

Fig. 3.16: Normalized intensity versus wavelength. The period of the oscillations corresponds to a distance of 30.8 μm between medium and silicon.

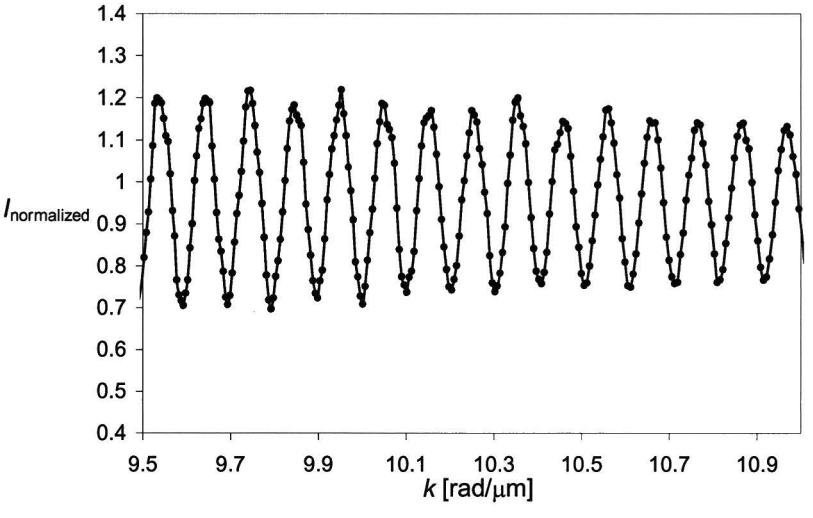

Fig. 3.17: Normalized intensity versus wave number. The period of the oscillations corresponds to a distance of 30.8 μm between medium and silicon.

The last step is to determine the period of the oscillation. This is done by finding the peak values of k and plotting them versus an integer. The slope of this plot is equal to $-\pi/d$. To find the peak values of k a standard routine of Labview 7.0, called Peak Detector, is used. The routine fits a quadratic polynomial to sequential groups of data points. If a maximum is present in the fitted polynomial the routine recognizes this as a peak. The peak values are linearly fitted versus an integer number. The outcome of this procedure on the spectrum in Fig. 3.17, is shown in Fig. 3.18. The last step is to calculate the separation distance from the slope of the fit. The error in the distance measurement will be discussed in the experimental results.

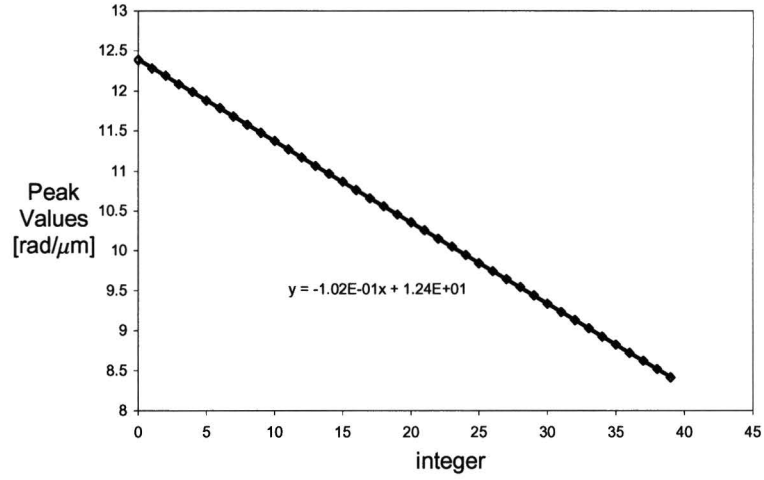

Fig. 3.18: Peak values of k versus an integer number. The corresponding distant is $\pi/0.102 = 30.8\ \mu$m.

4 Experimental Results

This chapter deals with the experimental results, which are mainly the detection of magnetic bits. However, before we show and discuss them we will first address the experiments necessary for the interpretation. The first subject is the calibration of the magnetoresistance of the single junction and the MTJ array. Then we will discuss the performance of the monochromatic and white light interferometer. Both are tested with an unprocessed piece of silicon and the medium. The white light interferometer is also tested with the MTJ array and the medium in order to measure the influence of the SiO_2 layer on the detected spectrum. This will be compared with the theory and we will find the uncertainly in the measured separation distance.

4.1 Sensor calibration

The calibration of the sensor is done with the external magnetic field perpendicular on the longitudinal direction of the MTJ element; this corresponds with the configuration drawn in Fig. 2.20. In all cases the external magnetic field, H, starts at $-H_{max}$ and is swept to $+H_{max}$ and back. First the external magnetic field is varied over such a range, H_{max} = 300 Oe, that the magnetoresistance is swept from R_{ap} to R_p and back. Then a smaller range is chosen, H_{max} = 25 Oe, corresponding with the expected magnetic fields of the bits. In Fig. 4.1 and Fig. 4.2 both measurements of the single junction are shown.

As can been seen in Fig. 4.1, the magnetoresistance varies almost linearly from R_{ap} to R_p and vice versa. We observe a small hysteresis in the magnetoresistance curve. This hysteresis will not affect the bit detection, because the magnetic bit field it is too small to saturate the free layer of the MTJ element, and the sensitivities of the two curves are the same. Furthermore we note that the curve is shifted to positive external magnetic fields with 49 Oe. This indicates that the MTJ stack influences the free layer, as is discussed in section 2.4.2 of the theory. This is also no problem, because the sensor is still in its linear regime at $H = 0$ Oe. The ΔR of the single junction is 1.3 kΩ, this is in the expected order of magnitude and suitable for bit detection.

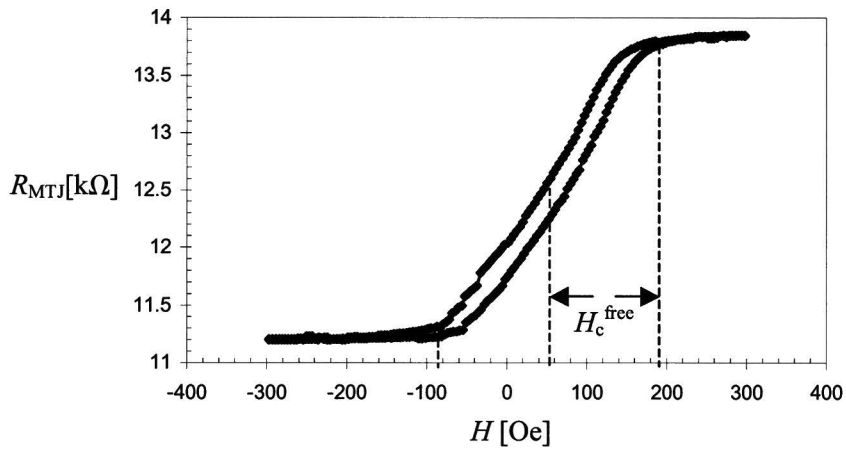

Fig. 4.1: Calibration of single junction, the magnetoresistance is swept from R_p to R_{ap} and back. The following settings are used to measure the resistance, the amplitude of the current through the single junction is 10 μA and the lock-in settings are, 10 ms integration time, 12 dB attenuation factor and a frequency of 900 Hz.

In Fig. 4.2 we see the magnetoresistance curve for the smaller sweep of the external magnetic field. The curve is linear, but the resistance of the single junction shows a jump at $H = 7$ Oe. A linear fit of the curve is made and also shown in Fig. 4.2. From this fit we determine that the sensitivity of the single junction is 8.2 ΩOe^{-1}. This also is in the same order of magnitude as predicted in the theory, see section 2.4.3, and therefore suitable for bit detection.

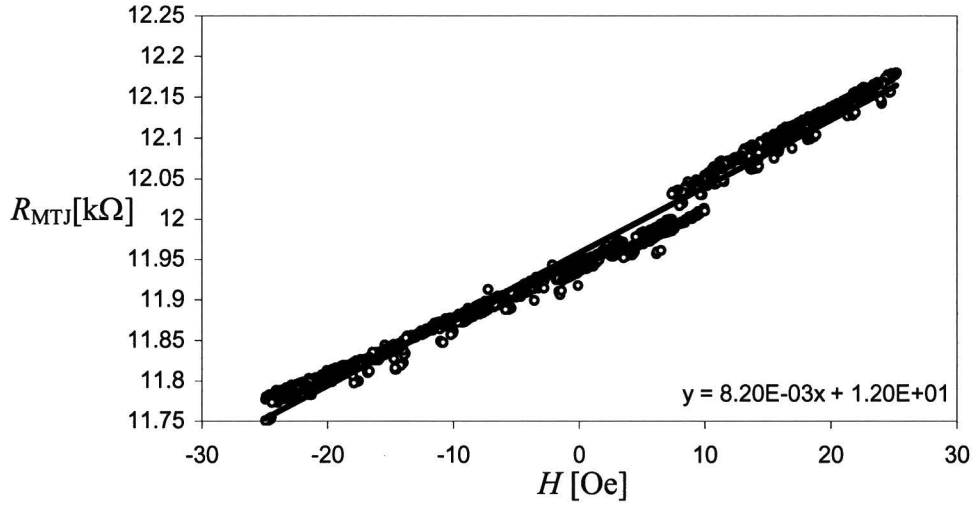

Fig. 4.2: Calibration of single junction, the magnetoresistance is swept in a small range to determine the sensitivity. In the lower right corner the equation of a linear fit is shown. The following settings are used to measure the resistance, the amplitude of the current through the single junction is 10 μA and the lock-in settings are, 10 ms integration time, 12 dB attenuation factor and a frequency of 900 Hz.

We can compare the measured H_c^{free} with the theory, discussed in section 2.2.2, from which we expect a value of $H_c^{free} = (N_1\text{-}N_2)M_{free} = 135$ Oe. This is calculated for a rectangular ferromagnet with dimensions (l x w x h) 5 μm x 1 μm x 0.015 μm, and $4\pi M_{free} = 15 \cdot 10^3$ G. From Fig. 4.1 we can determine that the measured H_c^{free} is 142 Oe. Because the theoretical and measured H_c^{free} are in the same order of magnitude, we can conclude that the magnetization rotation of the MTJ element behaves according to a single magnetic domain.

The MTJ array of 3x3 sensors, see section 3.2.1, is also measured for two different values of H_{max}, being $H_{max} = 300$ Oe and $H_{max} = 25$ Oe. We will not show all the figures; instead we will list the sensitivities and R_0 values in Table 4.1.

		Column					
		0		1		2	
Row	0	6.5 ΩOe^{-1}	8.5 kΩ	5.6 ΩOe^{-1}	6.9 kΩ	6.9 ΩOe^{-1}	8.0 kΩ
	1	5.8 ΩOe^{-1}	7.3 kΩ	6.4 ΩOe^{-1}	7.2 kΩ	5.6 ΩOe^{-1}	7.6 kΩ
	2	7.1 ΩOe^{-1}	7.8 kΩ	5.5 ΩOe^{-1}	7.1 kΩ	7.9 ΩOe^{-1}	8.2 kΩ

Table 4.1: Measured values of sensitivity and R_0 of the elements of the MTJ array. They are measured with the following lock-in and multiplexer settings; 10 ms integration time, 12 dB attenuation factor, frequency of 900 Hz and $V_{in} = 100$ mV. The multiplexer is set at $R_{gain} = 10$ kΩ.

We see that each element can be read out individually and that the sensitivities are in the same order of magnitude as the single junction. All the elements of the MTJ array are therefore suitable for bit detection. However, after the values in Table 4.1 were measured the tunnel barrier of one of the elements was shorted due to ESD and the resistance of that element dropped to ~ 500 Ω. The MTJ array was measured again with the same settings. The measured values are listed in Table 4.2.

		Column					
		0		1		2	
Row	0	5.9 ΩOe^{-1}	7.4 kΩ	5.2 ΩOe^{-1}	6.2 kΩ	short	short
	1	5.8 ΩOe^{-1}	7.4 kΩ	6.4 ΩOe^{-1}	7.2 kΩ	5.8 ΩOe^{-1}	7.7 kΩ
	2	7.2 ΩOe^{-1}	7.9 kΩ	5.6 ΩOe^{-1}	7.2 kΩ	8.0 ΩOe^{-1}	8.3 kΩ

Table 4.2: Measured values of sensitivity and R_0 of the elements of the MTJ array after one of the elements is shorted due to ESD. They are measured with the following lock-in and multiplexer settings; 10 ms integration time, 12 dB attenuation factor, frequency of 900 Hz and V_{in} = 100 mV. The multiplexer is set at R_{gain} = 10 kΩ.

If we compare the values before and after the ESD, we see that the short of one of its elements affects the first row of the MTJ significantly. Both the sensitivity and R_0 of the two remaining elements in the row have decreased significantly. The sensitivity and R_0 of the other elements have not increased significantly. This is because V_{in} is applied on a row of the MTJ array, see Fig. 3.6 in paragraph 3.4. Because most of the current will flow through the shorted MTJ, we will measure a lower resistance and sensitivity for the remaining two MTJ elements. This brings us to the conclusion that the state of one element in row, influences the read out of the other elements in the row. However, if one element in a row is shorted, the other two elements in the row can still be used as sensor.

The measured H_c^{free} of the MTJ array elements are listed in Table 4.3. As we can see the H_c^{free} of the elements of the MTJ array are a bit higher than that of the single junction, but still in the same order of magnitude. This is because the MTJ array is processed on a different wafer. The H_c^{free} of the elements of the MTJ array are in the same order magnitude as the H_c^{free} predicted by the theory. This brings us to the conclusion that the MTJ elements also have one magnetic domain.

		Column		
		0	1	2
Row	0	160 Oe	149 Oe	165 Oe
	1	155 Oe	157 Oe	162 Oe
	2	159 Oe	166 Oe	150 Oe

Table 4.3: Measured values of H_c^{free} of the MTJ array.

To conclude, both the single junction and the MTJ array elements show magnetoresistance. The magnetoresistance curve shows hysteresis and it appears that the free layer is still influenced by the MTJ stack. However, both issues are not important for bit detection because the curve is linear around zero fields. Furthermore we can conclude, from the measured H_c^{free}, that the free layer of the MTJ element behaves as a single magnetic domain. In the case of the MTJ array, we have found that the state of one element influences the read out of the other elements in the row.

However, if one of the elements in a row is shorted, the other two elements can still be used as sensor.

4.2 Interferometer

Both the monochromatic and white light interferometer are tested with a piece of unprocessed silicon and the medium. The silicon has a surface of 1x2 cm^2, and the medium has a surface of 6x4 mm^2. To determine whether the white light interferometer measures the correct separation distance, it is varied with the piezo while measuring it. This test is also used to determine the minimal obtainable distance between the medium and silicon. The last part of this paragraph deals with the influence of the SiO_2 layer, in which the MTJ elements are embedded, on the detected spectrum.

4.2.1 Tilt between sensor and medium

In Fig. 4.3 three screenshots of the CCD camera of the monochromatic interferometer setup are shown. They are made with the medium and a piece of unprocessed silicon. Each screenshot is taken with a different tilt between the medium and silicon. Going from left to right, the tilt was decreased until no fringes were observed (the right picture).

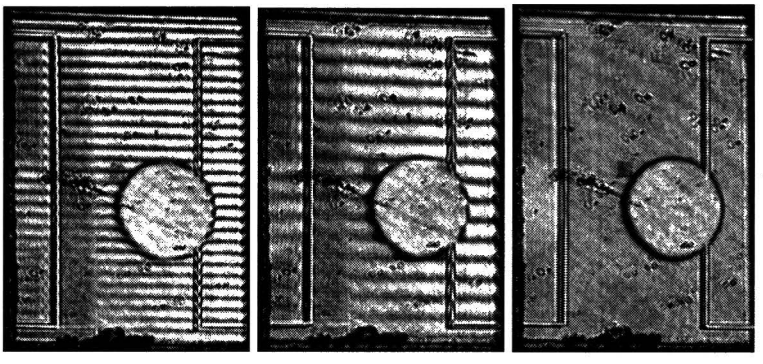

Fig. 4.3: Three screenshots of the CCD camera output. The fringes correspond with a tilt between the medium and silicon. Going from left to right the tilt is decreased. In the rightmost picture no fringes are visible, this indicates that we have reached the minimal tilt.

The non-horizontal fringes that are still visible in the right picture are due to the optical setup. In conclusion, we are able to get an indication of the tilt, and more important, we can reduce the tilt to the minimum value of $8 \cdot 10^{-5}$ rad. This corresponds with the minimal value calculated in paragraph 3.1.

4.2.2 Minimal distance between unprocessed silicon and medium

With the medium and silicon aligned parallel we can test the white light interferometer and try to determine the minimal obtainable separation distance. This is interesting because it is expected to be an important design constraint in a real application. The medium and silicon are carefully

cleaned in an ultrasonic acetone bath of 12 minutes. The silicon medium distance is varied with the piezo, while measuring it with the white light interferometer. The measurement is shown in Fig. 4.4; we see that the measured medium silicon distance varies linear with the piezo position, with a slope of 1.02, until the separation distance is approximately 1.2 μm. The error in the slope is due to the determination of the peak positions, by the Labview program. Around 1.2 μm the medium and silicon make contact and the distance only decreases slightly with increasing piezo position. At the end of the piezo range the medium silicon distance is 0.63 μm. Substrate bending or contamination on the medium or silicon surface can limit this minimal distance. However, as no bending of more than 100 nm over the medium and silicon wafer is observed with light white interferometry, in a large area, it is concluded that the presence of particles on the surface is determining this minimal distance of 0.63 μm. Apparently contamination is the limiting factor for the separation distance, in spite of the thorough cleaning efforts.

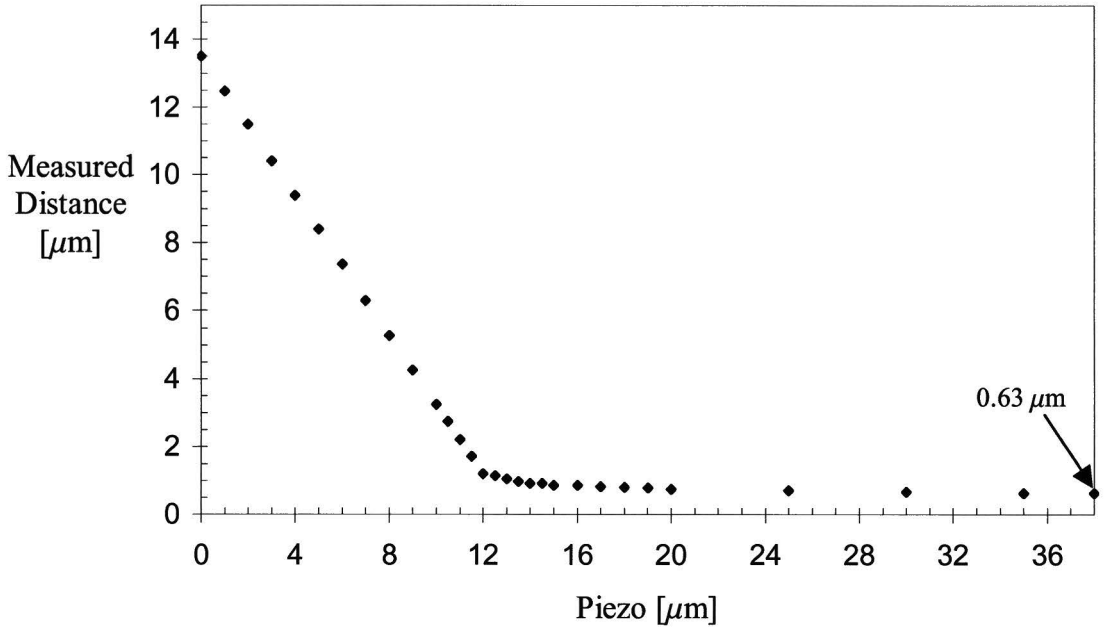

Fig. 4.4: Test of separation distance determination with the white interferometer. The test is done with the piezo. The vertical axis is the determined separation distance and the horizontal axis is the piezo position.

4.2.3 Interferometry on processed Si wafer with SiO_2 layer

As we have already addressed in the theory, 2.6.2, the actual sensor is embedded in a SiO_2 layer. This influences the medium sensor distance measurement considerably. To get an estimation of the influence we can calculate the reflection and transmission coefficients with equations (2.65) and (2.66), and substitute them into equation (2.64). If we do this for $n_1 = n_3 = 1.5$ and $n_2 = 1$ we get[24],

$$E = (0.2 \cdot e^{ik_1 x} + 0.96 \cdot e^{i(k_1 x + 2d_2 k_2)} \sum_{n=0}^{\infty} 0.04^n \cdot e^{i2d_2 k_2 n} (-0.2 + 0.96 \cdot e^{i2d_3 k_3} \sum_{m=0}^{\infty} 0.2^m \cdot e^{i2d_3 k_3 m})), \quad (4.1)$$

[24] Note that we have dropped the $I[k]$ factor. This is done because we are measuring normalized spectra.

in which we have taken the positive sign in equation (2.65). We see that the coefficient in the summation decrease as n and m increase, the reflections at the two interfaces become less important as they bounce back and forward. As an illustration we will calculate the intensity of the light if we take the first term of both summations into account and neglect all others. This gives,

$$I = 0.93 + 0.076 \cdot \cos[2d_2k] - 0.36 \cdot \cos[2d_3n_3k] + 0.36 \cdot \cos[2(d_2 + n_3d_3)k], \quad (4.2)$$

in which we have used $k_1 = k_2 = k$ and $k_3 = n_3k$. If we compare equation (4.2) with a measured spectrum of the medium and MTJ array, see Fig. 4.5, we see a striking resemblance. We see a slowly oscillation term, the $\cos[2n_3d_3k]$ term, with a rapid oscillation term of the same order magnitude superposed, the $\cos[2(d_2+n_3d_3)k]$ term. The amplitude of the $\cos[2d_2k]$ term is to small to be seen visually.

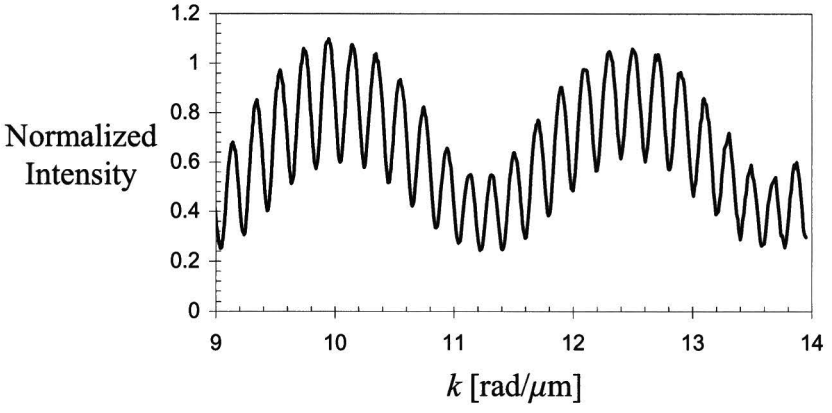

Fig. 4.5: Measured spectrum of the medium in combination with the MTJ array.

Remember that the Labview program determines the height from the peaks positions in the spectrum; it finds the positions of local maxima in the spectrum. Therefore it finds the period corresponding to the $\cos[2(d_2+n_3d_3)k]$ term. This implies that we have to subtract n_3d_3 from the value given by the program in order to obtain the correct medium sensor distance. There is a complication however, we have neglected a lot of reflections in the electrical field and it is entirely possible that an interference term, with a high oscillation but small amplitude, shifts the position of the peak values in the spectrum. In order to check the error in the peak determination method we have redone the calibration with the piezo, but now with the medium and MTJ array. Besides the peak determination method, we have also determined the distance between the medium and MTJ array, by fitting the measured spectrum with equation (4.1), using the first and second term of both summations. Before we can interpret these measurements we have to measure d_3, by making the distance between the medium and MTJ array larger than the coherence length. The measured spectrum is shown in Fig. 4.6, from it we can determine that $n_3d_3 = 1.25$ μm. This is done with the peak determination method. If we assume that $n_3 = 1.5$ this given $d_3 = 0.83$ μm, which corresponds with what we expect from processing.

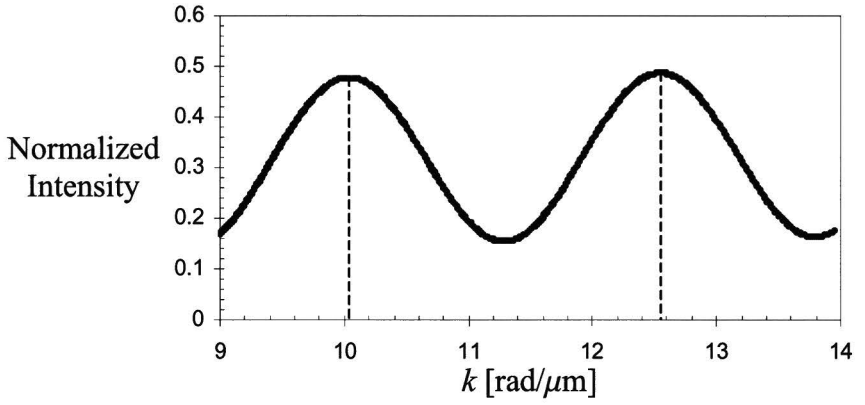

Fig. 4.6: Determination of SiO_2 thickness on the MTJ array. The distance is determined with the peak determination method.

The calibration measurement with the piezo, in the case of the medium in combination with the MTJ array is shown in Fig. 4.7.

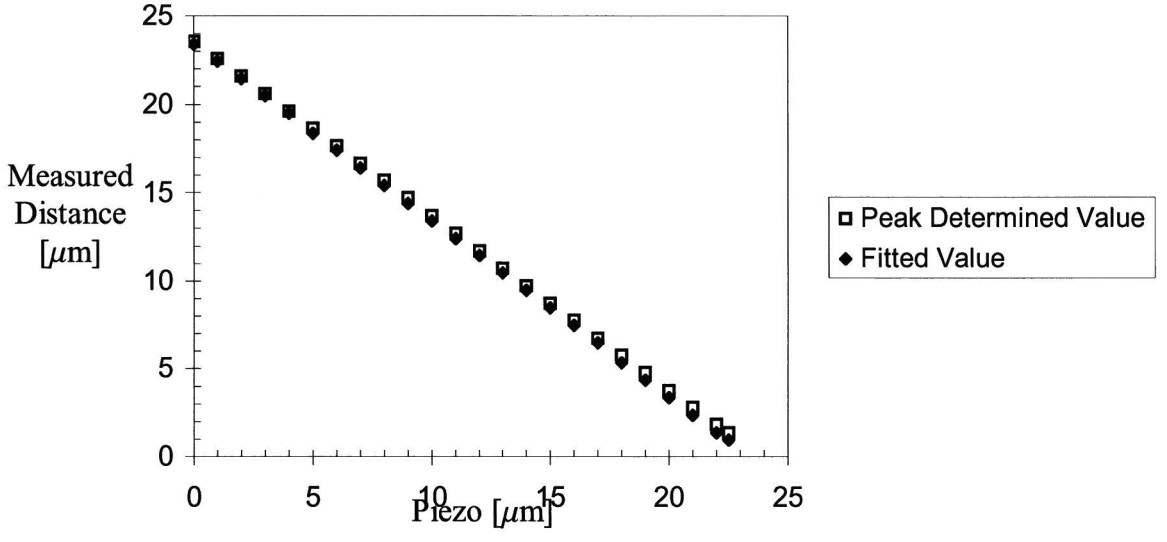

Fig. 4.7: Calibration of the separation distance determination, between the medium and MTJ array. The calibration is done with the piezo. The distance is determined with two different methods, the peak determination method and the fitting method.

As we can see there is little difference between the two methods, peak determination and fitting, when the distance between the medium and MTJ array is large. However, at a small separation there is a significant difference in both methods. This can be understood because at large separation distances the period of the $\cos[2(n_3d_3)k]$ term is a lot larger than that of the $\cos[2(d_2+n_3d_3)]$ term. In that case the local peaks in the spectrum are determined by the last term and we measure the correct distance. However, as we decrease d_2, the periods eventually become of the same order and the peak position determination method becomes unreliable. The difference between the two methods at the smallest separation distance is $d_{peak} - d_{fitted} = 1.36 - 0.95\ \mu m = 0.4\ \mu m$. Increasing the spectral width of the spectrometer can reduce this. This is because the program then detects two peaks of each period, which means that the distance is averaged and the error

reduced. We will not go into the details of why this is the case, what is important is that in this manner the error in the peak determination method is reduced to 0.1 μm at a separation distance of ~ 1 μm.

In conclusion of this paragraph, the monochromatic interferometer is suitable for establishing a parallel alignment of the medium and sensor planes. We can reduce the tilt between them to $8 \cdot 10^{-5}$ rad. We have calibrated the distance measurement versus the piezo position, with a medium and an unprocessed piece of silicon and observed that the white light interferometer is measuring the correct distance. Furthermore we found that the minimal obtainable separation distance between the medium (6x4 mm^2) and silicon (1x2 cm^2) is 0.63 μm, which is limited by contamination. We have investigated the influence of the SiO_2 layer on the sensor. We found that at small medium sensor distances the peak determination method is more unreliable than at large separation distances. We redid the calibration with the medium and MTJ array, and found an error of 0.1 μm for small distances (~ 1 μm).

4.3 Bit detection

In this paragraph we will present and discuss the measured magnetic fields from the various bit patterns. For the discussion we need to know the bit parameters, which are the height of the bits and the magnetization of the CoFe layer. The measurements of these two parameters are therefore shown in the beginning of this paragraph. The measured magnetic fields of each bit pattern are then presented individually, and we will discuss their differences and similarities. After that, we will investigate if the shape and magnitude of the measured magnetic fields corresponds with the theory. The measured signal versus the medium sensor distance is also discussed. In the last part of this chapter we display and discuss the measured signals from the MTJ array.

4.3.1 Bit parameters

The height of the bits is measured with an atomic force microscope (AFM) and a SEM; both measurements are shown in Fig. 4.8. The AFM measurement shows that the height of the bits is 0.1 μm, which is confirmed by the SEM picture. According to the processing of the medium, see paragraph 3.3, the height should be 1.1 μm. Apparently the 1 μm thick resist layer is not spin-coated during the processing of the medium. A schematic cross-section of a bit, in the case of the new bit parameters, is drawn in Fig. 4.9. The magnetic moment of the entire medium is measured with a SQUID magnetometer. This is converted to magnetization by dividing it with the volume of the CoFe layer, which is $1.9 \cdot 10^{-13}$ m^3. The measured hysteresis loop is displayed in Fig. 4.10; from the remnant state we determine that the magnetization at zero external field is $8.7 \cdot 10^3$ G, the saturation magnetization is $12 \cdot 10^3$ G. According to reference [11] on page 194, the saturation magnetization of $Co_{90}Fe_{10}$ is $18.5 \cdot 10^3$ G at room temperature and at an external field of $1.5 \cdot 10^3$ Oe. The measured saturation magnetization is thus in the correct order of magnitude. In order to be sure of the state of the magnetization during the experiment, an external field of 200 Oe is applied to the medium before the experiment.

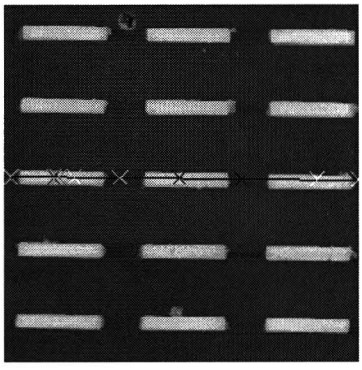

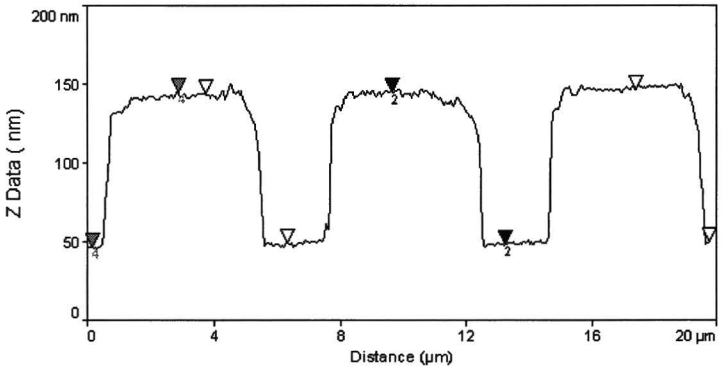

#	Distance	Height
1	2.60 µm	94.89 nm
2	3.59 µm	97.11 nm
3	2.34 µm	96.69 nm
4	2.73 µm	97.96 nm

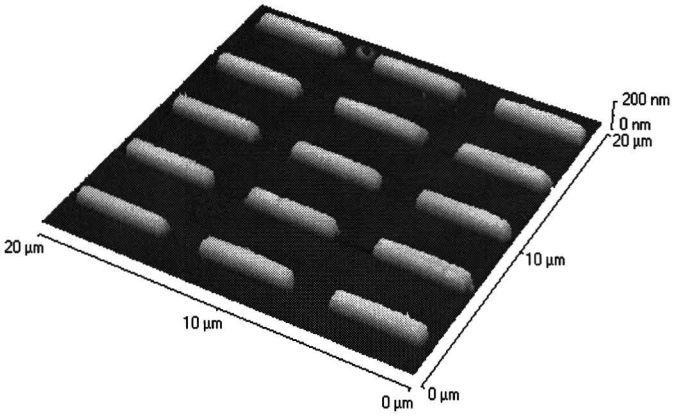

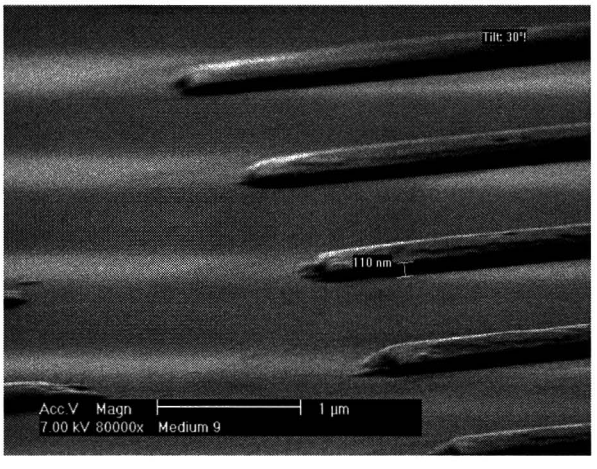

Fig. 4.8: In the upper picture the AFM measurement of the height of a bit is shown, in the lower picture the SEM measurement is displayed. The measured height is 0.1 μm. Both measurements are done after the deposition of the CoFe layer.

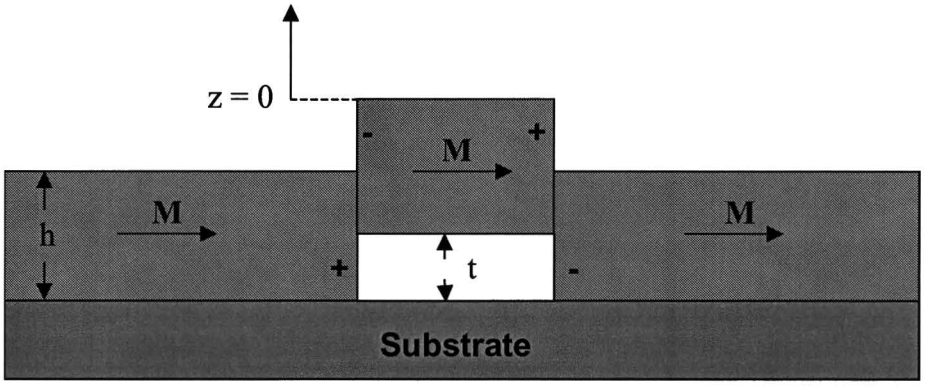

Fig. 4.9: Schematic cross-section of a bit according to the new bit parameters. Note that t is now the height of a bit and h is the thickness of the CoFe layer. This is because the CoFe layer is thicker than the height of a bit.

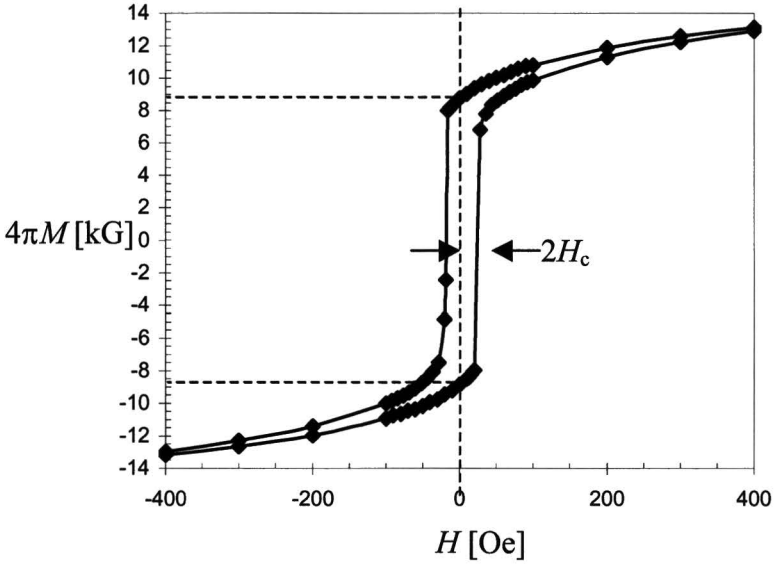

Fig. 4.10: Hysteresis loop of magnetization of the CoFe layer on the medium. The measurement is done with a SQUID magnetometer at room temperature.

4.3.2 Magnetic field of each bit pattern

In order to get an indication of the noise contribution in the measured signal, a measurement of the medium is done at a height of $d_2 = 11.5$ μm, it is shown in Fig. 4.12. We can see that the measured signal is almost constant. The stripes in the signal coincide with the direction in which the medium is scanned, and it appears that the signal is decreasing with increasing x_2. An explanation for this can be that we are measuring the magnetic field, created by the entire CoFe layer on the medium. Both effects are too small to interfere with bit detection.

The measured magnetic fields of each bit pattern are shown in Fig. 4.13 to Fig. 4.16. In each figure a schematic picture of the bit pattern is shown in the upper right corner. Bit patterns A, B and D are all measured with the single junction. Bit pattern C is measured with the middle element of the

MTJ array. In all four cases the medium is scanned over a range of 100 μm in both the x_1 and x_2 direction. The settings at which the measurements are done are listed with the figures. If we compare the four measurements with each other, we notice that the signal in Fig. 4.13 and Fig. 4.14 are better defined than the measurement shown in Fig. 4.15 and Fig. 4.16. The measurement displayed in Fig. 4.15 is less defined, because the used step size in the x_2 direction is larger. Fig. 4.16 is less defined, because the bit pattern is not as closely packed, plus the separation distance is less. Notice that the amplitude of the measured signal increases as the separation distance decreases, we will come back to this later.

The measured magnetic field of bit pattern A is displayed in Fig. 4.13. It is measured with the single junction at a medium sensor distance of $d_2 = 1.5$ μm. If we look at Fig. 4.13 we can clearly observe a periodic signal in the x_2 direction, with a period of 7 μm. This corresponds with the pitch of the bit pattern in the x_2 direction. We also expect to see an oscillation of the signal in the x_1 direction, but this is not visible in the measured signal. There seems no correlation between the modulation of the measured signal in the x_1 direction and the bit pattern, except where the bit pattern ends. Notice that the measured magnetic field near the bit pattern also fluctuates and is not constant. This indicates the presence of magnetic poles in the CoFe layer on the substrate, which means that it is not homogenously magnetized; see equation (2.6) in the theory. The fact that we do not observe oscillations in the x_1 direction can be understood, if we schematically draw the sensor with respect to the bit pattern. This is done in Fig. 4.11. Because the dimension of the MTJ element in the x_1 direction, 5 μm, is larger than the pitch in that direction, 4 μm, the oscillations are averaged out. For the x_2 direction this is not the case and we do measure the oscillation. A last observation of the measured signal in Fig. 4.13 is that the magnetic field is always positive. This is not what we expected; see for example Fig. 2.11 in paragraph 2.3.1. Apparently there is an offset in the resistance of the single junction. A explanation could be, that the magnetic cores of the Helmholtz coils have a little remnant magnetization, which is calibrated away with the Hall probe.

In Fig. 4.14 the measured signal from bit pattern B is displayed, measured at a medium sensor distance of $d_2 = 1.6$ μm. We again observe the oscillations in the x_2 direction with a period of 7 μm, and we do not observe any oscillations in the x_1 direction. The triangular shape of the bit pattern can be distinguished and we can see where the bit pattern ends. The amplitude of the oscillation is less at the end of the triangular bit pattern; see the circles in Fig. 4.14, than right above the triangular bit pattern. This is because we are measuring the signal of two bits at the end of the triangle. Again we notice that the CoFe layer is not magnetized homogeneously, because the measured signal fluctuates at positions where the bits are absent.

If we look at Fig. 4.15 we see the measured magnetic field of bit pattern C, measured at a medium sensor distance of $d_2 = 1.38$ μm. The signal displays large irregular fluctuations in the x_1 direction. Because of these fluctuations we cannot see the missing bits in the bit pattern. Notice that the amplitude of the oscillation in the x_2 direction is larger than in the previous two measurements. This is because the medium sensor distance is smaller. Once again we can see where the bit pattern ends, and we notice that the magnetic field fluctuates at positions where no bits are present.

The measured magnetic field of bit pattern D, see Fig. 4.16, is measured at a medium sensor distance of $d_2 = 1.12$ μm. This is the smallest distance of the four measurements. Notice that the range on the z-axes is different; this is because the signal is larger due to the smaller medium

sensor distance. We should be able to recognize groups of five bits and individual bits in the measured signal. This is difficult due to the background noise created by the CoFe layer. However, we can try to locate them by presenting the measured signal differently. In Fig. 4.17 the same signal is plotted in grayscale and seen from above. In the right picture the bit pattern has been added for comparison. Note that it is difficult to recognize any structure in the picture; there are many fluctuations in the signal, which cannot be attributed to the bit pattern. The six groups of five bits seem to be slightly visible in the measured signal, although the individual bits are much more difficult to recognize. This can be understood from the bit sensor orientation, see again Fig. 4.11. When the sensor is above a group of bits we are measuring the signal from more than one bit, and the signal is larger.

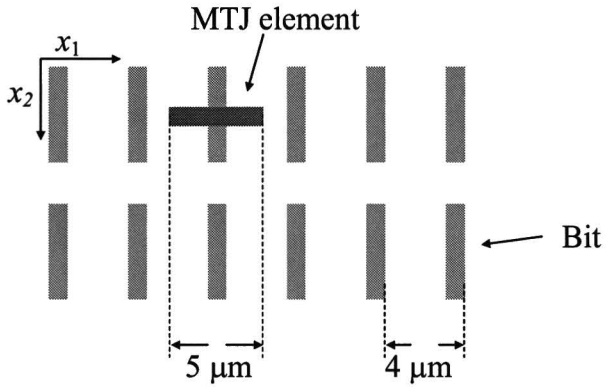

Fig. 4.11: Schematic picture of the orientation of the MTJ element with respect to the bits.

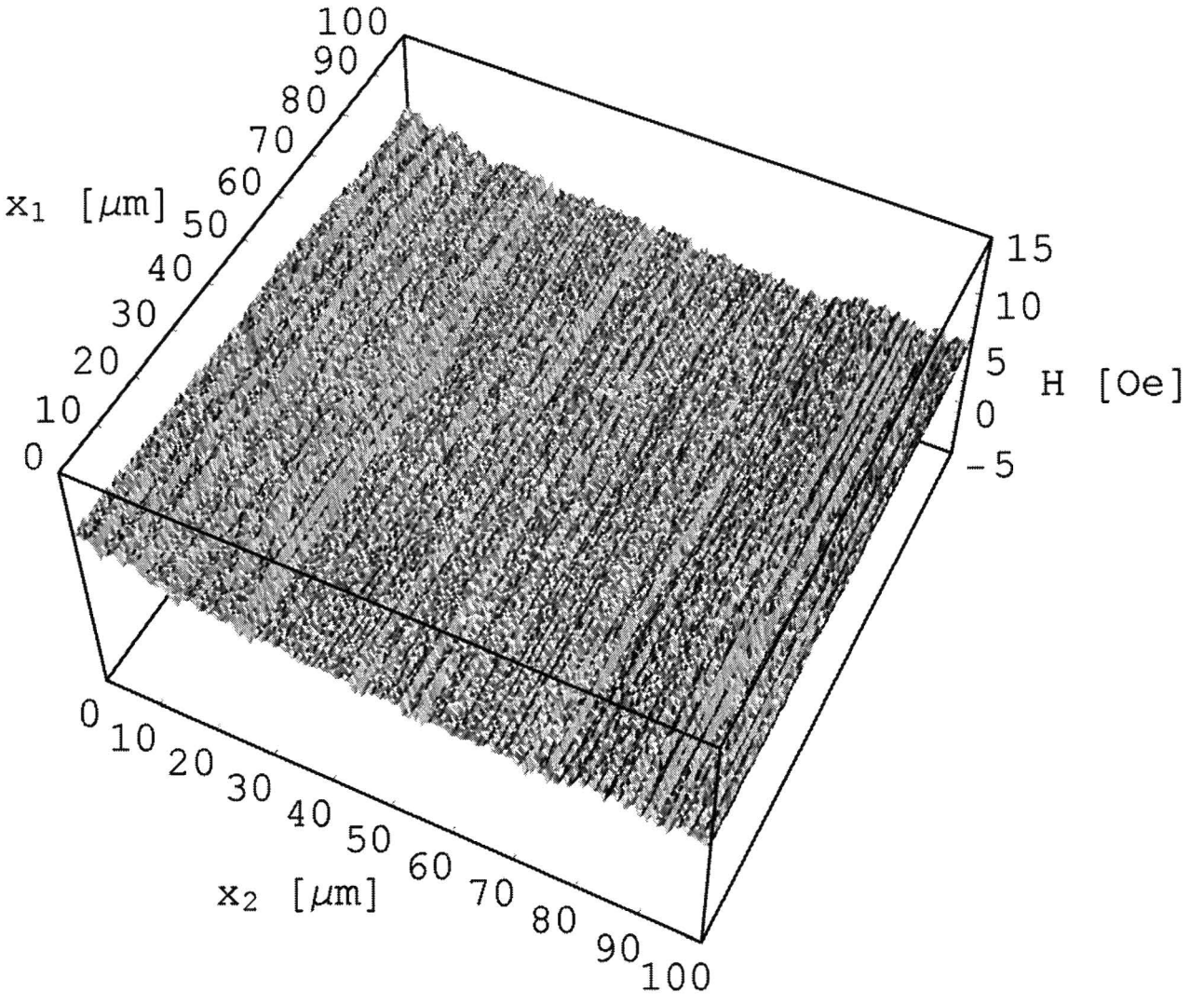

Fig. 4.12: Three-dimensional plot of the measured magnetic field. The measurement was done with the single junction. The (x,y) nanopositioner made steps of 0.5 μm in the x and y direction. The medium sensor distance is measured to be, d_2 = 11.5 μm. An ac-current with a frequency of 900 Hz is used to measure the resistance. The magnitude (rms value) of the current is $I_{measure}$ = 10 μA and the lock-in amplifier low pass filtering settings are: 10 ms integration time and a 12 dB attenuation factor

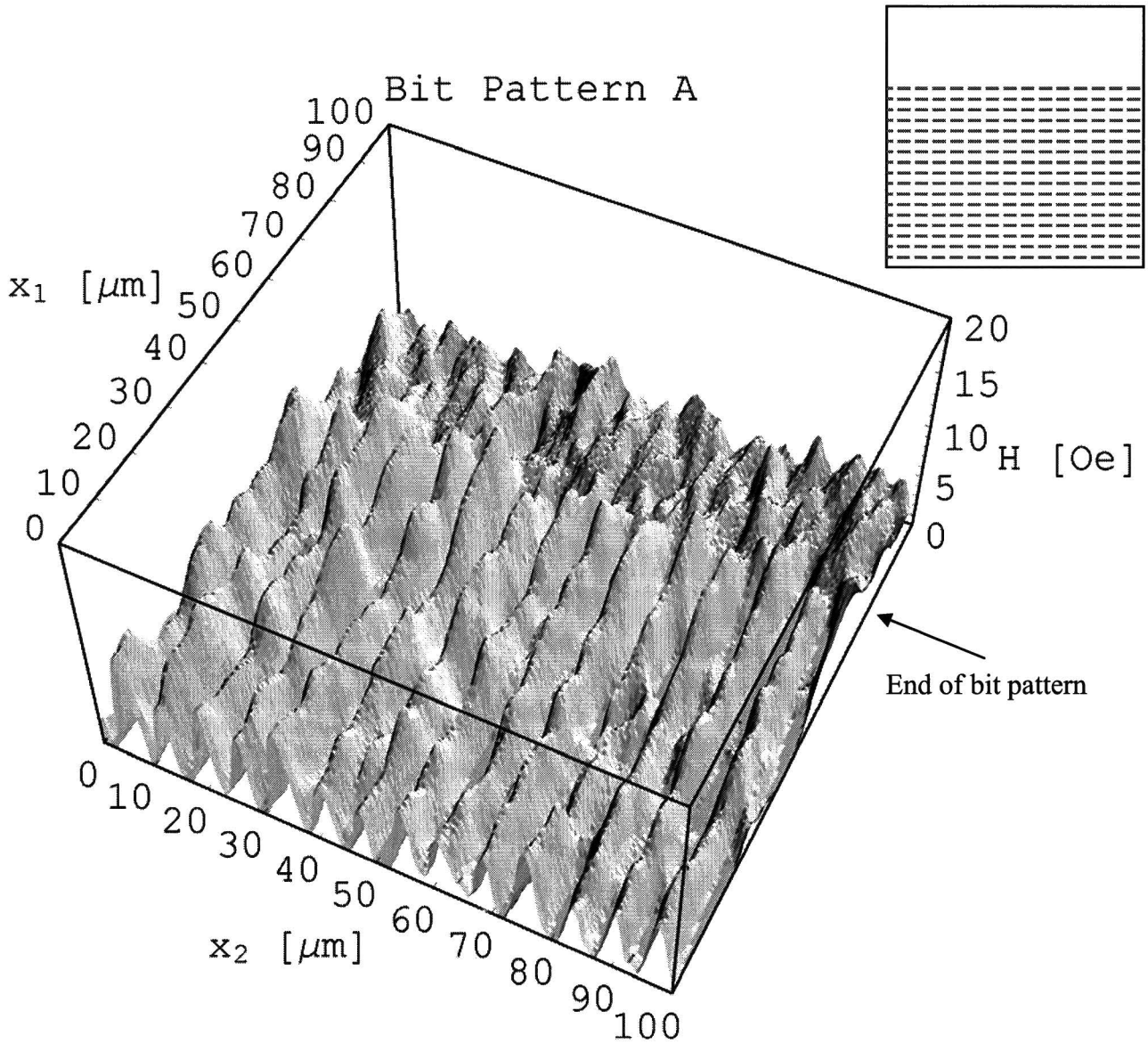

Fig. 4.13: Three-dimensional plot of the measured magnetic field of bit pattern A. In the upper right picture the bit pattern is drawn schematically. The measurement is done with the single junction. The (x,y) nanopositioner made steps of 0.5 μm in the x and y direction. The medium sensor distance is measured to be, d_2 = 1.5 μm. An ac-current with a frequency of 900 Hz is used to measure the resistance. The magnitude (rms value) of the current is $I_{measure}$ = 10 μA and the lock-in amplifier low pass filtering settings are: 10 ms integration time and a 12 dB attenuation factor

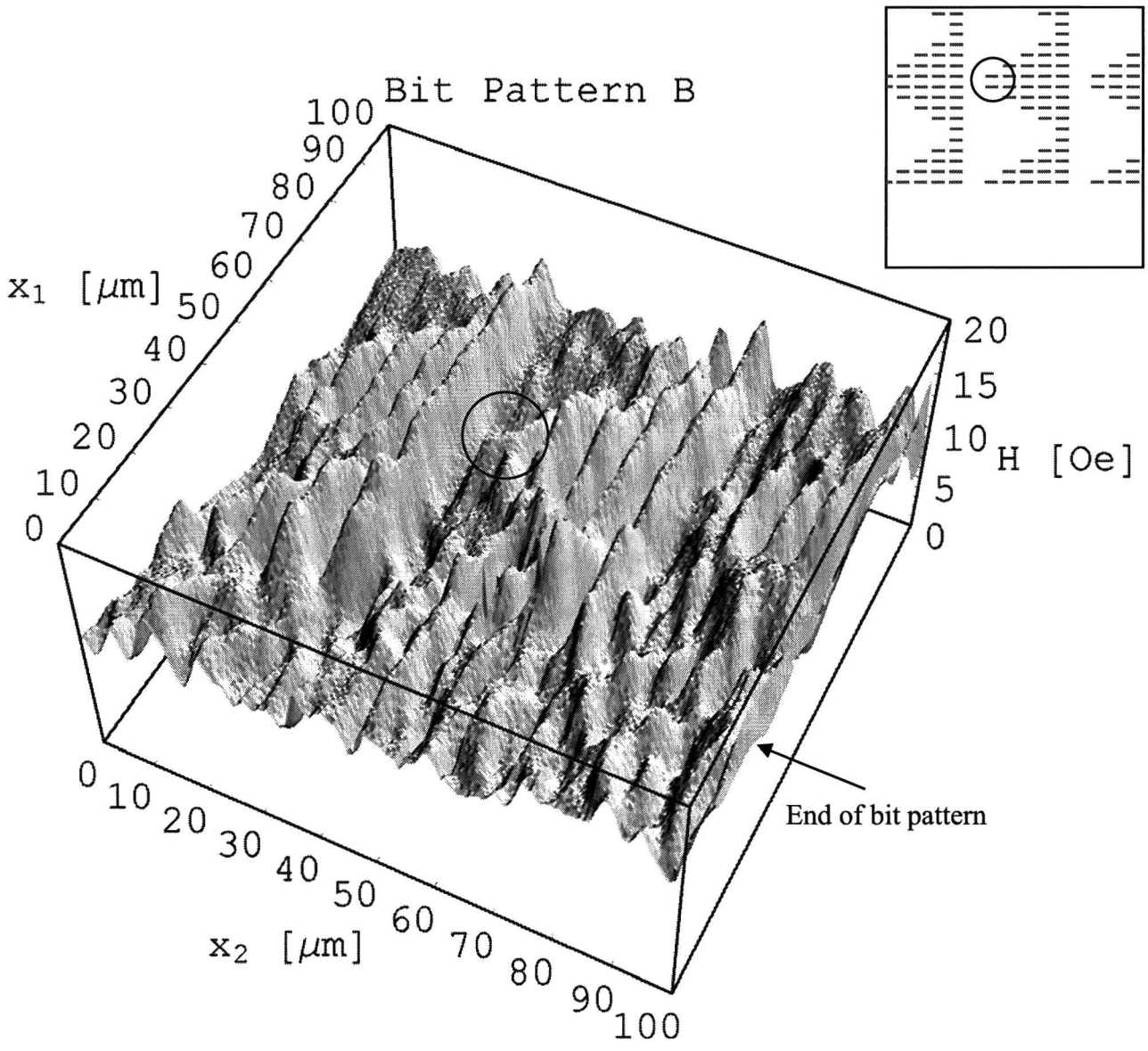

Fig. 4.14: Three-dimensional plot of the measured magnetic field of bit pattern B. In the upper right picture the bit pattern is drawn schematically. The measurement is done with the single junction. The (x,y) nanopositioner made steps of 0.5 μm in the x and y direction. The medium sensor distance is measured to be, $d_2 = 1.6$ μm. An ac-current with a frequency of 900 Hz is used to measure the resistance. The magnitude (rms value) of the current is $I_{measure} = 10$ μA and the lock-in amplifier low pass filtering settings are: 10 ms integration time and a 12 dB attenuation factor

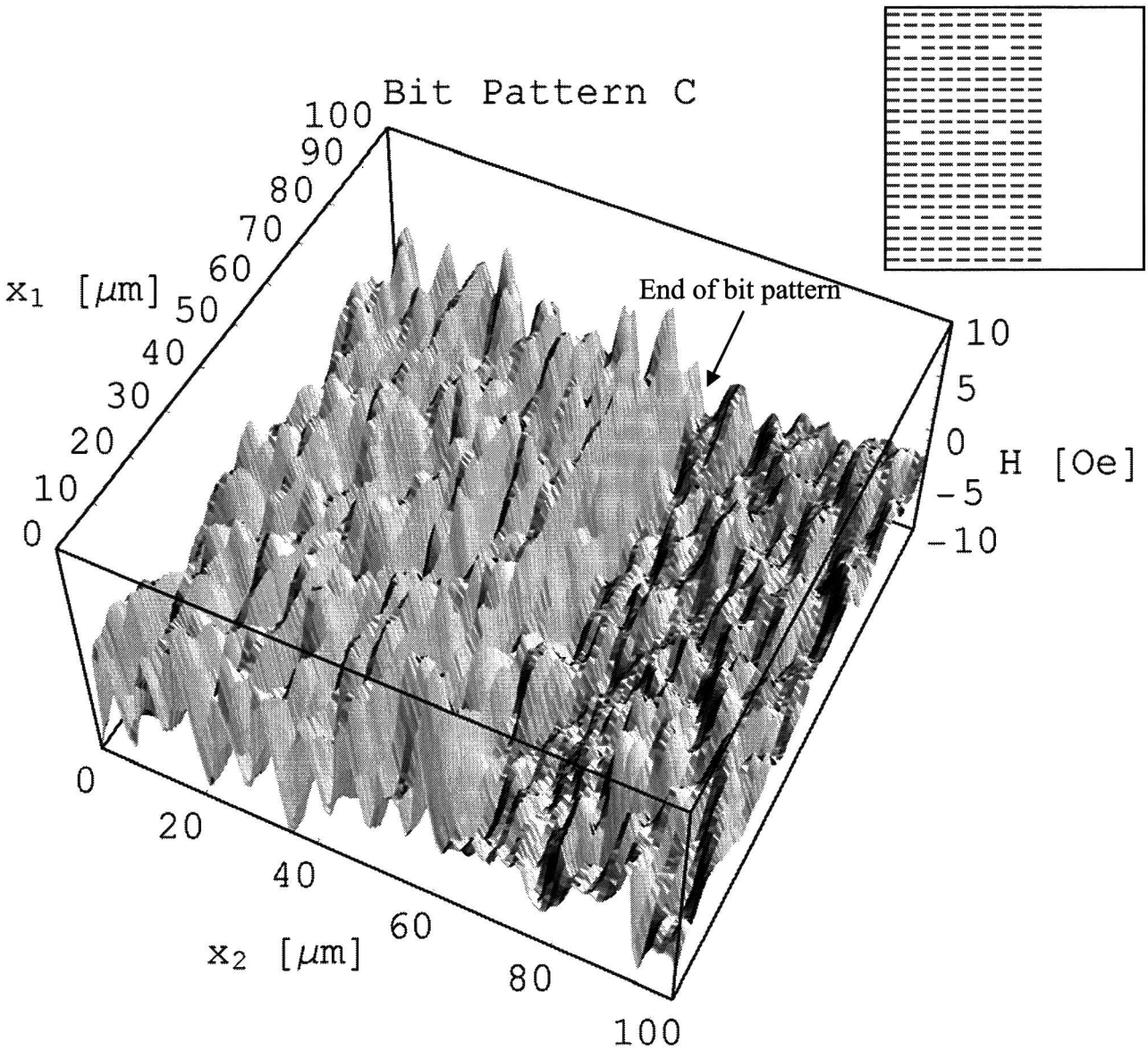

Fig. 4.15: Three-dimensional plot of the measured magnetic field of bit pattern C. In the upper right picture the bit pattern is drawn schematically. The measurement is done with the middle element of the MTJ array. The (x,y) nanopositioner made steps of 0.5 μm in the x direction, and steps of 1 μm in the y direction. The medium sensor distance was measured to be, d_2 = 1.4 μm. The used settings for the multiplexer and lock-in are; V_{in} = 0.1 V, R_{gain} = 10 kΩ, 10 ms integration time, 12 dB attenuation and a frequency of 900 Hz.

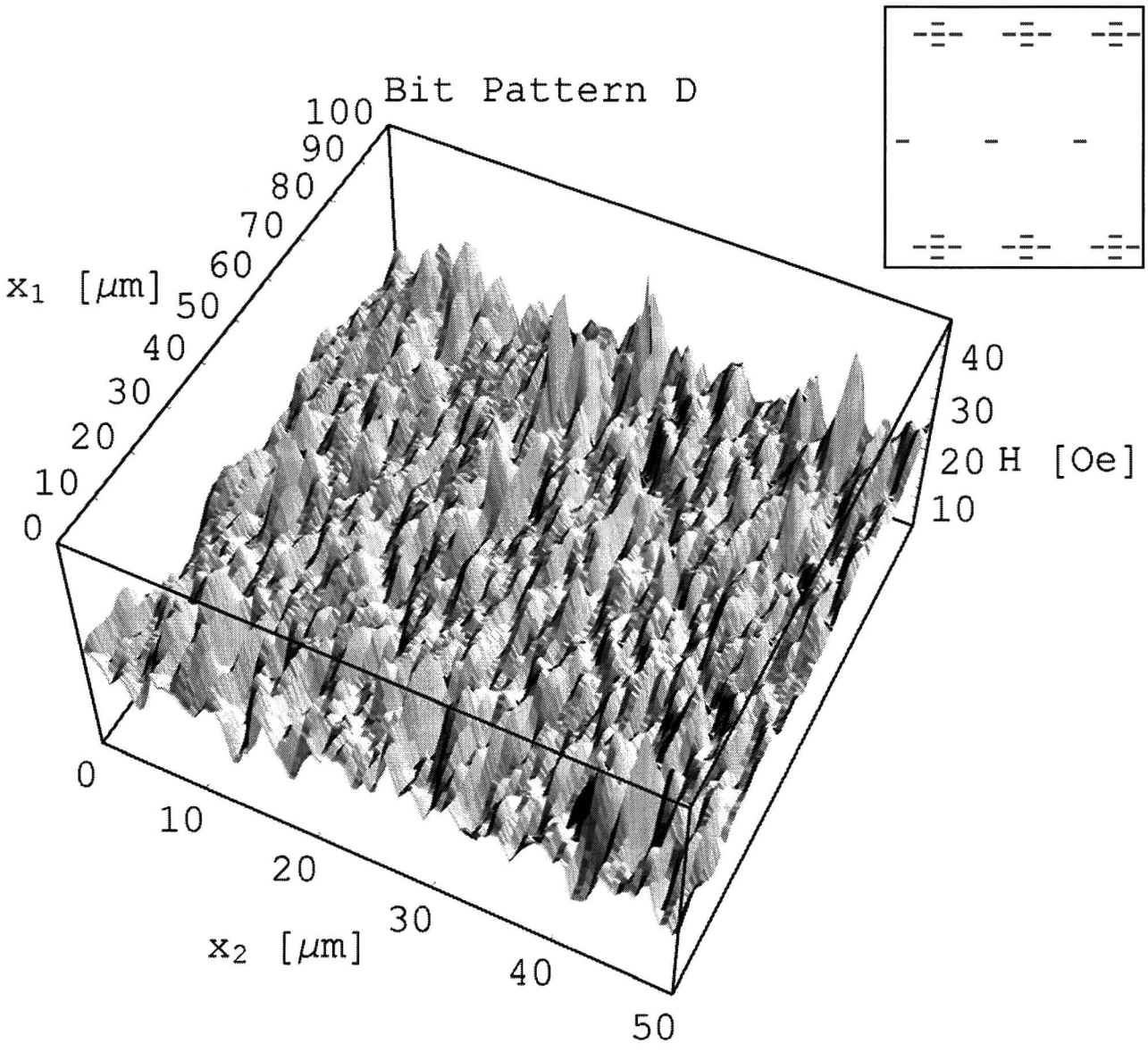

Fig. 4.16: Three-dimensional plot of the measured magnetic field of bit pattern D. In the upper right picture the bit pattern is drawn schematically. The measurement is done with the single junction. The (x,y) nanopositioner made steps of 0.5 μm in the x and y direction. The medium sensor distance was measured to be, d_2 = 1.1 μm. An ac-current with a frequency of 900 Hz is used to measure the resistance. The magnitude (rms value) of the current is $I_{measure}$ = 10 μA and the lock-in amplifier low pass filtering settings are: 10 ms integration time and a 12 dB attenuation factor

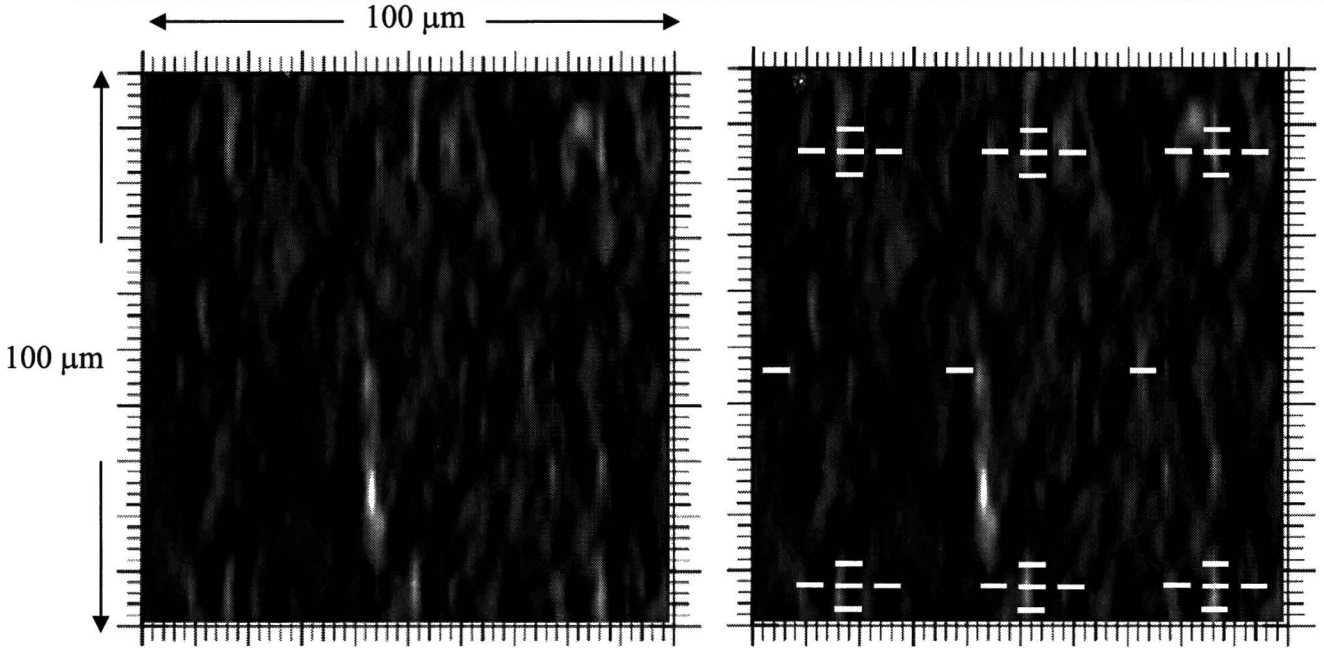

Fig. 4.17: The measurement shown in Fig. 4.16, seen from above and plotted in a grayscale. In the right picture the bit pattern has been drawn in it for comparison. A white color corresponds with 40 Oe, black with 10 Oe.

In conclusion of this paragraph, we have shown that the noise contribution does not interfere with the bit detection. Because of the sensor bit orientation, see Fig. 4.11, we only observed oscillations in the x_2 direction of the measured signal. The sensor averages out the oscillations in the x_1 direction. This is the case for all four bit patterns. Bit patterns A and B can be recognized in the measured signal. The position at which a bit is missing in bit pattern C cannot be recognized due to large irregular fluctuations of the signal in the x_1 direction. In the measured signal of bit pattern D we observe groups of five bits. Single bits are difficult to detect and can hardly be recognized. The reason that groups of bits are easier to detect is because the sensor integrates the signal over a few bits. From all four measurements we can determine that the CoFe layer is not in one magnetic domain. This can be concluded from the fact that the measured signal shows fluctuations, which cannot be attributed to the noise or the bit patterns. A last observation is that the measured magnetic field increases if the medium sensor separation decreases. This will be investigated in more detail in the next part of the paragraph.

4.3.3 Comparison with theory

We can make a theoretical calculation of the magnetic field at a certain height, see paragraph 2.3.2 of the theory, and compare it with the measured magnetic field. In Fig. 4.18 a calculation of the magnetic field of bit pattern B is shown. To save computational time only a part of the bit pattern is calculated, it is shown in the lower right corner. It was done for $x_3 = 1.55$ μm, which corresponds with $d_2 = 1.6$ μm. The x_1-x_2 range and scale are kept the same as in Fig. 4.14 to make the comparison easier. In order to make the peaks in the calculated signal visible above a bit, we have defined the positive magnetic field direction in the opposite direction of the magnetization. If we look at the calculated signal we can recognize the triangular shape of the bit pattern. Furthermore we see the peaks and valleys belonging to poles of the bits, and we observe that the signal is periodic in the x_1 and x_2 direction. Note that the signal varies around zero field and that

the calculated magnetic field shows no fluctuations at positions where the bits are absent. The calculated signal has the same order of magnitude as the measured signal, but the shape is different. The oscillations in the x_1 direction are not visible in the measured signal because the size of the MTJ element is too large; they are averaged out to one big peak. For an illustration of this, see again Fig. 4.11.

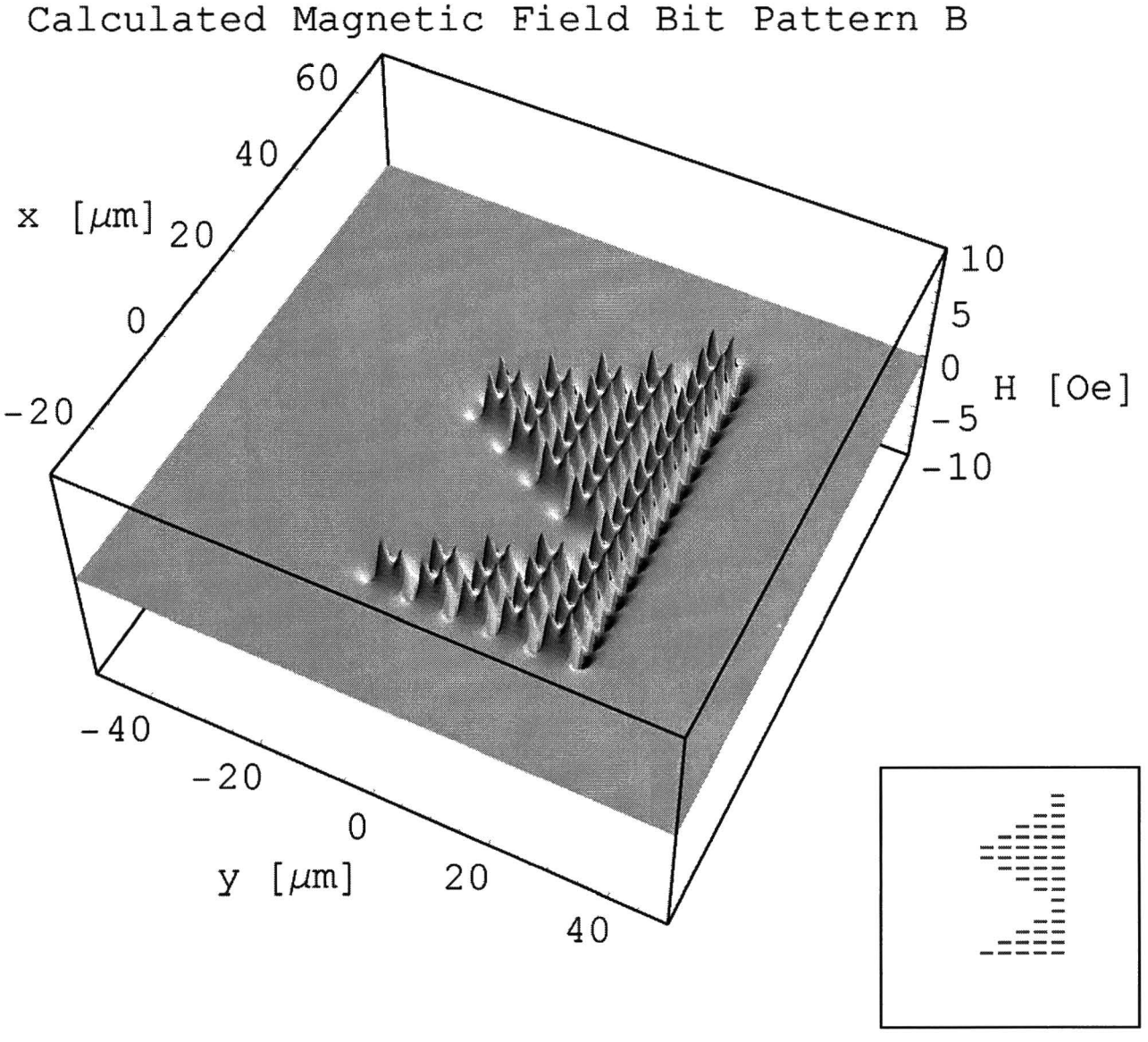

Fig. 4.18:Theoretical calculation of magnetic field of bit pattern B. The field is calculated at 200x200 points. The calculation is done for x_3 = 1.55 μm, which corresponds with d_2 = 1.6 μm. In the lower right picture the corresponding bit pattern is showed.

In order to obtain a more detailed quantitative comparison between the amplitude and shape of the measured and theoretical signal, another measurement of the magnetic field is done. This time the medium is not scanned in the x_1 and x_2 direction, but only in the x_2 direction using a smaller step size. The medium sensor distance is made as small as possible. This resulted in a separation distance of $d_2 = 0.95$ μm and a step size of 0.167 μm. Bit pattern A is used as medium. The measurement will be compared with the calculated sensor signal. With sensor signal we mean the averaged value of the calculated magnetic field over the sensor divided by the sensor area. The averaged value is calculated for 35 points, 7 in the x_1 direction and 5 in the x_2 direction. The measurement and calculated sensor signal are shown in Fig. 4.19.

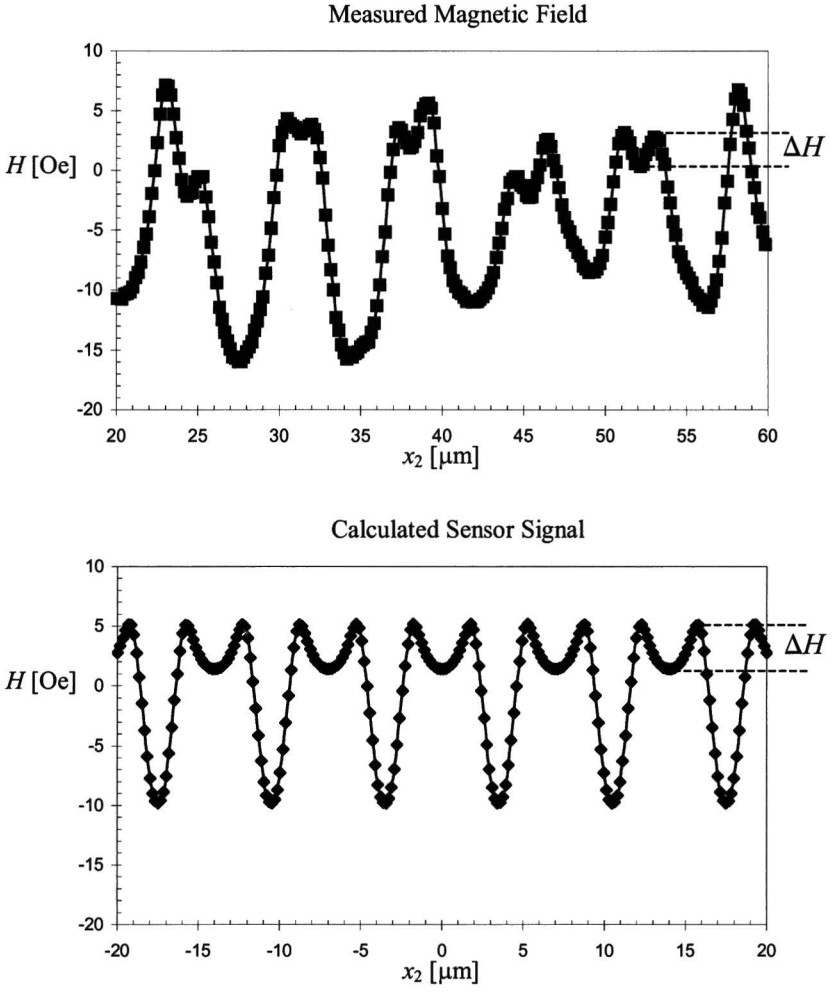

Fig. 4.19: Measured and calculated signal of bit pattern A, for $d_2 = 0.95$ μm. An ac-current with a frequency of 900 Hz is used to measure the resistance. The magnitude (rms value) of the current is $I_{measure} = 10\ \mu A$ and the lock-in amplifier low pass filtering settings are: 10 ms integration time and a 12 dB attenuation factor

The order of magnitude of the calculated and measured magnetic field is the same, the measured signal oscillates over a range of ~ 20 Oe, the calculated signal over a range of 15 Oe. Both signals have a period of 7 μm and their shape show a strong resemble, both having a tooth-like shape. There are also differences between the two curves. The amplitude of the oscillations of the measured signal is not constant and the shape is not always the same. The positive peaks in the

measured signal, indicated with ΔH in Fig. 4.19, are typically smaller and closer together, and the valleys are wider. This indicates that the magnetic poles of the bits are not at the edges of the bits but translated inwards. An explanation is that the a bit is mainly in one magnetic domain, but not at the edges of the bit. To illustrate this, we have calculated the magnetic structure of the CoFe layer on top of the bit. The dimensions of the CoFe layer are 5x1x0.2 μm (l x w x h). The calculation is done with the package called, Object Oriented MicroMagnetic computing Framework (OOMMF). The package requires the input of the saturation magnetization M_s, the exchange constant A, the crystalline anisotropy constant K_1 and the damping coefficient. From Fig. 4.10 we can determine that $4\pi M_s = 12 \cdot 10^3$ G and $K_1 = 2\mu_0 M_s H_c = 4 \cdot 10^4$ erg/cm^3, see paragraph 2.2.2. In the literature we have found values for K_1 at room temperature of Co_0Fe_{100} to $Co_{70}Fe_{30}$, but not for $Co_{90}Fe_{10}$. The literature values are listed in Table 4.4.

Co	Fe	K_1 [ergs/cm^3]
0	100	$42 \cdot 10^4$
30	70	$10 \cdot 10^4$
40	60	$4.5 \cdot 10^4$
50	50	$-6.8 \cdot 10^4$
70	30	$-43 \cdot 10^4$

Table 4.4: Literature values of K_1 for various CoFe alloys at room temperature. Taken from reference [11] at page 570.

As we can see there is a strong dependence of K_1 on the alloy composition. If we extrapolate the literature values linearly we obtain $K_1 = -59 \cdot 10^4$ ergs/cm^3 for $Co_{90}Fe_{10}$. This is a factor 15 larger than the measured value. The exchange constant has been chosen $A = 30 \cdot 10^{-12}$ J/m. The damping is not relevant in our case, it is necessary for describing the time evolution of the magnetization. We have chosen it to be 0.5. The calculation starts with a random magnetization in each cell. The result of the calculation is shown in Fig. 4.20, in the left picture the magnetic structure is calculated when an external magnetic field of 10^3 Oe is applied. The right picture shows the magnetic structure after the field is removed.

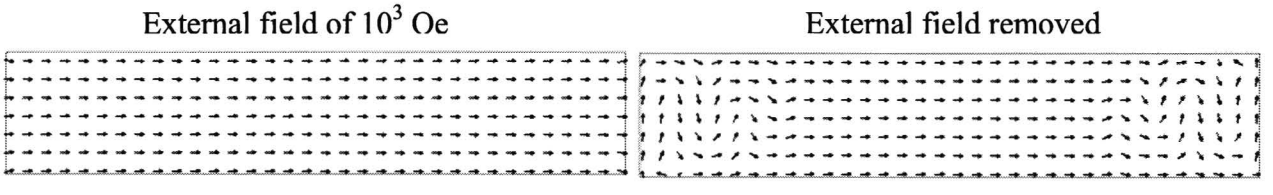

Fig. 4.20: Calculated magnetic structure of the CoFe layer on top of bit. The dimensions of the CoFe layer are 5x1x0.2 μm (l x w x h). The other parameters used for the calculation are $4\pi M_s = 12 \cdot 10^3$ G, $K_1 = 4 \cdot 10^4$ erg/cm^3, $A = 30 \cdot 10^{-12}$ J/m and the damping coefficient is 0.5. The used cell size is 50 nm.

If we look at the right picture, we see that the CoFe layer is indeed not in one magnetic domain. However, the large middle part is magnetized homogenously, and the domains form at the edges of the CoFe layer. This support the previously made hypothesis that a bit is mainly in one magnetic domain, but not at the edges of the bit.

The scan shown in Fig. 4.19 is not only done at $d_2 = 0.95$ µm, but also at different medium sensor distances in order to measure how the signal evolves as a function of the separation distance. The

scans are plotted in Fig. 4.21. We see that the amplitude of the signal decreases as the separation distance increases. Furthermore we notice that, with increasing separation distance, the signal starts to behave as a cosine with a period of 7 μm. This can be understood from the theory of a bit pattern, see paragraph 2.3.2. It was found that the Fourier components of the magnetic field each decays exponentially with their wave number. The smallest wave number present in the signal is corresponding to the pitch of the bit pattern, and therefore the component with this wave number will become dominant with increasing distances.

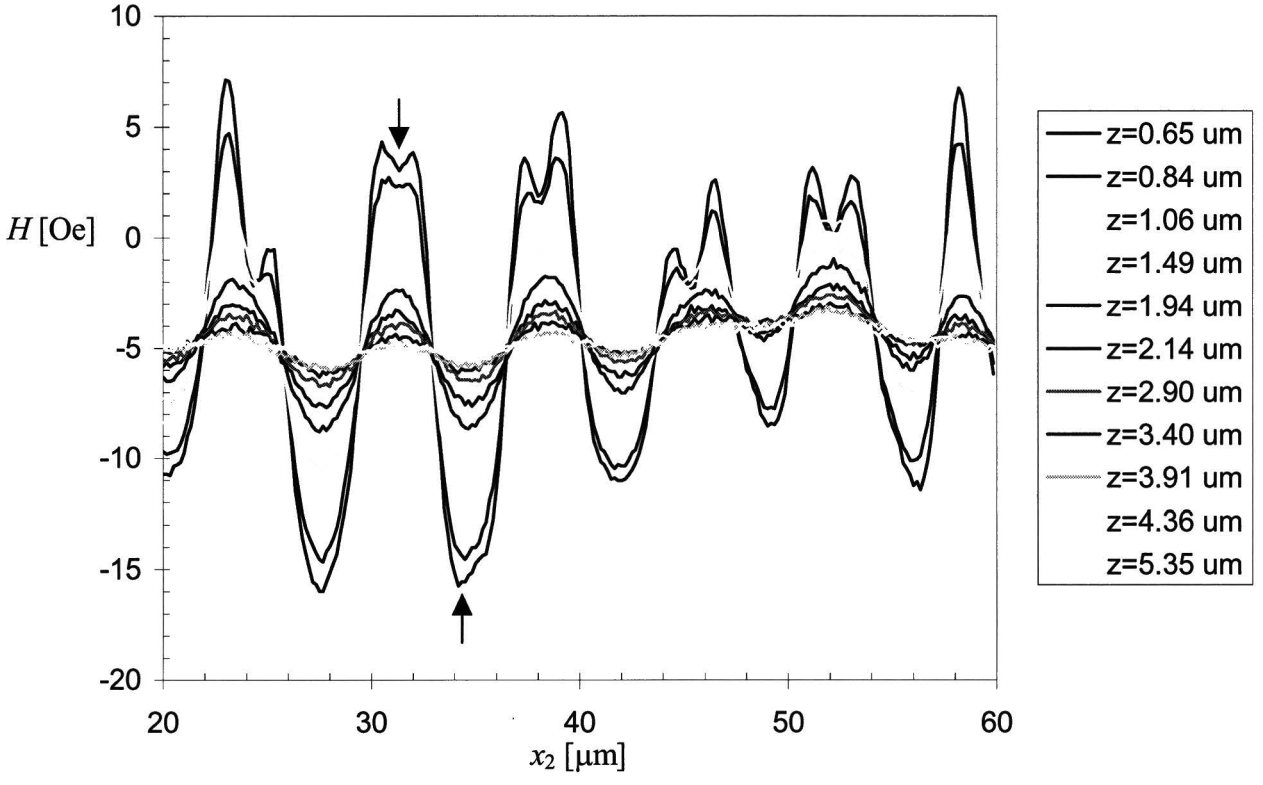

Fig. 4.21: Plot of scan of bit pattern A in x_2 direction, at different medium sensor distances. The arrows indicate the position at which the amplitude is determined. An ac-current with a frequency of 900 Hz is used to measure the resistance. The magnitude (rms value) of the current is $I_{measure}$ = 10 μA and the lock-in amplifier low pass filtering settings are: 10 ms integration time and a 12 dB attenuation factor

In order to compare the decay of the measured signal with Fourier theory we have recalculated the Fourier component of the magnetic field with the new bit parameters, see paragraph 2.5 and 7.3. Because the length of the MTJ element is almost the same as the pitch in the x_1 direction we have calculated the Fourier component at $k_1 = 0$, and divided it by the length of the MTJ element. This is the same as taking the average of the magnetic field over the sensor. Furthermore, because we have only scanned the oscillating component in the x_2 direction we expect the amplitude of the measured signal to decay exponentially with $k_2 = 2\pi / 7 = 0.90$ μm^{-1}. The measured and calculated amplitude at various separation distances are plotted logarithmically in

Fig. 4.22. The measured amplitude is determined at the two positions indicated with arrows in Fig. 4.21, because this gives the largest amplitude. At small separation distances the measured values are approximately a factor two larger than the calculations. We observe a good match between the theoretical and measured values at large separation distances. This is because at smaller

separations distances, the exact magnetic structure of the CoFe layer becomes more important, and the components with higher wavelengths are still present in the measured signal. As the separation distance increases, the components with higher wavelengths and the exact magnetic structure both become less important, and we only measure the component corresponding to the pitch of the bit pattern; this is precisely the component for which the Fourier theory applies. Notice that if we chose a different location in Fig. 4.21 to determine the amplitude, the measured amplitude reduces, and we find a better match between the calculated Fourier component and the measured amplitude. This brings us to the conclusion that the Fourier analysis gives the correct order of magnitude for the Fourier component critical for bit detection, at least for large separation distances. Note that the Fourier components are calculated without the use of a fitting parameter, all parameters are known or measured.

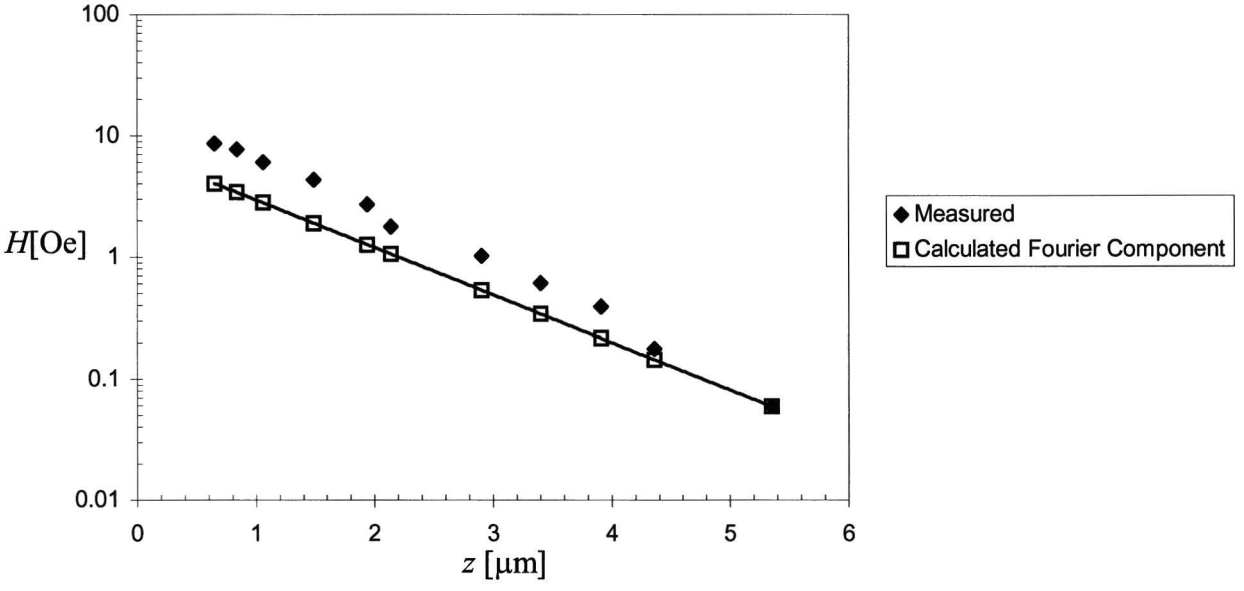

Fig. 4.22: Logarithmic plot of the measured and calculated amplitude of the Fourier component of the magnetic field, critical for bit detection, versus the separation distance.

To conclude the comparison between theory and experiment, we have shown that the theory predicts the right order of magnitude of the measured signal. The shape of the measured signal also shows a similar behavior as the theoretical signal. However, the measured signal is more irregular and it appears that the magnetic poles of the bits are closer together. This indicates that the bits are mainly in one magnetic domain, and that magnetic subdomains do form at the edges of a bit. This is confirmed by a calculation of the magnetic structure with the OOMMF package. The exponential decay of the calculated Fourier component shows a good match with the amplitude of the measured signal, at least at large separation distances. At smaller distances, ~ 1 μm, the measured amplitude is approximately a factor two larger than the calculated Fourier component. This is because at these distances the components with higher wave numbers are also present in the measured signal and the magnetic structure of a bit is more important.

4.3.4 MTJ array

The last subject is the measurement of bit pattern B with the MTJ array. The measurement is done by scanning the medium in a range of 100 x 100 μm, with a step size of 2 μm in both directions. At every step the resistance of each element in the MTJ array is measured. The element at row and column three is not measured because the tunnel barrier is shorted. The measurement is done at a separation distance of d_2 = 1.4 μm. The measured signal of each element is displayed in Fig. 4.23; in the corner the row and column numbers of the elements are listed. The triangles are drawn as a guide to the eye, in each picture the same part is highlighted. We see that the difference between two measurements is a spatial translation of the measured signal. For example, if we look at the measurement with element 2,2 and compare it with the measurement with element 2,1, we see the same picture translated to the right. This is because element 2,2 is to the left of element 2,1. If we compare two elements on a different row we observe that the signal is translated up or down. If we look between the triangular shapes, we see once again fluctuations in the measured signal, which come from the CoFe layer and not from the bit pattern. To give an indication of the amplitude of the measured signal, cross-sections of the measured magnetic fields of the second column are shown in Fig. 4.25. The cross-sections are taken along the dashed lines in Fig. 4.23. The amplitudes of the elements in other columns are in the same order of magnitude. If we look at Fig. 4.25, we see that each element measures the same signal, only translated over 7 μm in the x_2 direction. All the three signals vary in a range of ~ 15 Oe, which is the same range as the single junction at a separation distance of d_2 = 1.4 μm. The oscillations of the measured magnetic fields have a period of 7 μm, which corresponds with the bit pattern. Furthermore we notice that the amplitude of the signal is lower at the end of the triangular bit pattern than above it. In Fig. 4.24 as well as in Fig. 4.23 and Fig. 4.25, two arrows are drawn to illustrate what is meant with the end of the triangular bit pattern. The reason the signal is less, is because we are only measuring the signal of two bits, instead of more. Finally, we note that element 3,2 has a different offset than element 1,2 and 2,2, this is due to the shorted element in the third row. This is also the case for element 3,1.

In conclusion, each element of the MTJ array can be read out individually without influence from other elements. They all produce the same magnetic field, only translated because each element is located at a different position. This also applies for the two remaining elements on the third row. Even though one of the elements on that is row is shorted, they still can be used as sensor. However, due to the short, element 3,2 has a different offset than element 1,2 and 2,2. This is also the case for element 3,1. The measured signals all vary in a range of ~ 15 Oe, which is the same as the single junction, at a separation distance of d_2 = 1.4 μm. The oscillations of the measured magnetic fields have a period of 7 μm, which corresponds with the bit pattern. Furthermore we observed that the signal from two bits is smaller than the signal of a row of four bits or more, which is due to the fact that the sensor integrates the signal.

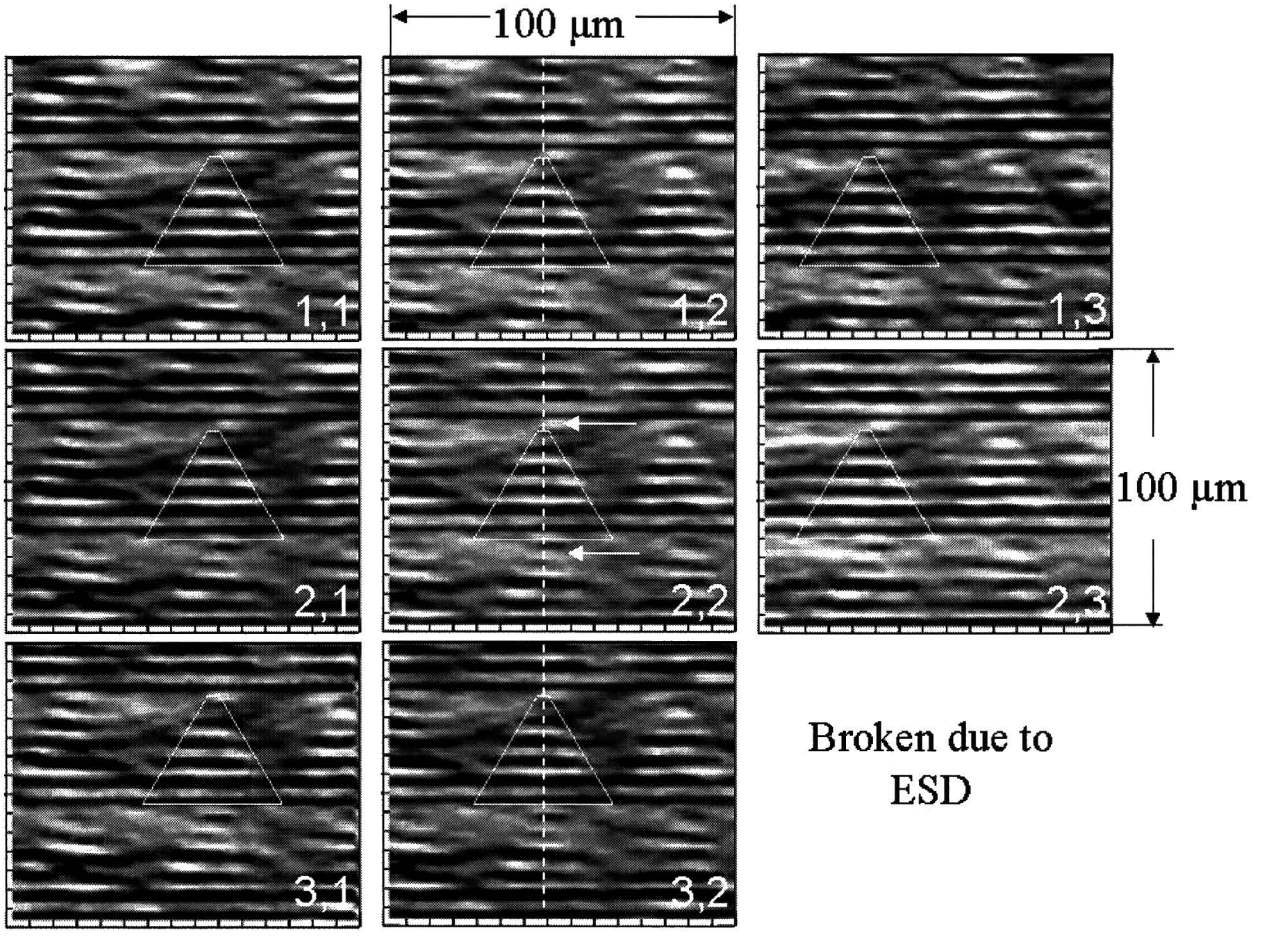

Fig. 4.23: Measured magnetic fields of the eight MTJ elements in the MTJ array. The measurement is done at a height of d_2 = 1.4 µm. The measurements are shown from above and in a grayscale. To give an indication of the amplitude of the measured signal, cross-sections of the measured magnetic fields of the second column are shown in Fig. 4.25. The cross-sections are taken along the dashed lines. In the corner of each measurement the row and column number of the elements are listed. The used settings for the multiplexer and lock-in are; V_{in} = 0.1 V, R_{gain} = 10 kΩ, 10 ms integration time, 12 dB attenuation and a frequency of 900 Hz.

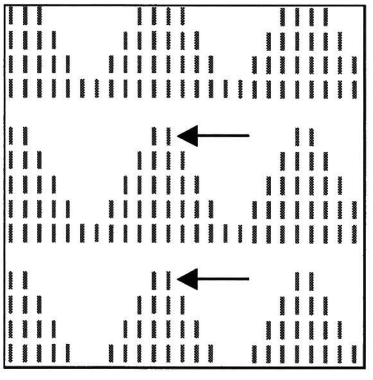

Fig. 4.24: Approximate bit pattern as seen by element 2,2. The arrows designate the end of triangular bit pattern.

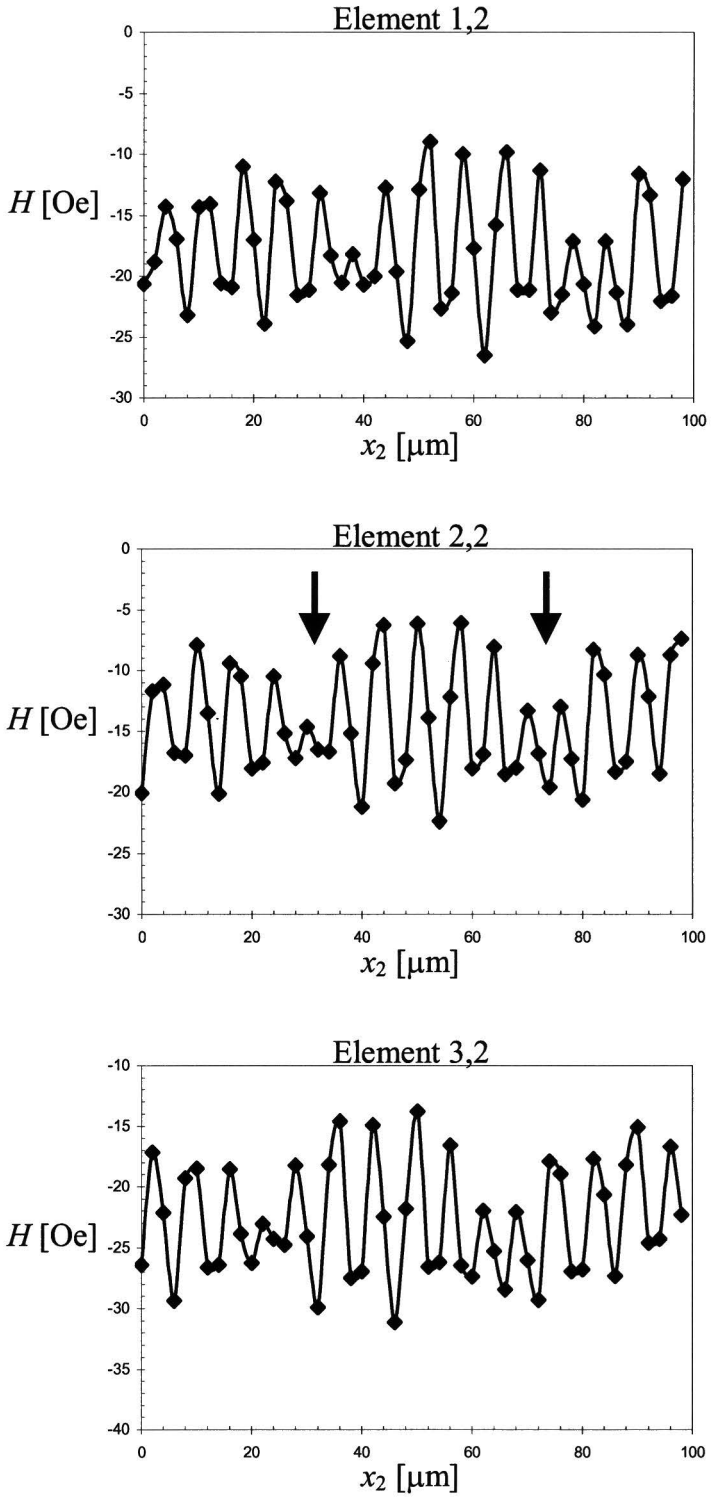

Fig. 4.25: Cross-sections of the measured magnetic fields of the elements in the second column of Fig. 4.23. The measurements are done at a height of d_2 = 1.4 µm. The cross-sections are taken across the dashed lines in Fig. 4.23. The arrows indicate the end of the triangular bit pattern; this is illustrated in Fig. 4.24.

4.4 Feasibility of MROM concept

In the experimental results so far, we have shown that the theory quantitatively predicts the magnitude of the measured signal reasonably well. Therefore we will use the theoretical description of the magnetic bit pattern and sensor sensitivity, as discussed in the theory, to determine the feasibility of the MROM concept, by calculating the design constraint for a real application. With design constraint we mean the required separation distance between the sensor and the medium. This can then be compared with the minimal separation distance obtained in the experimental results. We take portable video as application, because downloading a movie on a portable device via a wireless connection is very expensive. The necessary bit rate for video is ~ 5 Mbit/s, which corresponds with a read out of measurement integration time of $\tau = 200$ ns. We will take 60 Mbyte/cm^2 as the necessary bit density; this allows the storage of a movie on a few squared centimeters. This relates to a pitch of $p_1 = 0.3$ μm in the x_1 direction and a pitch of $p_2 = 0.7$ μm in the x_2 direction. For the size of the bit we will take 0.5 x 0.1 x 0.1 μm (l x w x h), and 0.02 μm for the thickness of ferromagnetic layer. Because $h > t$, $p_3 = h = 0.1$ μm for these parameters, see Fig. 2.9 of the theory for an illustration.

We want to calculate the medium sensor separation distance, at which the signal becomes obscured in the noise. Do this we need to know the smallest detectable magnetic field. If we combine equations (2.43) and (2.44) and substitute $I_{\text{measure}} = V_{\text{measure}} / R_{\text{MTJ}}$ we obtain,

$$R_{\text{noise}} = \frac{\sqrt{4k_b T R_{\text{MTJ}} \Delta f}}{V_{\text{measure}}} R_{\text{MTJ}} \,. \tag{4.3}$$

If we then use equation (2.42) to calculate the change in the resistance of the tunnel junction,

$$\partial R_{\text{MTJ}} = \frac{\Delta R}{M_{\text{free}}(N_1 - N_2)} \partial H \,, \tag{4.4}$$

and if we state that the measured signal has to be at least equal to the noise, we can write,

$$\partial H = \frac{R_{\text{MTJ}}}{\Delta R} \frac{\sqrt{4k_b T R_{\text{MTJ}} \Delta f}}{V_{\text{measure}}} M_{\text{free}}(N_1 - N_2) \,, \tag{4.5}$$

for the smallest detectable magnetic field ∂H. We will calculate ∂H at room temperature for the following parameters: the dimension of the free layer are 0.15 x 0.075 x 0.005 μm (l x w x h), the magnetization of the free layer $4\pi M_{\text{free}} = 10 \cdot 10^3$ G, the spectral bandwidth $\Delta f = 1/2\pi\tau = 1.6 \cdot 10^6$ Hz, the voltage used to measure the resistance $V_{\text{measure}} = 1$ Volt, the resistance of the MTJ $R_{\text{MTJ}} = 10^6$ Ω and the MR ratio $\Delta R / R_{\text{MTJ}} = 0.1$. For these parameters the smallest detectable magnetic field, $\partial H = 0.3$ Oe. If we recalculate the Fourier component, critical for bit detection, for the new parameters, we obtain $G_2[1,1,0] = 2.3 \cdot 10^{-3} M = 23$ Oe, with $4\pi M = 10 \cdot 10^3$ G. If we substitute this into equation (2.46) we can write

$$G_2[1,1,\xi_3] = 23\exp[-2\pi\sqrt{(\frac{1}{3})^2 + (\frac{1}{7})^2}\,\xi_3] = 23\exp[-2.28\xi_3] \text{ Oe.} \quad (4.6)$$

We can now calculate the medium sensor distance by equating $G_2[1,1,\xi_3]$ with ∂H, this gives

$$\xi_3 = -\frac{1}{2.28}\log[\frac{0.3}{23}] = 1.9. \quad (4.7)$$

The corresponding medium sensor distance is $z = \xi_3 p_3 = 190$ nm, using $p_3 = h = 100$ nm, equivalent to the height of the bit. In the experimental results we have determined that the minimal separation distance between a piece of unprocessed silicon (1x2 cm^2) and the medium (6x4 mm^2) is 0.63 μm, when both are cleaned thoroughly. A separation distance of 190 nm is unrealistic in normal ambient conditions, where surface contamination will lead to even larger separation distances. Therefore we conclude that the MROM concept is not a realistic option for video distribution. More general can be concluded that if a high bit density and high bit rate is required, the MROM concept is not adequate. This is because the required separation distance, between the medium and sensor, cannot be obtained in the ambient conditions where real applications operate in.

5 Conclusions and recommendations

5.1 General conclusions

In order to test the MROM concept on its feasibility, a sensor and four different ferromagnetic bit patterns are made. The sensor is created in two different layouts to increase the yield of the process. One layout consists of three vertical and horizontal current lines with a MTJ element at each intersection; this layout is called the MTJ array. In the other layout each MTJ element has a unique current path, this layout is called the single junction. Because the sensor and medium have to be brought into close contact with another, a mechanical setup is build. An optical setup is built for the alignment and separation distance determination of the medium and sensor. Because the magnetoresistance of the sensors has to be calibrated, a calibration setup is also constructed.

- We have found that the minimal obtainable separation distance between the medium (6x4 mm^2), and an unprocessed piece of silicon (1x2 cm^2) is 0.63 μm. This minimal separation distance is limited by surface contamination. We have investigated the influence of the SiO_2 layer, needed for the growth of the MTJ elements, on the detected medium sensor distance. We have found that at small medium sensor distances the peak determination method is more unreliable than at large separation distances. Proper calibration with the medium and MTJ array yields an error of 0.1 μm for small distances (~ 1 μm).

- The calibration of the single junction and MTJ array show that both are magnetoresistive. We can conclude, from the measured H_c^{free}, that the free layer is in one magnetic domain. The dimensions of the free layer are 1x5x0.15 μm ($lxwxh$). From the calibration measurements done with the MTJ array, we can conclude that the state of one element in a row, influences the read out of the all other elements in the row. However, if one of the elements in a row is shorted, the other two elements can still be used as sensor.

- The measured magnetic fields of the various bit patterns show that the CoFe layer is not in a single magnetic domain. This can be concluded from the fact that the measured signal shows fluctuation at positions where no bits are present. Bit patterns can be recognized in the measured signal. The position at which a bit is missing cannot be recognized due to large irregular fluctuations. Single bits and groups of five bits are difficult to detect and can hardly be recognized. The reason that groups of bits are easier to detect is because the sensor integrates the signal over a few bits.

- The comparison between theory and experiment showed, that the theory quantitatively predicts the magnitude of the measured signal reasonably well. The shape of the measured signal also shows a similar behavior as the theoretical signal. However, the measured signal is more irregular and it appears that the magnetic poles of the bits are closer together. This indicates that the bit is mainly in one magnetic domain, but that magnetic subdomains do form at the edges of a bit. This is confirmed by a calculation of the magnetic structure with the OOMMF package. The exponential decay of the calculated Fourier component, as a function of the sensor medium separation distance, shows a good match with the amplitude

of the measured signal, at least at large separation distances. At smaller distances, ~ 1 μm, the measured amplitude is approximately a factor two larger than the calculated Fourier component. This is because at smaller distances the components with higher wave numbers are also present in the measured signal, and the exact magnetic bit structure is more important.

- The measurement with a 3x3 MTJ array shows that each element of the MTJ array can be read out individually, without influence from other elements.

- From the calculation of the required medium sensor distance, it followed that the MROM concept is not applicable for video content distribution. The calculation showed that the separation distance should be 0.19 μm, if the bit rate is ~ 5 Mbit/s and the bit density is 60 Mbyte/cm^2. The minimal measured distance in the experiment is 0.63 μm; this is measured with an unprocessed piece of silicon and the medium. Therefore we can conclude that a separation distance of 0.19 μm is unrealistically low. In general we can conclude, that the MROM concept is not suitable for any application requiring bit densities and bit rates associated with video applications.

5.2 Recommendations

We will focus the recommendations on the medium and sensor and not on the experimental setup. We did not observe oscillations in the measured magnetic fields in the x_1 direction, which could be attributed to the pitch of the bit pattern in that direction. This is because the sensor averages the oscillations in that direction; see Fig. 4.11. An obvious recommendation therefore is to make the sensor smaller than the bits. For example, if we use MTJ element of 1 μm wide and 0.2 μm long, we would observe oscillations in the magnetic field in the x_1 direction. In this research we used an analog sensor configuration, because we wanted to measure the exact shape of the magnetic fields of the bit patterns. However, in an real application we want maximum output signal, which means that the sensor has to switch from its anti-parallel state to its parallel state, or vice versa. This can be achieved if the fixed layer is biased in the longitudinal direction of the sensor. Such a sensor configuration with the corresponding MR curve is displayed in Fig. 5.1.

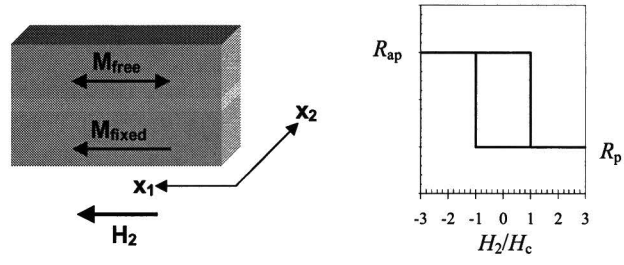

Fig. 5.1: Sensor configuration and corresponding MR curve that are more suitable for a real application. The resistance of the sensor will be swept from R_p to R_{ap}, or vice versa, in this case.

The deposited CoFe layer on the substrate has an unwanted side effect, it creates a lot of fluctuations in the measured magnetic field that do not correspond to any bit pattern. This is because it is not in one magnetic domain. This effect can be reduced by increasing the height of the

bits, see Fig. 2.9, and by enhancing the anisotropy of the ferromagnetic layer. The anisotropy can be enhanced by depositing another ferromagnetic material, with a higher anisotropy, or by changing the shape of the entire CoFe layer.

6 Literature

[1] Optics, second edition, Eugene Hecht, Addison-Wesley, 1998, Page 416-421, ISBN 0-201-11611-1
[2] Classical Electrodynamics, third edition, John David Jackson, John Wiley & Sons INC.
[3] Lecture notes of coarse Mathematische Fysica en Theoretische Mechanica, W.M. De Muynck, Technical University of Eindhoven.
[4] E.L. Wolf, Principles of Tunneling Spectroscopy (Clarendon Press, Oxford, 1985)
[5] E. Burstein and S. Lundqvist (eds.), Tunneling Phenomena in Solids (Plenum Press, New York, 1969)
[6] I. Giaever, Phys. Rev. Lett. 5 (1960) 147, 464; I. Giaever and K. Megerle, Phys. Rev. 122 (1961) 110; I. Giaever, H. Hart and K. Megerle, Phys. Rev. 126 (1962) 941; D.H. Douglass Jr. and L.M. Falicov, in: Progress in Low Temperature Physics 4, ed. C.J. Gorter (North-Holland, Amsterdam, 1964) p. 97.
[7] Introduction to Quantum Mechanics, David J. Griffiths, Prentice Hall International Edition, 1994, ISBN 0-13-185513-1
[8] Solid State Physics International Edition, Ashcroft and Mermin, W. B. Saunders Company, 1976, ISBN 0-03-049346-3
[9] Introduction to Modern Magnetism, Swagten, H.J.M. "Magnetisme" course syllabus 2003-2004 – Eindhoven, August 26, 2003
[10] The DFT An Owner's manual for the Discrete Fourier Transform, William L. Briggs and Van Emden Henson, SIAM, 1995, ISBN 0-89871-342-0
[11] Ferromagnetism, Richard M. Bozorth, IEEE Press, 1993, ISBN 0-7803-1032-2

7 Appendix

7.1 Focus problem white light interferometer

The difficulty with focusing and collimating white light comes from the fact that the refractive index ($n[\lambda]$) is a function of the wavelength (λ). It follows then via the thin-lens equation,

$$\frac{1}{f[\lambda]} = (n[\lambda]-1)\left(\frac{1}{R_1} - \frac{1}{R_2}\right) \tag{7.1}$$

that the focal length ($f[\lambda]$) is also a function of λ. R_1 and R_2 are the degrees of curvature of respectively the front and backside of the lens. To see the consequence of this lets imagine a bundle of collimated white light incident on lens 2 in Fig. 3.13[25] when the medium is removed from the MROM setup. This situation is drawn in Fig. 7.1. The virtual focus points f` of each wavelength, created by the silicon and the lens, determines the eventual spot size of that wavelength on the fiber of the spectrometer. By adjusting the position of the silicon a different wavelength is brought into focus and thus chances the spot size of each wavelength. Since the spot size is larger than the fiber of the spectrometer the measured spectrum changes as the position of the silicon changes.

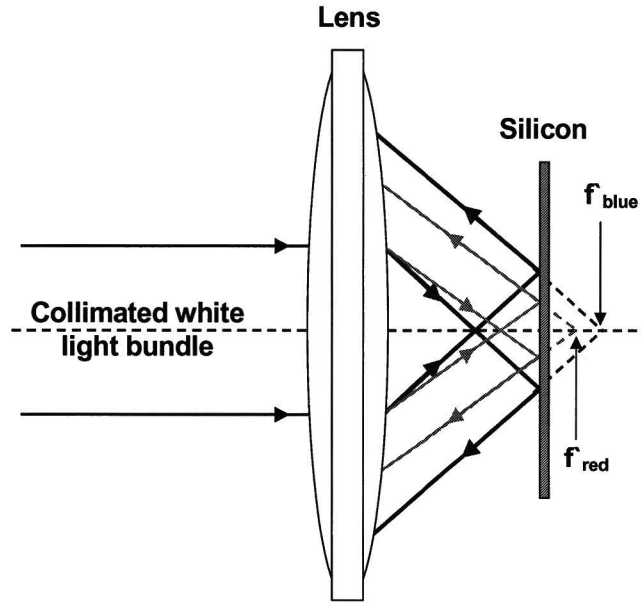

Fig. 7.1: The focus problem illustrated schematically for two different wavelengths. The silicon acts as a mirror and creates virtual focus f` points for each wavelength. As the position of the silicon is changed, the position of the virtual focus points is also changed.

[25] This assumes that we already created a collimated bundle of white light, which is precisely one of the problems. However the origin of the focus problem is at lens 2, lens 1 and 3 (Fig. 3.13) just make it worse. So to explain the origin of the focus problem we only need to take a look at lens 2 in combination with the MROM setup. Therefore it is a safe assumption and it makes the discussion a lot easier.

7.2 Components Tensor

For the case of a rectangular ferromagnet the components of the tensor, see equation (2.15), are integrals that can be evaluated analytical. The expression for each component is:

$$N_{11}[\mathbf{x}] = \sum_{i=0}^{1}\sum_{j=0}^{1}\sum_{k=0}^{1}(-1)^{i+j+k}\frac{1}{4\pi}\arctan\left[\frac{(x_2-y_2)(x_3-y_3)}{(x_1-y_1)\sqrt{(x_1-y_1)^2+(x_2-y_2)^2+(x_3-y_3)^2}}\right],$$

$$N_{12}[\mathbf{x}] = \sum_{i=0}^{1}\sum_{j=0}^{1}\sum_{k=0}^{1}(-1)^{i+j+k+1}\frac{1}{4\pi}\log\left[x_3-y_3+\sqrt{(x_1-y_1)^2+(x_2-y_2)^2+(x_3-y_3)^2}\right],$$

$$N_{13}[\mathbf{x}] = \sum_{i=0}^{1}\sum_{j=0}^{1}\sum_{k=0}^{1}(-1)^{i+j+k+1}\frac{1}{4\pi}\log\left[x_2-y_2+\sqrt{(x_1-y_1)^2+(x_2-y_2)^2+(x_3-y_3)^2}\right],$$

$$N_{21}[\mathbf{x}] = \sum_{i=0}^{1}\sum_{j=0}^{1}\sum_{k=0}^{1}(-1)^{i+j+k+1}\frac{1}{4\pi}\log\left[x_3-y_3+\sqrt{(x_1-y_1)^2+(x_2-y_2)^2+(x_3-y_3)^2}\right],$$

$$N_{22}[\mathbf{x}] = \sum_{i=0}^{1}\sum_{j=0}^{1}\sum_{k=0}^{1}(-1)^{i+j+k}\frac{1}{4\pi}\arctan\left[\frac{(x_1-y_1)(x_3-y_3)}{(x_2-y_2)\sqrt{(x_1-y_1)^2+(x_2-y_2)^2+(x_3-y_3)^2}}\right],$$

$$N_{23}[\mathbf{x}] = \sum_{i=0}^{1}\sum_{j=0}^{1}\sum_{k=0}^{1}(-1)^{i+j+k+1}\frac{1}{4\pi}\log\left[x_1-y_1+\sqrt{(x_1-y_1)^2+(x_2-y_2)^2+(x_3-y_3)^2}\right],$$

$$N_{31}[\mathbf{x}] = \sum_{i=0}^{1}\sum_{j=0}^{1}\sum_{k=0}^{1}(-1)^{i+j+k+1}\frac{1}{4\pi}\mathrm{Log}\left[x_2-y_2+\sqrt{(x_1-y_1)^2+(x_2-y_2)^2+(x_3-y_3)^2}\right],$$

$$N_{32}[\mathbf{x}] = \sum_{i=0}^{1}\sum_{j=0}^{1}\sum_{k=0}^{1}(-1)^{i+j+k+1}\frac{1}{4\pi}\log\left[x_1-y_1+\sqrt{(x_1-y_1)^2+(x_2-y_2)^2+(x_3-y_3)^2}\right],$$

$$N_{33}[\mathbf{x}] = \sum_{i=0}^{1}\sum_{j=0}^{1}\sum_{k=0}^{1}(-1)^{i+j+k}\frac{1}{4\pi}\arctan\left[\frac{(x_2-y_2)(x_3-y_3)}{(x_3-y_3)\sqrt{(x_1-y_1)^2+(x_2-y_2)^2+(x_3-y_3)^2}}\right],$$

in which y_1, y_2, y_3 should be substituted with:

$y_1 = w(i-\frac{1}{2})$, $y_2 = l(j-\frac{1}{2})$, $y_3 = h(k-\frac{1}{2})$.

7.3 Calculation Fourier component H_2

We want to calculate the Fourier component of H_2 at the spatial frequency of $k_i = 1/p_i$. We will assume an infinite bit array of ones. Because we anticipate that we cannot calculate this

analytically, we will write H_2 as function of scaled coordinates $\xi = (x_1/p1, x_2/p_2, z/p_3)$ and calculate the Fourier component at the scaled spatial frequency $\kappa_i = p_i k_i = 1$. This will be done with discrete Fourier transformation (DFT). We begin with writing the total magnetic field of an infinite bit array of ones, H_2, as a superposition of a single bit with the help of a convolution,

$$H_2[\xi_1,\xi_2,\xi_3] = H_2^{\text{bit}}[\xi_1,\xi_2,\xi_3] \otimes \left(\sum_{n=-\infty}^{n=\infty} \delta[\xi_1 - n] \sum_{m=-\infty}^{m=\infty} \delta[\xi_2 - m]\right), \tag{7.2}$$

in which $H_2^{\text{bit}}[\xi_1,\xi_2,\xi_3]$ is the magnetic field of an individual bit and δ is the Dirac delta function. The magnetic field of an individual bit is given by

$$H_2^{\text{bit}}[\xi_1,\xi_2,\xi_3] = \sum_{m=0}^{1}\sum_{i=0}^{1}\sum_{j=0}^{1}\sum_{k=0}^{1}(-1)^{i+j+k+m}\frac{M}{4\pi}\arctan\left[\frac{p_1(\xi_1-\rho_1)(\xi_3-\rho_3)}{p_2(\xi_2-\rho_2)\sqrt{(\frac{p_1}{p_3})^2(\xi_1-\rho_1)^2+(\frac{p_2}{p_3})^2(\xi_2-\rho_2)^2+(\xi_3-\rho_3)^2}}\right],$$

in which ρ_1, ρ_2, ρ_3 should be substituted with:

$$\rho_1 = \alpha_1(i-\tfrac{1}{2}),\ \rho_2 = \alpha_2(j-\tfrac{1}{2}),\ \rho_3 = \alpha_3(k-1)+\beta(m-1),$$

where $\alpha_i = b_i / p_i$ and $\beta = h / p_3$. If we calculate the two-dimensional Fourier transform, $G_2[\kappa_1, \kappa_2, \xi_3]$, of (7.2) we obtain,

$$G_2[\kappa_1,\kappa_2,\xi_3] = \sum_{n=-\infty}^{n=\infty}\sum_{m=-\infty}^{m=\infty} G_2^{\text{bit}}[n,m,\xi_3]\delta(\kappa_1 - n, \kappa_2 - m), \tag{7.3}$$

in which $G_2^{\text{bit}}[n,m,\xi_3]$ is the two-dimensional Fourier transform of $H_2^{\text{bit}}[\xi_1,\xi_2,\xi_3]$. If we calculate the Fourier component at $\kappa_1 = \kappa_2 = 1$ we retrieve,

$$G_2[1,1,\xi_3] = G_2^{\text{bit}}[1,1,\xi_3], \tag{7.4}$$

because the Dirac delta functions is only non-zero for $n = m = 1$. This brings us to the conclusion that we only have to calculate the Fourier transform of the magnetic field of one bit, instead of an entire array. This calculation, however, still has to be done with DFT. Because we will use the outcome in an actual calculation, we must have an idea of the error in the DFT with respect to the Fourier integral. To accomplish this, the DFT is calculated on a different set of intervals and for a different number of samples, to see if it converges. Before presenting the results we mention that the DFT is taken for $\xi_3 = 0$ and all the other relevant parameters are, $\alpha_1 = 1/4$, $\alpha_2 = 5/7$, $\alpha_3 = 2/10$, $\beta = 1$ and $M = 1$. The result of the DFT for different set of intervals and sampling is shown in Fig. 7.2.

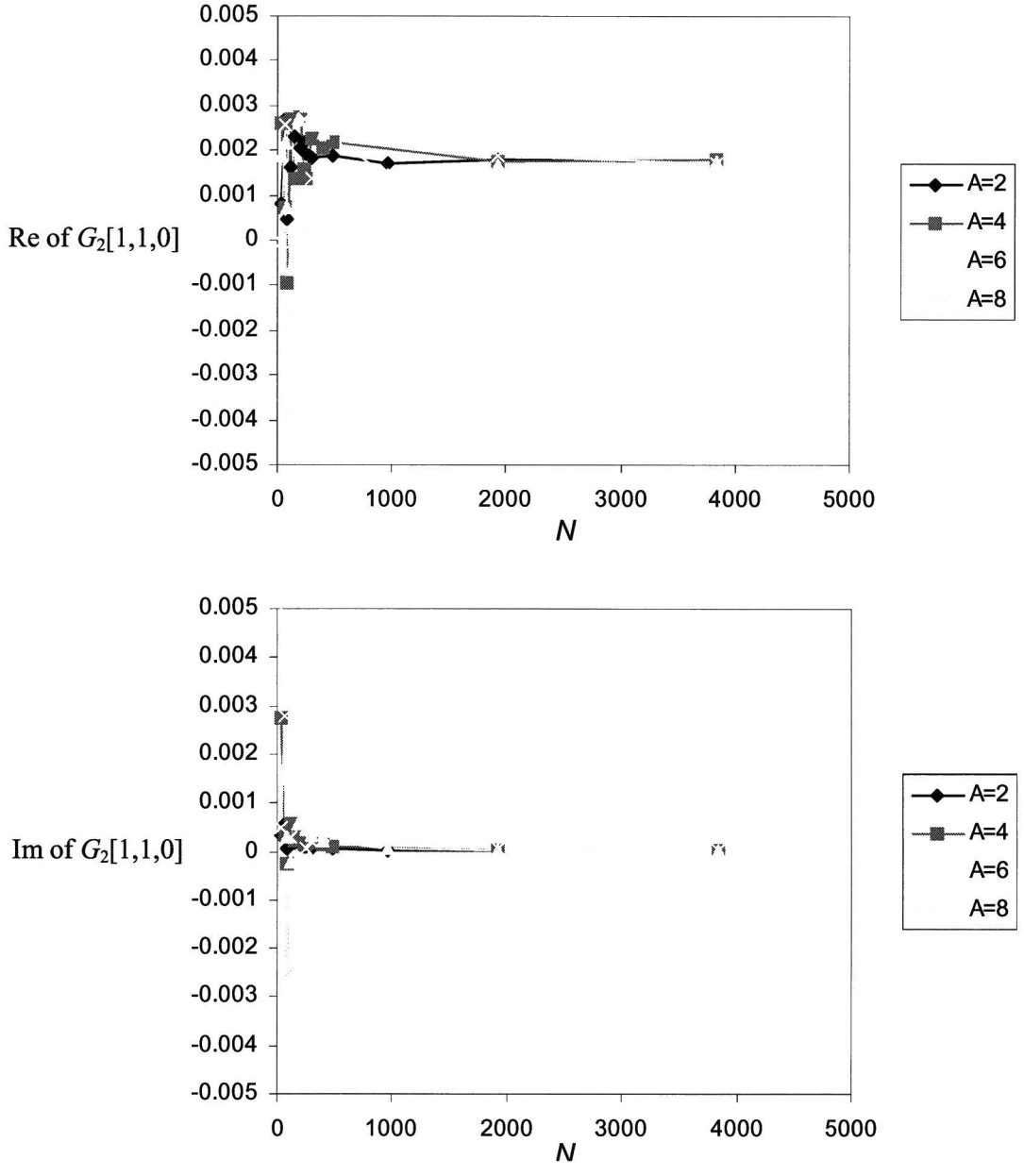

Fig. 7.2: Result of the DFT for different intervals (A) and sampling numbers (N). The upper figure shows the real part and the lower figure shows the imaginary part. We can see that both quantities converge if we increase N, for different values of A.

The interval on which $H_2^{bit}[\xi_1,\xi_2,\xi_3]$ is sampled is denoted with $A = A_1 = A_2$, and $N = N_1 = N_2$ is the number of samples used. As we can see the value of $G_2^{bit}[1,1,0]$ converges as N goes up. This implies that we have obtained the correct value. However, we should be careful with this conclusion because in the formal limit[26],

[26] For a derivation of the limit and more information about the DFT in general and the error with respect to the Fourier integral in special, see reference [10].

$$\lim_{\Delta\xi_{1,2}\to 0} \lim_{\substack{A_{1,2}\to\infty \\ N_{1,2}\to\infty}} A_1 A_2 G_{nm}^{bit} = G_2^{bit}[f_1^n, f_2^m], \tag{7.5}$$

A also needs to go to infinity, and $\Delta\xi_i = A_i / N_i$, i =1,2 has to go to zero. For completeness we will state the used definition of the DFT,

$$G_{nm}^{bit} = \frac{1}{N_1 N_2} \sum_{k=-\frac{N_1}{2}+1}^{k=\frac{N_1}{2}} \sum_{l=-\frac{N_2}{2}+1}^{l=\frac{N_2}{2}} H_2[k\Delta\xi_1, l\Delta\xi_2, 0] e^{-2\pi i\left(\frac{nk}{N_1}+\frac{ml}{N_2}\right)}. \tag{7.6}$$

Therefore we also need to investigate the influence of A, independent of N and check if the value converges. We have listed the values of the DFT, for $N = 1920$ and $N = 3840$ in Table 7.1.

	N	
A	1920	3840
2	$1.80 \cdot 10^{-3}$	$1.76 \cdot 10^{-3}$
4	$1.73 \cdot 10^{-3}$	$1.80 \cdot 10^{-3}$
6	$1.66 \cdot 10^{-3}$	$1.77 \cdot 10^{-3}$
8	$1.88 \cdot 10^{-3}$	$1.73 \cdot 10^{-3}$

Table 7.1: Values of the DFT for different of N and A.

As we can see the real part of $G_2^{bit}[1,1,0]$ at $N = 1920$ and $N = 3840$ is almost constant for the various values of A. This means increasing A or increasing N or halving $\Delta\xi_i$, doesn't affect the value. This brings us to the conclusion that we have obtained a correct value for the Fourier component, of $G_2^{bit}[1,1,0] = 1.8 \cdot 10^{-3}$.

8 Erratum

In paragraph 4.3.3 the measured magnetic bit fields are compared with analytical calculations. However, these analytical calculations are done at an incorrect height, because the free magnetic layer of the MTJ is not at the air-SiO_2 interface of the sensor, but buried within the SiO_2. This is illustrated in Fig. 8.1.

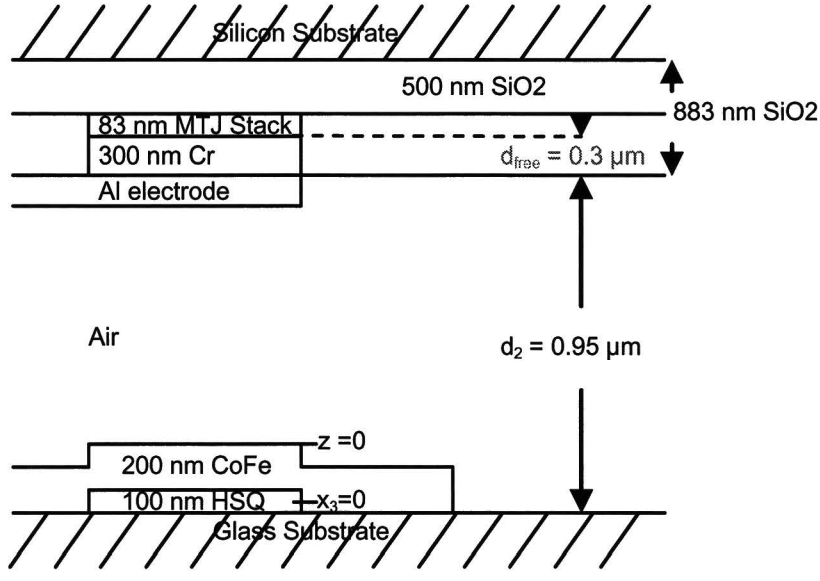

Fig. 8.1: Illustration of a MTJ sensor element in combination with a bit. The free layer of the MTJ is not at the air-SiO_2 interface of the sensor, but instead is located 300 inwards.

This means that the calculation shown in Fig. 4.19 must be recalculated 300 nm higher. In Fig. 8.2 the correct calculated signal, together with the measured signal for d_2 = 0.95 µm is shown. The bold line is the calculated signal; the thin line is the measured signal. The correct calculated signal is in the same order of magnitude as the measured signal, the shape of the calculated and measured signal also correspond. The conclusions drawn from Fig. 4.19 are therefore still valid.

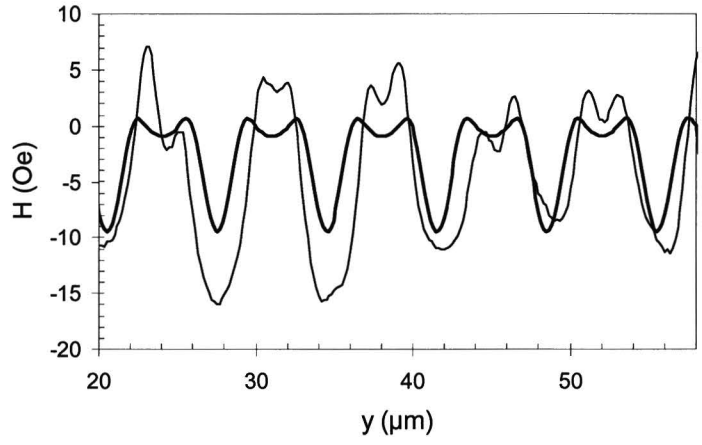

Fig. 8.2: Correct calculated signal (bold line) and measured signal (thin line) at a medium sensor distance of $d_2 = 0.95$ µm.

Fig. 4.19 is not the only figure which needs attention. The z axis of Fig. 4.22 should be translated with 300 nm in order to make the comparison with theory correct. This is done in Fig. 8.3, the dots represent the measured amplitudes of the magnetic bit field, and the solid line is the calculated prediction. The measured amplitudes are still a factor two higher than the calculated amplitudes, the conclusions drawn from Fig. 4.22 are therefore still correct.

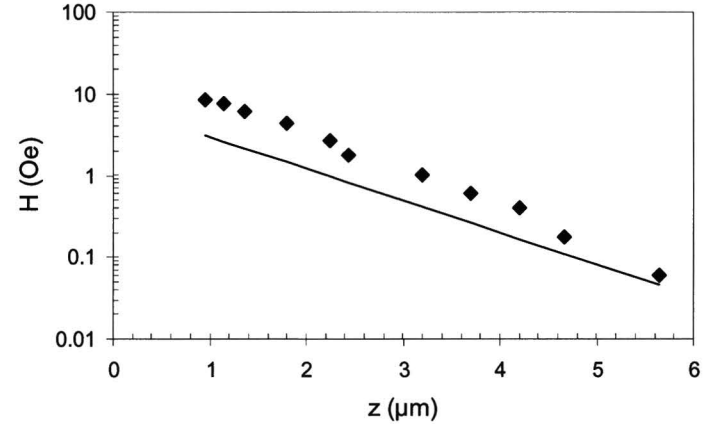

Fig. 8.3: Logarithmic plot of the measured and calculated amplitude of the Fourier component of the magnetic field, critical for bit detection, versus the correct separation distance.

To sum up this chapter, it was found that the theory and experiment where compared at an incorrect height. The fact that the free layer of the MTJ is located at 300 nm from the air-SiO_2 interface of the sensor was not taken into account. The theoretical curves where recalculated at the correct height, and it was found that the conclusions do not change.